The Effect of Topography on the Martian Atmospheric Circulation and Determining Pluto's Atmospheric Thermal Structure from Stellar Occultations

by

Angela Marie Zalucha

Submitted to the Department of Earth, Atmospheric, and Planetary Sciences
in partial fulfillment of the requirements for the degree of

Doctor of Philosophy in Atmospheric Science

at the

MASSACHUSETTS INSTITUTE OF TECHNOLOGY

June 2010

Author .....
Department of Earth, Atmospheric, and Planetary Sciences
April 22, 2010

Certified by .....
R. Alan Plumb
Professor of Meteorology
Department of Earth, Atmospheric, and Planetary Sciences
Thesis Supervisor

Accepted by .....
Maria T. Zuber
E. A. Griswold Professor of Geophysics
Head, Department of Earth, Atmospheric, and Planetary Sciences

The Effect of Topography on the Martian Atmospheric Circulation and Determining Pluto's Atmospheric Thermal Structure from Stellar Occultations

by

Angela Marie Zalucha

Submitted to the Department of Earth, Atmospheric, and Planetary Sciences
on April 22, 2010, in partial fulfillment of the
requirements for the degree of
Doctor of Philosophy in Atmospheric Science

Abstract

Previous work with Mars General Circulation Models (MGCMs) has shown that the north-south slope in Martian topography causes asymmetries in the Hadley cells at equinox and in the annual average. To quantitatively solve for the latitude of the dividing streamline and poleward boundaries of the cells, the Hadley cell model of Lindzen and Hou [1988, J. Atmos Sci. 45, 216–2427] was modified to include topography. The model was thermally forced by Newtonian relaxation to an equilibrium temperature profile calculated with daily averaged solar forcing at constant season. Two sets of equilibrium temperatures were considered that either contained the effects of convection or did not. When convective effects were allowed, the presence of the slope component shifted the dividing streamline upslope, qualitatively similar to a change of season in the original Lindzen and Hou [1988] (flat) model. The modified model also confirmed that the geometrical effects of the slope are much smaller than the thermal effects of the slope on the radiative-convective equilibrium temperature aloft. The results are compared to a simple MGCM forced by Newtonian relaxation to the same equilibrium temperature profiles, and the two models agree except at the winter pole near solstice. The simple MGCM results for radiative-convective forcing also show an asymmetry between the strengths of the Hadley cells at northern summer and northern winter solstices. The Hadley cell weakens with increasing slope steepness at northern summer solstice, but has little effect on the strength at northern winter solstice.

In the second part, a radiative-conductive model from Strobel et al. [1996, Icarus 120, 266–289] was used to least-squares fit Pluto stellar occultation light curve data. This model predicted atmospheric temperature based on surface temperature, surface pressure, surface radius, and methane and carbon monoxide mixing ratios, from which model light curves were able to be calculated. The model improves upon previous techniques for deriving Pluto's atmospheric thermal structure from stellar occultation light curves by calculating temperature (as a function of height) caused by heating and cooling by species in Pluto's atmosphere, instead of a general assumption that temperature follows a power law with height or some other idealized function. Fits were able to be performed for model surface radius, surface pressure, and methane

mixing ratio with one of the 2006 datasets and for surface pressure and methane mixing ratio for other datasets from the years 1988, 2002, 2006, and 2008. It was not possible to fit for carbon monoxide mixing ratio and surface temperature because the light curves are not sensitive to these parameters. The model surface radius, under the assumption of a stratosphere only (i.e. no troposphere) model and radiative equilibrium, was determined to be 1180 +20/-10 km, where the error bars are those from the formal least-squares fit and errors on the closest approach distance. The methane mixing ratio results are more scattered with time and are in the range of 0.18% to 1.78%. The surface pressure results show an increasing trend with time, although it is not as dramatic as the factor of 2 from previous studies. Finally, I demonstrate with a preliminary Pluto general circulation model the importance of the effect of atmospheric circulation on temperature and surface pressure.

Thesis Supervisor: R. Alan Plumb
Title: Professor of Meteorology
Department of Earth, Atmospheric, and Planetary Sciences

Acknowledgments

I would like to thank my advisor Alan Plumb for his guidance throughout my graduate tenure. John Wilson has furnished GFDL MGCM results and provided valuable insight into MGCM practices and the Martian atmosphere. The other committee members, Jim Elliot, Kerry Emanuel, Glenn Flierl, and Maria Zuber, have also contributed to the completion of my thesis and graduate education. I thank Amanda Gulbis for her advising on the Pluto parts of my thesis, and Mike Person for his assistance with Pluto light curve data and previous analyses. I would like to thank Andrea Molod and Jean-Michel Campin for helping me use the MIT GCM. I would also like to thank Darrell Strobel and Xun Zhu for the use of their Pluto radiative-conductive model. Various components of this thesis were reviewed by Jonathan Mitchell, Jude Sabato, and an anonymous reviewer prior to publication in the Journal of the Atmospheric Sciences. Jenny Meyer lent a careful eye in proofreading the final version of my thesis. This work was supported in part by NSF grant ATM-0436288 and NASA grants NNX08AE92G, NNX07AK73G, and NNG05GO91G.

Contents

List of Figures

List of Tables

Chapter 1

Introduction

The study of planetary atmospheres is not only important for the purpose of space exploration, but for understanding the physics of atmospheres in general. If we are to better understand the laws that govern our own planet's atmosphere, we should make use of the vastly different cases of atmospheres that are available in our solar system and beyond. Spacecraft and ground-based telescopes have provided astounding facts about planetary atmospheres [see Hunt, 1983; Prinn and Fegley, 1987, for a review]. To interpret and augment planetary atmospheres data, models are essential. Models must be used to convert data from its raw form to parameters relevant to atmospheric theories. General circulation models, which push the limits of computational power, contain a large number of physical processes thought to be important to a given atmospheric system and are necessary for examining the atmosphere as a whole. On the other hand, simple models are vital for isolating a particular effect and should not be dismissed on the basis of their simplicity alone. In my thesis, I make use of several different types of models to investigate problems in the atmospheres of Mars and Pluto.

1.1 Properties of the Martian Atmosphere

The atmosphere of Mars is an interesting object of study because of its similarities, yet striking differences, to that of Earth. Both planets are small, rocky bodies with relatively thin atmospheres (contrasting with Jupiter and Saturn). Both have nearly the same rotation rate and orbital inclinations (contrasting with Venus). Both have comparable distances from the Sun and length of year (contrasting with Titan).

As shown in Table 1.1 [taken from Owen, 1992], CO_2 is the dominant gas in the Martian atmosphere. At present, there is notably very little water in the Martian atmosphere. While some small, thin water ice clouds have been observed, they are not of primary importance to radiative processes. An important atmospheric aerosol not shown in Table 1.1 is dust. Atmospheric dust disturbances occur on a wide range of scales—from localized dust devils, to regional storms, to planet-wide storms. The dust is important radiatively, as it is an efficient absorber at infrared wavelengths, but difficult to measure and therefore accurately model because of its high variability

in space and time.

Table 1.2 [taken from Zurek et al., 1992] shows some basic planetary constants for Mars. The significantly larger orbital eccentricity of 0.093 compared to Earth's value of 0.017 is particularly important to the Martian climate. Figure 1-1 shows a diagram of the Martian orbit. By convention, Martian seasons are measured according to the ecliptic longitude of the Sun in Mars-centered coordinates and denoted by the parameter L_s. For example, L_s= 0° corresponds to the northern hemisphere spring equinox, L_s= 90° to the northern hemisphere summer solstice, L_s= 180° to the autumn equinox, and L_s= 270° to the winter solstice. According to Kepler's second law, a planet orbiting the Sun moves faster at perihelion than at aphelion. The time of perihelion, $L_{sp} = 252°$, corresponds closely to the time of northern hemisphere winter; thus the northern hemisphere winter is shorter than that of the southern hemisphere. Likewise, northern hemisphere summer is longer than that of the southern hemisphere. As shown in Fig. 1-1, the time between the northern hemisphere spring and autumn equinoxes is 371 sols compared with 297 sols between autumn and spring, where the term sol refers to a Martian solar day.

Mars' relatively eccentric orbit also has implications for the solar constant S, which is given by

$$S = \frac{L_\odot}{4\pi d^2}, \tag{1.1}$$

where $L_\odot = 3.826 \times 10^{26}$ W is the luminosity of the Sun and d is the Sun-Mars distance. When Mars is at its average distance from the Sun of 1.5 AU, $S = 600$ W m^2 (denoted by S_o). Using the aphelion and perihelion values from Table 1.2, S ranges from 488–714 W m^{-2} or 81–119% of the value at the average Sun-Mars distance. The corresponding range for Earth is 96–104%. Northern hemisphere summer occurs near aphelion; thus, solar heating during northern summer is less than during southern summer.

Mars also has a north-south asymmetry in its topography (relative to the aeroid), with the southern hemisphere being on average about 5 km higher in elevation than the northern hemisphere [Smith et al., 1999, Fig. 1-2]. The cause of this asymmetry has been suggested to be the result of a giant impact [e.g. Andrews-Hanna et al., 2008] or mantle convection varying on a planet-wide scale [e.g. Zhong and Zuber, 2001]. Mars has several large volcanoes, some over an atmospheric scale height (11 km) higher than the surrounding terrain. The elevation difference between the highest mountains and the lowest basins is 30 km—well over a scale height—making topographical forcing important to atmospheric circulations. Surface albedo variations are also important, with a distinct bimodal distribution between lighter and darker regions [Pleskot and Miner, 1981]. Surface thermal inertia varies by 1–2 orders of magnitude [Putzig et al., 2005]. In addition, the polar ice caps (discussed below) are highly reflective.

One major difference between Earth and Mars is that the major atmospheric constituent of the latter (i.e. CO_2) is in vapor pressure equilibrium with the surface. Data from Viking Lander 1 (Fig. 1-3) show a seasonal trend in the surface pressure signal. During autumn and winter, when polar temperatures fall below the freezing

point of CO_2, part of the atmosphere condenses into a seasonal CO_2 ice cap. In the following spring and summer, the cap sublimates back into the atmosphere. The surface pressure signal has two minima per year, corresponding to the northern and southern winter seasons. A deeper minimum occurs during southern winter, since this season is longer than northern winter, and hence there is more time for CO_2 to freeze out.

1.2 Martian General Circulation Models

The Martian atmosphere is generally divided into 3 layers: the lower atmosphere in the region from the surface to 50 km altitude, which has a mean lapse rate of 2–3 K km^{-1}; the middle atmosphere in the region from 50 to ~90 km, which is nearly isothermal; and a thermosphere above ~90 km [Barth et al., 1992]. Observational Martian atmospheric data are relatively sparse. The available *in situ* data include entry and surface data from the two Viking landers [e.g. Seiff and Kirk, 1977] and Mars Pathfinder [Magalhães et al., 1999], as well as entry data from the Spirit and Opportunity rovers [Withers and Smith, 2006]. Stellar occultation data [e.g. Elliot et al., 1977]; radio occultation data from the Mars Global Surveyor (MGS) [e.g. Hinson et al., 2001]; and thermal infrared measurements from the Mariner 9 Infrared Interferometer Spectrometer (IRIS) [e.g. Magalhães, 1987], the Viking Infrared Thermal Mapper (IRTM) [e.g. Martin and Kieffer, 1979], and the MGS Thermal Emission Spectrometer (TES) [e.g. Smith, 2004] have been important for determining vertical structure. The main results of these studies (and others not listed here) were lower and middle atmosphere temperature data and surface temperature, wind, and pressure data. These observations were greatly limited in space and time, and Mars General Circulation Models (MGCMs) are necessary for deducing planet-wide atmospheric processes over a variety of seasons. Below is a summary of the MGCMs present in the literature (some have undergone further modification since their most recent publication).

Leovy and Mintz [1969] created the first MGCM and used it to simulate the northern vernal equinox and northern winter solstice conditions. Even though the model had only four levels, it illuminated several key processes in the Martian atmosphere and the task of modeling it. One is the rapid spin-up time compared with terrestrial General Circulation Models (GCMs)—less than 10 sols in their experiments. They also found a temperature distribution and a circulation pattern that were symmetric about the equator during the equinox. The temperature gradient was flat at the equator and steeper in the midlatitudes, much like the terrestrial atmosphere. In the solstice experiment, a strong, thermally-direct, meridional circulation spanned the equator. In addition, the temperature gradient was flat at the equator and in the summer hemisphere while steeper in the winter hemisphere. Also during the solstice experiment they noted a poleward mass transfer toward the condensing CO_2 polar ice cap.

Pollack et al. [1990] described the NASA Ames MGCM. These authors conducted several experiments with a different amount of dust (i.e. surface optical depth) in each

one. The amount of dust in a particular experiment was constant in time and varied only in the vertical coordinate. In general, greater amounts of dust implied greater heating and therefore stronger overturning cells. A net "condensation flow" [as seen by Leovy and Mintz, 1969] resulted in their simulations due to mass flow towards or away from the poles as the CO_2 ice caps were condensing or subliming, respectively. This component of the meridional circulation does not have a counterpart on Earth. Their results also showed that CO_2 may condense in the winter polar atmosphere in addition to the surface (where the majority of condensation takes place), which has implications for the radiative properties of this part of the atmosphere. The proportion of CO_2 that condensed in the atmosphere was dependent on the atmospheric dust optical depth. Higher dust loadings allowed the atmosphere to more efficiently cool to the frost point and thus increased the atmospheric condensation rate relative to the surface condensation rate.

Wilson and Hamilton [1996] used a modified version of the Geophysical Fluid Dynamics Laboratory (GFDL) SKYHI terrestrial GCM to investigate thermal tides in the Martian atmosphere. These authors find a "very pronounced" zonal wavenumber-2 modulation, which is caused by the prominent zonal wavenumber-2 patterns in topography and surface thermal inertia. In addition, the eastward-propagating zonal wavenumber-1 Kelvin mode has a period near 1 sol and is thus near resonance. MGS TES observations [Hinson et al., 2001] show large amplitudes in the zonal wavenumber-2 component of geopotential height between 2 and .25 mb (10–30 km), which are attributed to thermal tides. Hence, thermal tides are of greater relative importance in the Martian atmosphere than the terrestrial one.

Hourdin et al. [1993] constructed a model based on the dynamical core from the terrestrial climate model of the Laboratoire de Météorologie Dynamique (LMD) and later Oxford University [Forget et al., 1999]. The former model is a grid point model, and the latter is a spectral model. Forget et al. [1999] found differences between the two types of models, especially above 50 km altitude, and commented that in general it is difficult to simulate this region of the Martian atmosphere due to lack of observations and poor knowledge of processes such as gravity wave drag, horizontal dissipation, and upper boundary conditions. Nonetheless, these authors obtained a winter polar warming with their model. Winter polar warmings are thought to occur when air from the cross-equatorial Hadley cell warms adiabatically as it descends over the poles [see e.g. Wilson, 1997].

Takahashi et al. [2003] built a model and found that at the equinoxes, the Hadley cells were asymmetric about the equator. They attributed the cause of this asymmetry to the mean north-south slope in surface elevation (known as the Martian topographic dichotomy). The cause of this result [and a similar one in the context of annually averaged circulation by Richardson and Wilson, 2002] will be discussed in detail in this thesis. Takahashi et al. [2003] do not take into account the seasonal atmospheric mass change from CO_2 condensation. The choice is justified by Haberle et al. [1993] who stated that the mass change does not significantly affect the zonal-mean circulation except at the lowest levels over the polar caps. Thermodynamically, the temperature cannot fall below the CO_2 condensation temperature, so when this is predicted to occur, the temperature is instantaneously snapped back to the CO_2 condensation

temperature.

Mouden and McConnell [2005] developed a model from the terrestrial Global Environmental Multiscale Model based on the Meteorological Service of Canada. This model extends well into the thermosphere (up to 170 km altitude), and includes physical parameterizations appropriate for these levels. The model also has the ability to run in "mesoscale" mode, where a small horizontal region has high resolution and the rest of the horizontal domain is run at coarser resolution. Using this nonuniform grid allows for the entire globe to be included in the calculation while not being too computationally expensive, thus avoiding the need for boundary conditions at the edges of the high resolution region. A mesoscale model is particularly useful on Mars where the range in surface topography is substantial.

Hartogh et al. [2005] redesigned the terrestrial Cologne Model of the Middle Atmosphere-Institute of Atmospheric Physics model for Martian conditions. These authors use their model to conclude that eddies are important in forcing winter polar warmings, much like Earth's stratospheric polar warmings. This is contrary to Wilson [1997] who suggested that thermal tides are the most influential in winter polar warmings and remarked on the contrast from the terrestrial case. Caution is warranted since at upper levels this model does not agree with other MGCMs, possibly due to the radiation scheme [R. J. Wilson, personal communication]. Meanwhile, Kuroda et al. [2009] concluded using their MGCM (described next) that dissipating thermal tides, planetary and resolved small-scale gravity waves and eddies were responsible for winter polar warmings in almost equal degree.

Kuroda et al. [2005] made a model based on the University of Tokyo/National Institute for Environmental Studies Center for Climate System Research atmospheric general circulation model. These authors specified a dust optical depth that depended on season, latitude, and pressure. The results with this dust distribution were compared to Viking and MGS TES results.

An important characteristic of MGCMs that should be mentioned is the extent of the vertical domain. The top layer in the model of Leovy and Mintz [1969] was at an altitude of 13.5 km. The first version of the NASA Ames MGCM [Pollack et al., 1981] had the top layer located at 15 km, while in the subsequent version [i.e. Pollack et al., 1990] the top layer was located at 47 km. Wilson and Hamilton [1996] extended the domain to 88 km in the GFDL model. In each model it was found that the circulation always extended throughout the model domain, and it has since been realized that the model top should be very high to capture the deep circulation in the Martian atmosphere (this requirement also holds for modeling of the terrestrial atmosphere). López-Valverde et al. [1998] concluded that non-local thermodynamic equilibrium effects become important above 80 km, and most modelers place their model top near or above this altitude rather than including these effects in the radiation scheme.

The MGCMs listed here have been vital in advancing our knowledge over time of the Martian atmosphere and are undergoing continual upgrades. Conversely, the MGCM described in Section 2.3 was chosen to be deliberately simple to isolate the effects of the Martian Hadley cells. By excluding physical processes of smaller importance to the Hadley circulation, the Martian circulation may be deconstructed in a computationally inexpensive way. The full MGCMs described in this section provide

an important guide and accuracy check, since at present observations of the Martian Hadley cell have been obtained.

1.3 Theories of the Hadley Circulation

The MGCM studies above revealed that Hadley cells are ubiquitous in the Martian atmosphere during all seasons. Near equinox, two Hadley cells are present. One cell is nearly always stronger and wider (in the north-south direction) than the other and spans the equator. The exact degree of the asymmetry depends not only on the season, but is also influenced by topography, as is discussed extensively in this thesis. Around the solstices, a single, cross-equatorial cell exists. Broad upwelling occurs in the summer hemisphere that extends to the summer pole (associated with a weak temperature gradient), while downwelling occurs in the winter hemisphere in the midlatitudes (associated with a strong temperature gradient). The circulation pattern tends to stay in a solstice configuration for most of the year, quickly transitioning through the equinox season to the opposite solstice.

Schneider and Lindzen [1977] and Schneider [1977] were the first to perform a quantitative study that focused on the Hadley circulation (of Earth). They assumed the system was asymmetric and neglected the effects of eddies, beginning with the zonally averaged Navier-Stokes equations on a sphere in the steady state and in hydrostatic balance. Parameterizations for the effects of small scale turbulent mixing and cumulus convection and friction were also included. The temperature at the bottom boundary was held fixed and depended only on latitude, which was meant to represent an ocean covered Earth. The model was thermally forced by Newtonian relaxation to an equilibrium temperature given by the annual mean heating that followed an adiabat in the troposphere and was isothermal in the stratosphere. The equations were solved on a numerical grid that spanned all latitudes and extended to various heights. These authors found that they could successfully reproduce the observed annual mean circulation when cumulus convection and friction were present, but could not when they were absent.

Held and Hou [1980] took a much more idealized approach to modeling the Hadley cells. They assumed a steady, axisymmetric, Boussinesq, hydrostatic, nearly inviscid set of equations on a sphere. Surface friction was given by a simple drag law. Diabatic heating was specified by Newtonian relaxation of temperature at a uniform rate toward a prescribed distribution of equilibrium temperature that is symmetric about the equator. Through consideration of the constraint of angular momentum conservation, they showed that the Hadley cell is confined to a finite region about the equator; poleward of the edge of the cell, there is no meridional circulation, and temperatures are in radiative equilibrium. By making arguments that the temperature is continuous at the cell boundary and that the net diabatic heating in each cell is zero, they were able to solve for the location of the cell edge and other characteristics of the circulation.

Lindzen and Hou [1988] solved the problem in the non-symmetric case, where the imposed equilibrium temperature maximum is located on the summer side of

the equator. They found strong sensitivity—with only a modest shift of the peak equilibrium temperature off the equator, the rising branch of the circulation shifted much further, and the resulting cross-equatorial cell was much stronger than the opposite cell in the summer hemisphere. Recently, Caballero et al. [2008] revised the Lindzen and Hou [1988] result using a more sophisticated, semi-gray specification of equilibrium temperature with the application to Mars or early Earth in mind. Their radiation scheme assumed a CO_2-like absorber, where absorption is zero everywhere outside of a narrow band at a single wavelength. Given the appropriate radiation parameters (i.e. total broadband optical depth, pressure broadening, and equivalent bandwidth), they derive an analytical solution for the Hadley cell width, depth, energy transport, and mass flux.

1.4 Topography as the Cause of Asymmetric Hadley Cells on Mars

Haberle et al. [1993] noted a factor of two difference in Hadley cell intensity between the two solstices using the NASA Ames Mars General Circulation Model (MGCM), which they attributed to the variation in the solar constant between these two seasons. However, Joshi et al. [1995] found that when the solar forcing was held constant between the two seasons, a factor of 1.5 difference in Hadley cell intensity was still present in the Oxford "intermediate" MGCM simulations. Wilson and Hamilton [1996] observed with the GFDL MGCM that the zonal mean component of topography inhibited Hadley cell intensity during northern hemisphere summer relative to southern hemisphere summer. Haberle et al. [1993] and Basu et al. [2006] remarked on the sensitivity of the Martian Hadley circulation to off-equatorial heating. Basu et al. [2006] also found that the relative strength of the circulation at the opposite solstices depends on dust loading.

Webster [1977] realized that elevated regions on Mars may act as local heat sources for the adjacent atmosphere, due to the fact that the (non-dusty) Martian atmosphere is effectively transparent to solar radiation. The near-surface temperature is therefore controlled by the surface temperature. Two recent studies have focused on the effects of the north-south slope in the zonally averaged topography on the Hadley circulation. Richardson and Wilson [2002] noted in the GFDL MGCM results that the annually averaged zonal mean circulation contained a stronger northern hemisphere Hadley cell, which also extended southward across the equator. They performed two further experiments in which the argument of perihelion was shifted by 180° (to test the effect of seasonal differences in the strength of the solar forcing) and in which the zonal mean component of topography was removed (leaving only the mountain or "wave" component). The removal of the zonal mean component of topography created two cells of nearly equal strength and shape, while the shift in the argument of perihelion produced little change from the full MGCM run. These results suggest that the north-south slope in topography is dominant, and the strength of the solar forcing is secondary.

Similarly, Takahashi et al. [2003] found that in their own MGCM results at equinox, the northern cell was stronger than the southern and extended across the equator into the southern hemisphere. They conducted three runs at perpetual equinox in which variations in only one of the following were included: topography, surface thermal inertia, and surface albedo. The runs with either surface thermal inertia only or surface albedo only did not match the control run with all three parameters, but the run with topography did. Two subsequent experiments in which either only the zonal mean component of topography or only the zonal wave component were included showed that, as in the study by Richardson and Wilson [2002], the zonal mean component of topography is the dominant factor in causing an asymmetric Hadley circulation.

Both Richardson and Wilson [2002] and Takahashi et al. [2003] concluded that the cause of the asymmetry was an upslope (i.e. southward) shift in the peak heating. Takahashi et al. [2003] went on to state that the convective heating term was the main influence in this shift. In this paper, we expand the analysis of the effects of convection and the north-south topographic slope to include other seasons, most notably the solstices. We also use not only a simple MGCM, but apply a modified version of the Hadley cell model of Lindzen and Hou [1988] that includes the effects of topography. To drive both of these models, we use a simple radiation scheme that assumes a gray atmosphere and no dust. While some aspects of the Martian atmosphere may be poorly represented by this assumption, we show that it captures the important aspects of Hadley-cell dynamics in Section 2.3.4 by comparing our scheme with the GFDL MGCM, which contains a non-gray radiation scheme. The gray radiation scheme has the advantage of being analytical (so that it can be used in the modified Lindzen and Hou [1988] model) and it allows us to formulate a conceptually simple description of Hadley cell dynamics in the presence of a north-south slope.

In Section 2.1, I develop the simple radiative transfer model that I use to calculate equilibrium temperature. The effects of convection are included in our radiative-convective model, but are not included in our "pure" radiative model. The equilibrium temperatures are used in Section 2.2, where I derive a model based on Lindzen and Hou [1988] that predicts the latitude of the dividing streamline and the poleward extent of the Hadley cells in the presence of nonzero topography. I use this model to solve for the boundaries of the Hadley cells with and without the zonal mean component of topography, but also explicitly as a function of season (recall that Richardson and Wilson [2002] concentrated their study on the annual average, Takahashi et al. [2003] on equinox). In Section 2.3 I present a simple MGCM and compare it to the modified Lindzen and Hou [1988] model in Section 2.4.

As shown by Webster [1977] and others, the longitudinally varying topography produces zonal asymmetries in the circulation. Elevated regions of topography near the equator cause zonally asymmetric diabatic heating that have the potential to drive Walker-like or monsoon-like circulations. These concepts will be explored in Chapter 3

1.5 Pluto's Atmosphere

Pluto's small size and large distance from the Sun make it a difficult object to observe. Early interpretation of Pluto spectra [Cruikshank et al., 1976; Fink et al., 1980; Buie and Fink, 1987] indicated CH_4 bands, but determining the relative proportions of gas and surface frost in an atmospheric column remained elusive. Brosch [1995] claim to have observed a stellar occultation by Pluto on 19 August 1985, although the observing conditions were very poor. They concluded that the primary atmospheric constituent was "probably" N_2, CO, or CH_4. The first high quality stellar occultation by Pluto was observed on 9 June 1988 at several locations in Australia and by the Kuiper Airborne Observatory (KAO) [Hubbard et al., 1988; Elliot et al., 1989; Millis et al., 1993]. Model fits to the KAO light curve, which had the highest SNR per scale height[1], yielded half-light radius and the scale height at the half-light level. Deriving a temperature required an assumption about the mean molecular weight of the atmosphere; under the assumption of pure CH_4, the temperature at the half-light level was 67 ± 6 K.

Yelle and Lunine [1989] developed a radiative-conductive model that included the effects of heating by the CH_4 3.3 μm band, cooling by the CH_4 7.6 μm band, and thermal conduction. Using the solution for temperature obtained from their calculation, they argued that Pluto's atmosphere must contain some heavier molecule or molecules to be consistent with the scale height obtained by Elliot et al. [1989]. Yelle and Lunine [1989] suggested CO, N_2, and argon as the most suitable candidates. Subsequent measurements by Owen et al. [1993] of solar reflection spectra in the near IR revealed the presence of surface ice composed of CO, N_2 and CH_4 (but not CO_2 as had been observed on Neptune's moon Triton, Pluto's sister atmosphere). Moreover, the N_2 ice was more abundant than the other two by a factor of 50. If the ices were in vapor pressure equilibrium with the surface, the relatively large abundance of N_2 ice implies that the atmosphere must also be predominately N_2.

A quite puzzling feature, even to this day, in the KAO light curve is a kink at the 40% normalized flux level, at which point the light curve flux suddenly starts decreasing more sharply with time. Light curve data are ambiguous in that the flux may diminish either due to extinction of the starlight by an optically thick constituent in the atmosphere or due to a change in the refractivity (and hence spreading of the light rays) caused by a change in the temperature gradient. Elliot et al. [1989] included an optical depth that varied exponentially with height in the light curve model used to analyze the 1988 KAO data. The haze was described by the radius of the top of the haze layer, the radius of optical depth unity, and the scale height of the haze. Stansberry et al. [1989] investigated possible mechanisms for haze production, but found they needed physical parameters, specifically the CH_4 dissociation rate and absorption strength, to be beyond reasonable limits (based on other hazes in the outer solar system).

Hubbard et al. [1990] used a model similar to Yelle and Lunine [1989] to show that

[1]Light curve noise is evaluated in terms of the SNR per scale height, i.e. the SNR in the time that the shadow moves a distance of 60 km (approximately one pressure scale height). This quantity corrects for different shadow velocities.

under the right conditions, namely a strong temperature inversion near the surface and an isothermal atmosphere above, a kink could be produced without invoking the haze argument. Lellouch [1994] revised this calculation, updating the relative atmospheric abundances from the results of the ice spectra observations of Owen et al. [1993]. Stansberry et al. [1994] used an idealized temperature profile, which they adjusted to fit the properties of the light curve. They found that the temperature gradient in the inversion region must be 30 K km^{-1} to reproduce the kink in the 1988 KAO light curve. They also were the first to examine the possibility of a troposphere, the depth and lapse rate of which could be constrained by the minimum flux and the absence of caustic spikes in the 1988 KAO light curve. Strobel et al. [1996] presented another radiative-conductive model, based on physical arguments. They added CH_4 heating in the 2.3μm band and CO cooling (over several bands) to the CH_4 heating at 3.3 μm and cooling at 7.6 μm, but found they were not able to achieve the steep stratospheric gradient required by Stansberry et al. [1994].

A second set of occultations was observed on 20 July 2002 and 21 August 2002 [Elliot et al., 2003b; Sicardy et al., 2003; Pasachoff et al., 2005] that resulted in more questions than answers. First, the kink had disappeared; second, the half-light radius had increased, implying a factor of two increase in the surface pressure. Moreover, Elliot et al. [2003b] noted a wavelength dependence in the 21 August 2002 occultation data that was too large to be due to the dependence of N_2 refractivity on wavelength, and was thus attributed to a wavelength-dependent haze extinction.

From a subsequent stellar occultation observed on 12 June 2006 by Elliot et al. [2007] and by Young et al. [2008a], the analyses showed only subtle changes in atmospheric structure from the 2002 observations. Another stellar occultation on 18 March 2007 observed by Person et al. [2008] showed that the atmosphere was essentially unchanged from the 2006 occultation. Meanwhile, Olkin et al. [2009] showed a 28% increase in pressure at a reference radius of 1275 km between their observations of the 31 July 2007 occultation and the 12 June 2006 occultation [observed by Young et al., 2008a]. Adding further to the haze issue, Young et al. [2008b] observed no wavelength dependence in their observations of the 31 July 2007 occultation at 0.5 and 0.8 μm.

The light curve obtained on 18 March 2007 at the Multiple Mirror Telescope Observatory (MMT) had a very high SNR per scale height, and contained variations during immersion and emersion that were identified as waves in Pluto's atmosphere. What is remarkable is that each half of the light curve was nearly identical, indicating coherent wave structures between both limbs of Pluto's disk visible at the time of the occultation. Person et al. [2008] interpreted the waves as Rossby waves and calculated an upper limit for the zonal wind speed of 3 m s^{-1} based on the critical velocity required for vertical propagation. However, Hubbard et al. [2009] provided evidence that the waves are instead gravity waves.

1.6 Techniques for Analyzing Stellar Occultation Data

Baum and Code [1953] developed a light curve model to analyze their data from an occultation by Jupiter. Their model considered the effects of refraction of starlight by the atmosphere in the limit of geometric optics. They mention the possibility of atmospheric extinction, but reason that the path length through the atmosphere is too short for any significant attenuation to occur. They proceeded under the assumptions that the atmosphere is spherical and isothermal, that its depth is small compared to the radius of the planet (so that gravity does not vary with height), and that the angular size of the occulted star is small compared with the atmospheric scale height. Their model then describes the atmosphere by a single parameter, the inverse of the scale height, if the composition of the atmosphere, relative velocity between observer and occulting body, and gravitational acceleration on the occulting body are known.

Elliot and Young [1992] made a more sophisticated light curve model for small planets, motivated by the 1988 Pluto occultation data. They include the effects of atmospheric extinction using a specification similar to the one mentioned above used by Elliot et al. [1989]. They also include the geometrical effect of focusing of light rays when the observer is near the shadow center, which is what produces the central flash sometimes observed in occultation data [Elliot et al.]. Moreover, the gravitational acceleration is no longer assumed constant with height.

At the time of the model's inception, the functional form of the temperature variation with height was not known, in part because the composition of the atmosphere was not known. As such, these authors chose to use a temperature of the form

$$T(r) = T_H \left(\frac{r}{r_H} \right)^b , \tag{1.2}$$

where r is radius from the center of the body, T_H is the temperature at the half-light radius r_H, and b is the temperature power index. The power law form (rather than e.g. a linear expansion) was chosen for mathematical simplicity. They assume that the composition (i.e. mean molecular weight) of the atmosphere also varies with height according to a power law (with a different power index), but a vertically varying mean molecular weight has yet to be applied to data since it is difficult to make a physical argument that such a situation exists on Pluto (or any solar system body for that matter). The equation for temperature with height is then related to the refraction angle (dependent on the refractivity derivative) by assuming the ideal gas law, hydrostatic balance, and a linear relationship between refractivity and number density.

Occultations typically do not probe the entire depth of the atmosphere, and (1.2) is a good approximation to a region of the atmosphere where the temperature gradient is not varying substantially. For instance, if one were observing an occultation of a planet with an atmosphere identical to Earth's, (1.2) would hold in the middle of the stratosphere or mesosphere, but would not be a good representation at the tropopause or stratopause. The most current models of Pluto's atmosphere [e.g.

Strobel et al., 1996] show that there are two distinct regions, a stratosphere where the temperature increases with height and a mesosphere (for lack of a better term) where the temperature is either isothermal or decreasing (depending on the amount of cooling present from CO). The region probed by occultations seems to be near or at the boundary between these two different temperature gradients, and the shape of the temperature profile may not be accurately described by the Elliot and Young [1992] model.

Rather than make an assumption about the temperature variation with height, it is also possible to "invert" the light curve. This technique was first introduced by Kovalevsky and Link [1969] for stellar occultations by large planets, and was not extended to small planets until much later by Elliot et al. [2003a]. As in Elliot and Young [1992], they generalized the technique to include gravitational acceleration varying with height and effects from the curvature of the limb (i.e. the focusing effect). One drawback of this method is that it requires a clear atmosphere assumption (or that the optical depth due to extinction is independently known), which is questionable in light of Pluto's uncertain haze properties.

Specifically, the Elliot et al. [2003a] inversion method uses geometrical arguments, hydrostatic balance, the ideal gas law, and the linear dependence of number density on refractivity to cast the expression for temperature as a function of height in terms of various integrals. These integrals are integrated downward from the top of the atmosphere to the desired radius, and as such require a top boundary condition. In principle, independently obtained data could be used, but rarely is this available simultaneously with the occultation measurement. The suggested method for determining the boundary condition is to least-squares fit the top portion of the light curve using the Elliot and Young [1992] model and invert the remaining portion. Using the Elliot and Young [1992] model can introduce systematic errors if it does not accurately represent the atmosphere, however. In general, any error in the boundary condition will affect the inverted temperature.

Zalucha et al. [2007] devised a method for determining temperature from spikes in the light curve caused by density fluctuations in the atmosphere (with application to an occultation by Titan). The method requires multi-wavelength observations taken at the same location in the shadow plane. From the time delay between spikes at different wavelengths (a direct result of the slight dependence of refractivity on wavelength), information about the refraction angle was obtained, instead of obtaining it from the light curve flux. This method also requires an upper boundary condition, namely the Elliot and Young [1992] model, and a high enough time resolution to resolve the spikes. The MMT data are colocated, multi-wavelength observations and show oscillations, but do not show a time delay between the light curves of different wavelengths required to use the spikes method of Zalucha et al. [2007]. Apparently the conditions on Pluto or during the 2007 occultation event are unsuitable for this method, possibly because the path of the star only grazed Pluto's atmosphere. Spike delay decreases with height, so perhaps a the delay was undetectable at the altitudes that the occultation probed.

In Chapter 4, I take a new approach to obtaining the atmospheric temperature profile from occultation light curves using an atmospheric radiative-conductive model

based on that of Strobel et al. [1996]. Given a set of atmospheric parameters, namely surface temperature, pressure, and radius and mixing ratios of CH_4 and CO (with respect to an N_2 atmosphere), temperature as a function of radius is found by numerically solving the one-dimensional heat balance equation assuming radiative equilibrium, which includes the effect of heating and cooling by the specified amounts of CH_4 and CO. The corresponding refractivity and its vertical derivatives are subsequently computed at discrete points within the parameter space and interpolated, such that a light curve may be calculated quickly for an arbitrary point in the domain. I then perform a least-squares fit with the light curve data to obtain best-fit parameters. This method directly links the light curve data with a comprehensive radiative transfer calculation that predicts atmospheric structure based on physical properties of the atmosphere, rather than an idealized temperature structure or a boundary condition containing one.

In Section 4.1, I describe the radiative-conductive model and the procedure for calculating light curves. I also demonstrate the effects of various atmospheric parameters on the light curve. In Section 4.2, an overview of the light curve data is given and results from the least-squares fits are presented. I analyzed data from the following five events: 9 June 1988, 21 August 2002, 12 June 2006, 18 March 2007, and 24 June 2008. A discussion of my analysis and comparison of results to other work is given in Section 4.3.

The analysis described in Chapter 4 is conducted under the condition of radiative equilibrium. The global circulation of Pluto's atmosphere has yet to be assessed, but it is likely that atmospheric circulation plays at least some role in determining Pluto's temperature and pressure. In Chapter 5, I demonstrate with a simple Pluto GCM (PGCM) that Pluto's circulation is important for further study.

Table 1.1: The Composition of the Martian Lower Atmosphere

Gas	Abundance	Notes
CO_2	95.32%	···
N_2	2.7%	···
^{40}Ar	1.6%	···
O_2	0.13%	···
CO	0.07%	···
H_2O	0.03%	Variable with season and location
$^{36+38}Ar$	5.3 ppm	···
Ne	2.5 ppm	···
Kr	0.3 ppm	···
Xe	0.08 ppm	···
O_3	0.04–0.2 ppm	Variable with season and location

Table 1.2: Basic Planetary Constants for Mars

Parameter	Value	Units
Surface radius	3394	km
Surface gravity	3.72	m s^{-2}
Mean molecular weight	43.4	g $mole^{-1}$
Molecular gas constant	192	J K^{-1} kg^{-1}
Specific heat at constant pressure	860	J K^{-1} kg^{-1}
Solar day (sol)	88775	s
Rotation rate	7.088	$\times 10^{-5}$ s^{-1}
Year length	669 (687)	sols (Earth days)
Orbital eccentricity	0.093	···
Orbital inclination	25	°
Sun-planet distance at perihelion (aphelion)	1.38 (1.67)	AU
Surface pressure range due to seasonal variations	6–8	mb
Planetary equilibrium temperature	210	K
Mean scale height	10.8	km
Brunt-Väisälä frequency	~ 0.60	10^{-2} s^{-1}
Adiabatic lapse rate	4.5	K km^{-1}
Radiative damping time (lower atmosphere)	~ 2	sols
Specific latent heat (of CO_2)	590	kJ kg^{-1}

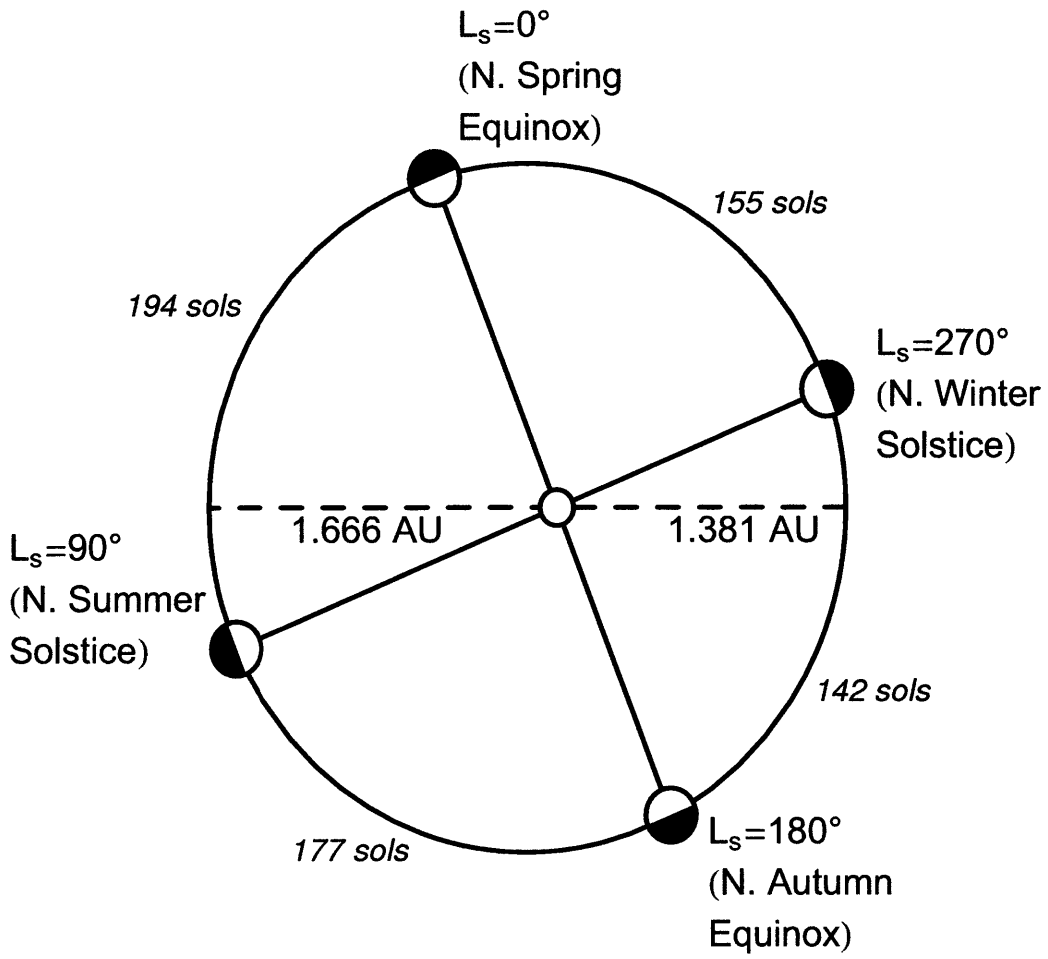

Figure 1-1: A diagram of the orbit of Mars illustrating the seasonal asymmetries [after Michaux, 1967]. The orbital semimajor axis is 1.52 AU and the orbital eccentricity is 0.093. By convention, Martian seasons are measured in angular units of L_s with L_s= 0° corresponding to the northern hemisphere spring equinox, L_s= 90° to the northern hemisphere summer solstice, L_s= 180° to the autumn equinox, and L_s= 270° to the winter solstice. The seasonal asymmetry is such that the northern hemisphere summer is longer than southern hemisphere summer. The term sol refers to a Martian solar day.

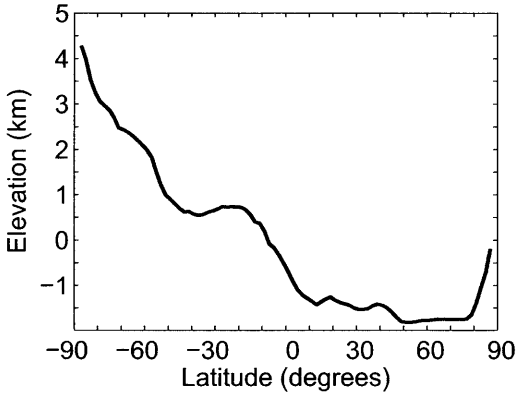

Figure 1-2: Zonally averaged Martian topography measured by the Mars Orbiter Laser Altimeter (MOLA) instrument [Smith et al., 1999]. Martian topography slopes downwards from the southern hemisphere to the northern hemisphere.

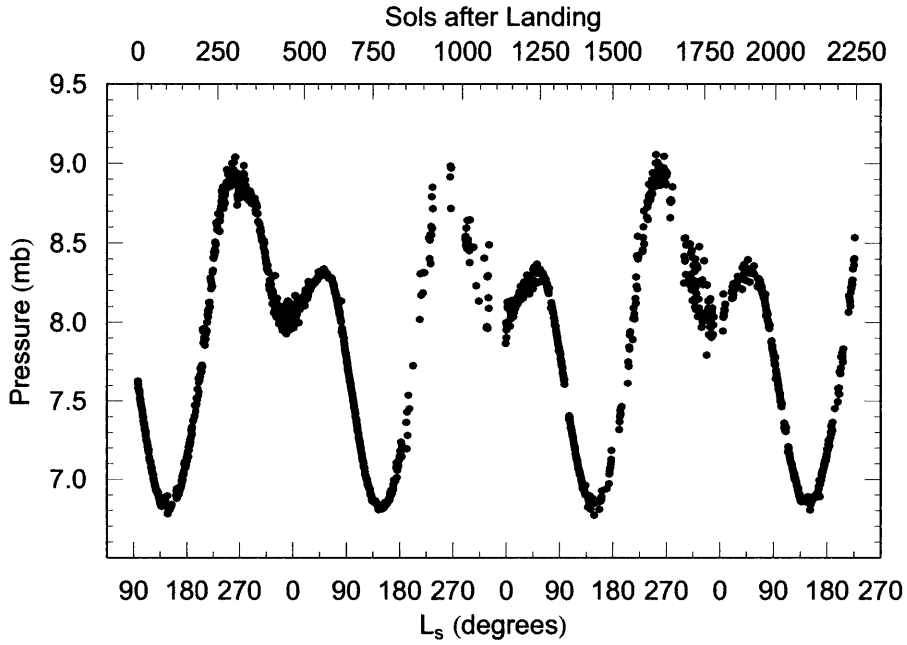

Figure 1-3: Daily averaged surface pressure at Viking Lander 1, located at 22°.5N, 48°W. During winter, CO_2 freezes out of the atmosphere into a seasonal ice cap, causing a decrease in surface pressure. The difference in the depth of the minima arises from the longer southern winter [data from Tillman, 1989].

Chapter 2

An Analysis of the Effect of Topography on the Martian Hadley Cells

2.1 Calculation of Equilibrium Temperature

In both the modified Lindzen and Hou [1988] model (Section 2.2) and the simple MGCM (Section 2.3), the external thermal forcing is applied through Newtonian relaxation to a radiative equilibrium state, represented by the equilibrium temperature T_{eq}. An atmosphere in radiative equilibrium by definition has no motion associated with it. Radiative equilibrium temperature is usually calculated from a radiative transfer scheme, whether it be a comprehensive model that includes heating and cooling from many spectral lines [e.g. the Strobel et al., 1996, model described in Section 4.1.1] or a simple gray model as described below. Radiative equilibrium temperature is a proxy for the diabatic heat source and does not correspond to a physical state that can be measured (except in the case of a motionless atmosphere, which has yet to be discovered). Newtonian relaxation to radiative equilibrium temperatures is a technique very commonly employed in terrestrial atmospheric models [e.g. Held and Suarez, 1994], and is accepted as a good approximation to driving a GCM directly with the diabatic heating and cooling rates calculated at each location.

A conceptually simple radiation scheme has been deliberately chosen here in order to more clearly understand its effect on the results. The experiments use two types of equilibrium configurations. The first is referred to as pure radiative equilibrium. Assuming the Eddington approximation, no dust, no scattering, no solar absorption by the atmosphere, and a gray atmosphere in the long wave, the solution to the radiative transfer equation is

$$\sigma T_{eq,R}\left(\phi, L_s, p\right)^4 = \begin{cases} Q_o\left(\phi, L_s\right)\left[0.5 + 0.75\tau\left(p\right)\right] & \tau \neq \tau_o \\ Q_o\left(\phi, L_s\right)\left[1 + 0.75\tau_o\left(p_o\left(\phi\right)\right)\right] & \tau = \tau_o, \end{cases} \tag{2.1}$$

where $T_{eq,R}$ is the pure equilibrium temperature, σ is the Stefan-Boltzmann constant,

ϕ is latitude, L_s is the ecliptic longitude of the Sun (in Mars-centered coordinates), p is pressure, Q_o is the daily averaged net solar flux, τ is the optical depth, and τ_o is the optical depth at the surface. Under the assumption of constant opacity, $\tau(p) = p\tau_{oo}/p_{oo}$, where p_{oo} is a reference pressure set to the mean surface pressure of 6 hPa, and τ_{oo} (here taken to be 0.2) is the optical depth at p_{oo}. Likewise $\tau_o(p_o(\phi)) = p_o(\phi)\tau_{oo}/p_{oo}$, where p_o is the height of the surface in pressure coordinates. A temperature discontinuity exists between the surface and the atmosphere directly above the surface. Note that τ increases downward.

From Peixoto and Oort [1992],

$$Q_o(\phi, L_s) = \frac{S_o}{\pi}(1-A)\left[\frac{1+e\cos(L_s - L_{sp})}{1-e^2}\right]^2 (\xi \sin\phi \sin\delta + \sin\xi \cos\phi \cos\delta), \quad (2.2)$$

where $S_o = 600$ W m^{-2} is the mean solar constant, A is the albedo (set to a constant value of 0.15), $e = 0.0934$ is the orbital eccentricity, $L_{sp} = 252°$ is the L_s of perihelion (located near northern winter solstice), δ is the declination of the Sun (in Mars-centered coordinates), and ξ is the hour angle[1] of sunrise and sunset. Furthermore, $\cos\xi = -\tan\phi\tan\delta$, and $\sin\delta = \sin i \sin L_s$, where $i = 25°$ is the obliquity. The square of the term in brackets in (2.2) represents the correction to S_o due to changing distance from the Sun in an elliptical orbit. For Earth, this quantity varies from 0.968 to 1.069 between perihelion and aphelion, respectively, while for Mars it varies from 0.837 to 1.217.

The second prescribed equilibrium state is radiative-convective equilibrium, in which the temperature above the convective layer is the same as in the pure radiative equilibrium state, and the temperature within the convective layer follows an adiabat. Thus,

$$\sigma T_{eq,RC}(\phi, L_s, p)^4 = \begin{cases} Q_o(\phi, L_s)\,[0.5 + 0.75\tau(p)] & \tau < \tau_t \\ Q_o(\phi, L_s)\,[0.5 + 0.75\tau_t(\phi)]\,[\tau(p)/\tau_t(\phi)]^{4R/c_p} & \tau \geq \tau_t, \end{cases} \quad (2.3)$$

where $T_{eq,RC}$ is the radiative-convective equilibrium temperature, τ_t is the optical depth of the top of the convective layer, R is the specific gas constant, and c_p is the specific heat at constant pressure. The height of the convective layer is calculated by requiring continuity of temperature and radiative flux (surface plus atmosphere) at τ_t. Explicitly,

$$\sigma T_{eq,R}^4(\tau_o)\exp\left[-(\tau_o - \tau_t)/\mu\right] + \int_{\tau_t}^{\tau_o} \sigma T_{eq,R}^4(\tau_*)\exp\left[-(\tau_* - \tau_t)/\mu\right] d\tau_* \quad (2.4)$$
$$= \sigma T_{eq,RC}^4(\tau_o)\exp\left[-(\tau_o - \tau_t)/\mu\right] + \int_{\tau_t}^{\tau_o} \sigma T_{eq,RC}^4(\tau_*)\exp\left[-(\tau_* - \tau_t)/\mu\right] d\tau_*$$

[1]Declination is the equivalent of latitude on the sky, measured from the celestial equator (the projection of the planet's equator onto the sky). Hour angle is the angle between a celestial object and the observer's meridian (line between the north and south celestial poles, the projection of the planet's north and south poles on the sky) where positive indicates the object has transited.

where $\mu = 2/3$ is the average cosine of the emission angle and τ_* is a variable of integration. Substitution of (2.1) and (2.3) for $T_{eq,R}$ and $T_{eq,RC}$, respectively in (2.4) shows that τ_t is a function of only R, c_p, and τ_o (i.e. the height of the surface). The key difference between $T_{eq,R}$ and $T_{eq,RC}$ is that for the latter, the equilibrium temperature aloft (within the convective layer) depends on the height of the surface, while the former does not.

The Martian atmosphere follows a seasonal cycle in which atmospheric CO_2 freezes out during the winter, causing the surface pressure to vary about its annually averaged value by over 1 hPa [e.g. Hess et al., 1980]. Haberle et al. [1993] showed (as did later versions of my model that included mass and surface albedo changes from CO_2 condensation and sublimation) that the mass change does not significantly affect the zonal-mean circulation except at the lowest levels over the polar caps; therefore, I have chosen to keep atmospheric mass constant. When T_{eq} falls below the CO_2 condensation temperature T_{co2}, it is instantaneously reset to T_{co2}. From the Clausius-Clapeyron equation,

$$T_{co2} = \left[\frac{1}{T_1} - \frac{R}{L}\ln\left(\frac{p}{p_1}\right)\right]^{-1}, \tag{2.5}$$

where $T_1 = 136.6$ K is the reference temperature at the reference pressure $p_1 = 1$ hPa [James et al., 1992], p is in hPa, $L = 5.9 \times 10^5$ J kg^{-1} is the specific latent heat of sublimation, and T_{co2} is given in K.

Figures 2-1 and 2-2 show zonally averaged $T_{eq,R}$ and $T_{eq,RC}$ given by (2.1) and (2.3), respectively, for $L_s = 0°$, $L_s = 90°$, and $L_s = 270°$. The following three topographies are considered: flat topography at zero elevation ("flat"), Mars Orbiter Laser Altimeter (MOLA) topography ("full"; Fig. 2-3a), and zonal mean MOLA topography ("mean"; Fig. 2-3b). For the pure radiative case, T_{eq} does not vary between the different topographies—it is as if the surface has been pasted onto the temperature profile. Conversely, the surface modifies the equilibrium temperature aloft in the radiative-convective case. The equilibrium temperature contours appear to be pushed up by the higher surface, changing the meridional temperature gradient so that the equilibrium temperature is higher above an elevated surface.

My values for $T_{eq,R}$ (and hence $T_{eq,RC}$) at high altitudes (not shown) are warmer and more isothermal than the corresponding values for $T_{eq,RC}$ plotted in Joshi et al. [1995] and Haberle et al. [1997]. While these authors use different radiative transfer models, the discrepancy is likely a result of the choice of τ_{oo} and the gray atmosphere assumption, which is not fully accurate for Mars. Hinson et al. [2008] observed in radio occultation data that the depth of the mixed layer varies with elevation, an effect that is not captured in my model. Caballero et al. [2008] derive a radiative-convective model for a semi-gray atmosphere, which they apply to Mars. Their predicted height of the convective layer in σ-coordinates (p/p_o) is 0.44 compared to my value of 0.51 for flat topography. Note that in the gray and semi-gray assumptions the height of the convective layer is independent of season, in contrast with other models and measurements [e.g. Haberle et al., 1993].

Figure 2-4 shows $T_{eq,R}$ and $T_{eq,RC}$ at a constant pressure level of 3.8 hPa or 5 km

log pressure height, which is within the convective layer. It is evident that topography changes the meridional gradient of $T_{eq,RC}$ (compare heavy solid and heavy dashed lines). For flat topography, $T_{eq,RC}$ is offset to higher temperature from $T_{eq,R}$, since in the former, convection acts to redistribute heat from the surface into the convective layer. Again, in pure radiative equilibrium, a temperature discontinuity exists between the surface and the atmosphere directly above the surface. The radiative-convective equilibrium temperature profile follows a dry adiabat that is continuous with the surface temperature.

Figure 2-5 shows a diagram of the two different types of T_{eq}. The gray and black curve is the pure radiative equilibrium solution for T_{eq} as a function of pressure and is the same regardless of surface height. If the surface is located at some elevation p_o, located at the level of the black, solid, horizontal line, then the pure radiative equilibrium surface temperature is given by T_g (black text). If the surface is then located at some higher elevation (lower pressure), represented by the gray, solid, horizontal line, the pure radiative equilibrium surface temperature (T_g in gray text) will decrease because of the reduced greenhouse effect. In an optically thin atmosphere such as Mars, however, this effect is extremely small, and the surface temperature can be considered independent of surface height.

The dashed lines in Fig. 2-5, drawn for both surface elevations, represent adiabats calculated such that the convective layer remains in energy balance with the rest of the atmosphere. Comparing the radiative-convective equilibrium temperatures at some pressure level p_a within the convecting layer shows that they are higher above the elevated surface than over the lower surface. The radiative-convective equilibrium temperature profiles are being evaluated at different relative heights above the local surface (the primary heating element for the atmosphere), which dominates over the reduced greenhouse effect at the higher altitude. In this way, the height of the surface modifies the heating profile of the lower atmosphere. Moreover, the change in surface temperature due to the reduced greenhouse effect at higher elevations is again negligible, varying by less than 3 K for a difference in elevation of 5 km.

In the radiative-convective model described here, the atmospheric temperature evaluated at the surface is equal to the temperature of the surface itself. In reality, the surface temperature and the temperature of the shallow atmospheric layer directly above the surface (i.e. the surface layer) may still be warmer. Within the surface layer, mechanical production of turbulence by flow over the surface can transport heat upward and outweigh buoyant (convective) transport of heat. The difference between the surface temperature and the atmospheric temperature above the surface layer may be assessed using boundary layer similarity theory. The functional dependence of boundary layer variables on each other is difficult to predict using first principles, and so relationships between variables are empirically determined from data. The relationships often have similar forms, hence the term similarity theory.

Boundary layer similarity theory provides the relation [e.g. Sutton et al., 1978]

$$B = -\rho c_p C_d C_h ||\mathbf{v}|| \Delta\Theta_s, \tag{2.6}$$

where B is the convective flux (upward positive), ρ is the air density, c_p is the specific

heat of the air at constant pressure, C_d is the drag coefficient, C_h is the heat transfer coefficient, $||\mathbf{v}||$ is the magnitude of the horizontal surface wind, and $\Delta\Theta_s$ is the potential difference between the atmosphere (above the surface layer) and the ground. The drag and heat transfer coefficients are given by [following Sutton et al., 1978]

$$C_d = \kappa \left[\int_{\zeta_o}^{\zeta} \zeta^{-1} \Psi_m(\zeta) d\zeta \right]^{-1} \tag{2.7}$$

and

$$C_h = \kappa \left[\int_{\zeta_o}^{\zeta} \zeta^{-1} \Psi_h(\zeta) d\zeta \right]^{-1}, \tag{2.8}$$

where $\zeta = z/l$, $\zeta_o = l_o/l$, z is height, κ is von Kármán's constant (0.4), and Ψ_m and Ψ_h are defined below. The Monin-Obokhov length l is physically interpreted as being proportional to the height above the surface at which buoyant factors first dominate over mechanical (shear) production of turbulence [Stull, 1988]. A negative value indicates unstable conditions, while a positive value indicates stable conditions. Martínez et al. [2009] estimate the diurnal average of l to be -17 m for Mars based on Viking Lander 1 and 2 and Pathfinder measurements, which is consistent with values for Viking Lander 1 and 2 measurements from Sutton et al. [1978]. Buoyant and shear forces become comparable at height $z = -0.5l$, and so I chose to evaluate C_d and C_h at that value. The roughness length l_o for Mars is not precisely known. Sutton et al. [1978] found l_o between 0.1 and 1 cm; Tillman et al. [1994] found the range between 0.1 to 0.3 cm with preference for 0.1 cm. Larsen et al. [2002] also found 0.1 cm. Thus, I have also chosen $l_o = 0.1$ cm. I have chosen to follow the Sutton et al. [1978] specification of $\Psi_m(\zeta)$ and $\Psi_h(\zeta)$, which is (for a statically unstable boundary layer)

$$\Psi_m = (1 - 15\zeta)^{-1/2} \tag{2.9}$$

$$\Psi_h = 0.74(1 - 9\zeta)^{-1/2}. \tag{2.10}$$

The value of $C_d \times C_h$ is $\sim 3 \times 10^{-3}$ using these assumptions.

The convective flux is given by the gray radiative equilibrium model described above

$$B = \int_{\tau}^{\tau_o} \sigma(T_{eq,RC}^4(\tau_*) - T_{eq,R}^4(\tau_*)) \exp\left[-(\tau_* - \tau)/\mu\right] d\tau_*, \tag{2.11}$$

where τ is evaluated at the value that corresponds to $z = -0.5l$. $||\mathbf{v}||$ is obtained from the lowest level of the (zonally and temporally averaged) results with flat topography from the MGCM described in Section 2.3.1. The lowest level is at an altitude of 100 m, where the wind is much higher than what probably exists at the surface due to the increased frictional drag.

Figure 2-6 shows $\Delta\Theta_s$ vs. latitude for L_s=0, 90, and 270°. By definition, $\Delta\Theta_s$ is negative for a warmer surface temperature and varies inversely with $||\mathbf{v}||$. Several sharp minima are present where $||\mathbf{v}||$ is small at the latitudes of the sinking branch of the Hadley cell (located at ±45° for L_s=0°, -50° for L_s=90°, and 40° for L_s=270°),

and a broader band of relatively lower values are present at the latitudes of the rising branch (0° for L_s=0°, 45 to 90°for L_s=90°, and -45 to -90°for L_s=270°). The magnitude of $\Delta\Theta_s$ is small, suggesting that the assumption of equal atmospheric and surface temperature at the surface made in the gray radiative-convective model above is valid.

Sutton et al. [1978] found $\Delta\Theta_s$ to be 10 K at night, lowering to a daytime minimum of -28 K from Viking Lander 1 and 2 measurements combined with a model for surface temperature. One possible reason for the large discrepancy between these values and Fig. 2-6 is that the measured surface wind speeds were lower than my MGCM wind speeds, which are taken from much higher aloft. Another reason is that my calculation uses daily averaged flux, whereas the measured flux exhibits a drastic diurnal cycle. The assumption of diurnally averaged solar flux results in a low level of convective flux all of the time, while in the true atmosphere, the convective activity will be concentrated during a shorter period during the day.

2.2 Hadley Cell Model with Topography

Here I follow the analysis of Lindzen and Hou [1988], modifying the problem to permit varying height of the surface and the equilibrium temperatures as discussed in Section 2.1. A schematic is shown in Fig. 2-7. The Hadley cells are confined between latitudes ϕ_+ and ϕ_-, with the dividing streamline at ϕ_1. The height of the surface as a function of latitude ϕ is given by $z_b(\phi)$. Non-axisymmetric effects are ignored. The governing principles are as follows: conservation of absolute angular momentum

$$M(\phi) = \Omega a^2 \cos^2\phi + u(\phi, z) a \cos\phi \tag{2.12}$$

at upper levels, where z is height, Ω is the planetary rotation rate, u is the zonal wind, and a is the planetary radius; gradient wind balance

$$2\Omega \sin\phi\ u + \frac{1}{a}\tan\phi\ u^2 = -\frac{1}{a}\frac{\partial\Phi}{\partial\phi}, \tag{2.13}$$

where Φ is geopotential; hydrostatic balance

$$\frac{\partial\Phi}{\partial z} = g\frac{\Theta}{\Theta_o}, \tag{2.14}$$

where g is the acceleration of gravity at the surface, Θ is potential temperature, and Θ_o is a constant reference temperature (note that in the Boussinesq approximation, temperature and potential temperature are the same); and the steady thermodynamic equation

$$\frac{v}{a}\frac{\partial\Theta}{\partial\phi} + w\frac{\partial\Theta}{\partial z} = -k_T\left(\Theta - \Theta_e\right), \tag{2.15}$$

where k_T is the radiative relaxation rate, Θ_e is equilibrium potential temperature, and v and w are the meridional and vertical velocities, respectively.

Now, consider the dividing streamline at $\phi = \phi_1$. Assuming the zonal flow near the surface is weak, the air rises out of the boundary layer with angular momentum $M_0 = \Omega a^2 \cos^2 \phi_1$, from (2.12). Conservation of angular momentum then dictates that everywhere along this streamline (outside the boundary layer) $M(\phi, z)$=M_0, where M_0 is a constant; hence, within each cell and along the top of the model at $z = h$, (2.12) requires that

$$u(\phi, h) = \Omega a \frac{(\cos^2 \phi_1 - \cos^2 \phi)}{\cos \phi}. \tag{2.16}$$

At $z = z_b(\phi)$, assume (again following Held and Hou) that u is much weaker than at the top, such that subtracting (2.13) applied at $z = z_b$ from that applied at $z = h$ and substituting from (2.16) gives

$$\begin{aligned} \Omega^2 a^2 \frac{\sin \phi}{\cos^3 \phi} \left(\cos^4 \phi_1 - \cos^4 \phi\right) &= -\left.\frac{\partial \Phi}{\partial \phi}\right|_{z=h} + \left.\frac{\partial \Phi}{\partial \phi}\right|_{z=z_b} \\ &= -\frac{\partial}{\partial \phi}\left[\Phi(\phi, h) - \Phi(\phi, z_b)\right] - \frac{dz_b}{d\phi}\left.\frac{\partial \Phi}{\partial z}\right|_{z=z_b}. \end{aligned} \tag{2.17}$$

Using (2.14) and its vertical integral, and integrating in ϕ, we obtain

$$\frac{g}{\Theta_o}\int_{z_b}^{h} \Theta \, dz + \frac{g}{\Theta_o}\int_{\phi_c}^{\phi} \Theta(\phi', z_b)\frac{dz_b}{d\phi'} \, d\phi' = \hat{\Phi} - \frac{\Omega^2 a^2}{2}\left(\cos^2 \phi + \frac{\cos^4 \phi_1}{\cos^2 \phi}\right), \tag{2.18}$$

where the second integral is along the boundary starting at an arbitrary latitude ϕ_c, ϕ' is a variable of integration, and $\hat{\Phi}$ is a constant of integration to be determined.

Next we apply the conditions invoked by Held and Hou [1980]. Since Φ must be continuous at the edges of the cells, both at $z = h$ and z_b (assuming that z_b is continuous), it follows from (2.14) that the vertical integral of Θ must be continuous there. Outside the edges of the cell, there is no overturning circulation, and $\Theta = \Theta_e$; hence

$$\int_{z_b(\phi_+)}^{h} \Theta(\phi_+, z) \, dz = \int_{z_b(\phi_+)}^{h} \Theta_e(\phi_+, z) \, dz, \tag{2.19}$$

with a similar expression evaluated at $\phi = \phi_-$. Additionally, since we assume no flow into or out of the cells, (2.15) integrated across each cell gives

$$\int_{\phi_1}^{\phi_+}\int_{z_b(\phi)}^{h} (\Theta - \Theta_e) \, dz \, \cos \phi \, d\phi = 0, \tag{2.20}$$

with a similar expression integrated between ϕ_- and ϕ_1. (2.20) is a statement of no net diabatic heating within the Hadley cells.

The Hadley cells are characterized by weak horizontal temperature gradients; neglecting advection along the bottom boundary, (2.15) says that $\Theta \simeq \Theta_e$ there,

so that (2.18) can be written

$$\frac{g}{\Theta_o}\int_{z_b}^{h}\Theta\ dz = \hat{\Phi} - \frac{\Omega^2 a^2}{2}\left(\cos^2\phi + \frac{\cos^4\phi_1}{\cos^2\phi}\right) - \frac{g}{\Theta_o}\int_{\phi_c}^{\phi}\Theta_e(\phi', z_b)\frac{dz_b}{d\phi'}\ d\phi'. \quad (2.21)$$

Substituting into (2.19) and (2.20) then prescribes the mathematical problem to be solved:

$$\hat{\Phi} - \frac{\Omega^2 a^2}{2}F(\phi_1, \phi_+) = X_e(\phi_+) \quad (2.22)$$

$$\hat{\Phi} - \frac{\Omega^2 a^2}{2}F(\phi_1, \phi_-) = X_e(\phi_-) \quad (2.23)$$

$$\int_{\phi_1}^{\phi_+}\left[\hat{\Phi} - \frac{\Omega^2 a^2}{2}F(\phi_1, \phi)\right]\cos\phi\ d\phi = \int_{\phi_1}^{\phi_+} X_e(\phi)\ \cos\phi\ d\phi \quad (2.24)$$

$$\int_{\phi_-}^{\phi_1}\left[\hat{\Phi} - \frac{\Omega^2 a^2}{2}F(\phi_1, \phi)\right]\cos\phi\ d\phi = \int_{\phi_-}^{\phi_1} X_e(\phi)\ \cos\phi\ d\phi \quad (2.25)$$

where we have used the shorthand

$$F(\phi_1, \phi) = \cos^2\phi + \frac{\cos^4\phi_1}{\cos^2\phi} \quad (2.26)$$

and defined the forcing function

$$X_e(\phi) = \frac{g}{\Theta_o}\int_{z_b(\phi)}^{h}\Theta_e(\phi, z)\ dz + \frac{g}{\Theta_o}\int_{\phi_c}^{\phi}\Theta_e(\phi', z_b)\frac{dz_b}{d\phi'}\ d\phi'. \quad (2.27)$$

Thus, (2.22)–(2.25) constitutes a set of equations in the four unknowns $\hat{\Phi}$, ϕ_1, ϕ_+, and ϕ_-. For a flat surface, X_e reduces to the form $\int_0^h \Theta_e\, dz$ as in Held and Hou [1980] and Lindzen and Hou [1988]. Variations in the height of the lower boundary impact the forcing function both explicitly, since both terms involve z_b, and implicitly through their influence on equilibrium temperature. The relative importance of these contributions will be discussed below.

The choice of h, taken to be the height of the tropopause on Earth, is not obvious for Mars. If the tropopause is defined as the level where the static stability changes drastically, no clear transition exists analogous to the terrestrial troposphere and stratosphere. The tropopause could also be defined as the level to which convection penetrates in radiative-convective equilibrium, but this definition excludes the pure radiative case. While work with MGCMs has shown that the Martian circulation extends to the mesopause, the mesopause hardly seems like a good definition since most of the mass transport in the Hadley cells is well below this level. Since in my simple MGCM (Section 2.3) 50% of the mass flux is typically located below 15 km, I adopt that value for h.

Since the theory is assumed to be axisymmetric, flat and zonal mean MOLA topography (Fig. 1-2) are considered. Θ_e in (2.27) is evaluated using either the

pure radiative equilibrium temperature given by (2.1) or the radiative-convective equilibrium temperature given by (2.3), recalling that the temperature must remain above the CO_2 frost temperature.

While the solutions to (2.22)–(2.25) depend solely on $X_e(\phi)$, it is only gradients of X_e that drive the circulation. (If X_e is constant, the trivial solution is a cell of zero width.) From (2.27),

$$\frac{dX_e}{d\phi} = \frac{g}{\Theta_0}\int_{z_b}^{h} \frac{\partial \Theta_e}{\partial \phi}\, dz \ , \tag{2.28}$$

from which we deduce the rather obvious conclusion that, as in the case of a flat surface, the circulation is driven by the vertically integrated temperature gradients. Topography enters both explicitly, in the integration limit, and implicitly, through its impact on Θ_e. Under the conditions of our calculations, both the surface temperature and the depth of the convecting layer, while varying substantially with latitude, are remarkably insensitive to the surface height variations. This insensitivity, a consequence of the weakness of the greenhouse effect, can be exploited to arrive at a simple understanding of the role of topographic height variations on the forcing of the Hadley circulation.

Now,

$$\int_{z_b}^{h} \frac{\partial \Theta_e}{\partial \phi}\, dz = \int_{h_c}^{h} \frac{\partial \Theta_e^R}{\partial \phi}\, dz + \int_{z_b}^{h_c} \frac{\partial \Theta_e^C}{\partial \phi}\, dz \ , \tag{2.29}$$

where $\Theta_e^C(\phi, z)$ and $\Theta_e^R(\phi, z)$ are the equilibrium temperatures within and above the convecting layer, respectively (and note that the latter is radiatively determined and independent of z_b), and $h_c(\phi)$ is the altitude of the top of the convecting layer. Within the convecting layer, and consistent with the Boussinesq approximation,

$$\Theta_e^C(\phi, z) = \Theta_e^S(\phi) - \Gamma_a\left[z - z_b(\phi)\right] \ ,$$

where $\Theta_e^S(\phi)$ is the surface temperature, and Γ_a is the adiabatic lapse rate; hence the gradient

$$\frac{\partial \Theta_e^C}{\partial \phi} = \frac{\partial \Theta_e^S}{\partial \phi} + \Gamma_a \frac{\partial z_b}{\partial \phi} \tag{2.30}$$

is independent of z. Therefore

$$\int_{z_b}^{h_c} \frac{\partial \Theta_e^C}{\partial \phi}\, dz = \epsilon\left(\frac{\partial \Theta_e^S}{\partial \phi} + \Gamma_a \frac{\partial z_b}{\partial \phi}\right) \ , \tag{2.31}$$

where $\epsilon = h_c - z_b$ is the depth of the convecting layer. As we have seen, both Θ_e^S and ϵ are, to an excellent approximation, independent of z_b, and so the surface topography enters (2.31) only through the term $\partial z_b/\partial\phi$.

Above the convecting layer, the contribution to (2.29) is

$$\int_{h_c}^{h} \frac{\partial \Theta_e^R}{\partial \phi}\, dz = \int_{\epsilon}^{h} \frac{\partial \Theta_e^R}{\partial \phi}\, dz + \int_{h_c}^{\epsilon} \frac{\partial \Theta_e^R}{\partial \phi}\, dz \ . \tag{2.32}$$

Accordingly, dependence of (2.32) on z_b is encapsulated in the second term. If the radiative lapse rate does not vary significantly with latitude, then $\partial\Theta_e^R/\partial\phi$ is independent of z (Fig. 2-1), so

$$\int_{h_c}^{\epsilon} \frac{\partial\Theta_e^R}{\partial\phi}\, dz \simeq \frac{\partial\Theta_e^R}{\partial\phi}(\phi,\epsilon)\,(\epsilon - h_c) = -\frac{\partial\Theta_e^R}{\partial\phi}(\phi,\epsilon)\; z_b\;.$$

In total, then, substituting into (2.28) and (2.29),

$$\frac{\Theta_0}{g}\frac{dX_e}{d\phi} \simeq \left[\epsilon\frac{\partial\Theta_e^S}{\partial\phi} + \int_{\epsilon}^{h} \frac{\partial\Theta_e^R}{\partial\phi}\, dz\right] + \Gamma_a\epsilon\frac{\partial z_b}{\partial\phi} - \frac{\partial\Theta_e^R}{\partial\phi}(\phi,\epsilon)\; z_b. \tag{2.33}$$

Of the two contributions that depend on z_b, the first depends directly on the local topographic slope, while the second does not. (But note that both contributions are zero with flat topography, since then $z_b = 0$.) For the most part, $\partial z_b/\partial\phi < 0$ for Mars, so the first term is generally negative, and hence tends to influence the forcing function in the same way as displacing the Θ_e maximum into the southern hemisphere. At equinox, the second term is small in the tropics and so the net effect of the topography is to shift the effective thermal equator into the southern hemisphere. This is illustrated in Fig. 2-8, for which the forcing function and its derivative have been calculated by direct substitution of the radiative-convective equilibrium temperature distribution, with the topography of Fig. 1-2, into (2.27). The impact of the topography is modest, but the analysis of Lindzen and Hou [1988] leads us to expect that a small asymmetry in the thermal forcing will produce a much larger asymmetry in the circulation. At the solstices, the possibly competing effect of the two terms makes simple statements on the basis of (2.33) more elusive. However, Fig. 2-8 shows that the net effect is weak at L_s=90°, with only a slight weakening of the gross latitudinal gradient. At L_s=270°, the impact of the surface topography is somewhat greater, with an intensification of the gross gradient.

Returning to (2.22)–(2.25), Figure 2-9 shows the solutions for ϕ_+, ϕ_1, and ϕ_- for each of the two topographies with pure radiative or radiative-convective forcing and physical constants appropriate for Mars. The solutions for flat topography for pure radiative and radiative-convective forcing are nearly equal, such that they lie on the same curve in Fig. 2-9. Hadley cells are most sensitive to the meridional gradient in equilibrium temperature, which is purely a consequence of the meridional gradient in solar heating in the absence of topography. Since the meridional gradient in solar heating is the same for both radiative forcings (c.f. (2.1) and (2.3)), their solutions are expected to be similar.

For flat topography at equinox, symmetric cells are obtained, which agrees with the limit of Held and Hou [1980]. When topography is added in the pure radiative case, ϕ_1 is shifted slightly upslope, while the poleward boundary of the winter cell (ϕ_+ for 270° < L_s < 360° and ϕ_- for 0° < L_s < 90°) shifts downslope. The deviations from the flat topography case may be attributed as the result of integrating over a different vertical range (z_b to h instead of 0 to h).

For the case of radiative-convective forcing and zonal mean MOLA topography,

ϕ_1 is shifted a significant distance upslope, which qualitatively agrees with previous MGCM results. Again the poleward boundary of the winter cell shifts downslope, but the boundary of the summer cell (ϕ_- for $270° < L_s < 360°$ and ϕ_+ for $0° < L_s < 90°$) shifts upslope. The large shift in the solution compared with the other cases is a result of the thermal effects of the slope on Θ_e. Differential convective heating aloft associated with the slope moves the latitude of maximum equilibrium temperature upslope and away from the subsolar latitude. This change in the location of the maximum equilibrium temperature causes the boundaries of the cells to move relative to the cases with zero topography or without convective forcing.

2.3 Experiments with a Simple MGCM

2.3.1 Description of the MIT MGCM

I have converted the MIT GCM to use physical constants appropriate for the Martian atmosphere, which is assumed to be entirely CO_2 and contain no dust. The dynamical core of the MIT GCM solves the fundamental equations of geophysical fluid dynamics in the hydrostatic approximation using the finite volume method on an Arakawa C grid [Marshall et al., 1997]. The default configuration has no viscosity nor vertical diffusion, and uses an eighth order Shapiro filter to remove grid scale noise. The horizontal configuration is a cube-sphere grid [Adcroft et al., 2004] with 32×32 points per cube face, equivalent to a resolution of 2.8° or 166 km at the equator. Note that the resolution of the MOLA dataset is 1/64° latitude × 1/32° longitude [Smith et al., 2001], which exceeds the horizontal resolution for the simple MGCM.

The vertical grid uses an η coordinate [Adcroft and Campin, 2004] with 30 levels, and the grid spacing increases approximately logarithmically with height. Zero elevation corresponds to a pressure of 6 hPa (the observed annual and global average value), which is also used as a reference pressure elsewhere in my calculations. The top level is centered at a pressure of 0.000117 hPa, which corresponds to a log pressure height of 119 km (using the reference pressure above and a scale height of 11 km). This is above the level where non-local thermodynamic equilibrium effects may become important [López-Valverde et al., 1998]. The top levels are not treated as realistically modeling the atmosphere in that region, since a sponge layer is also located in the upper levels (described below). Within each vertical level intersecting the surface, the resolution of the topography is increased by inserting sub grids spaced at 10% of the full vertical grid spacing at that level [Adcroft et al., 1997].

The external thermal forcing is specified by Newtonian relaxation to a prescribed equilibrium temperature following Held and Suarez [1994]. Explicitly, this term in the energy equation is

$$\frac{\partial T}{\partial t} = \cdots - k_T \left[T - T_{eq} \right], \tag{2.34}$$

where T is temperature, t is time, $k_T = 1/2$ sol^{-1} is the radiative relaxation rate, and T_{eq} is the equilibrium temperature, discussed in Section 2.1. The choice of k_T is based on a calculation using (6) of Showman et al. [2008] and is the same as the

value calculated by Haberle et al. [1997] for clear sky conditions. k_T is taken to be constant here for simplicity's sake, but in general varies with space (horizontally and vertically) and season. The assumption of fixed k_T implies that radiation and convection (if implicitly present in T_{eq}) operate on the same time scale.

Boundary layer friction is specified in the horizontal momentum equations by

$$\frac{\partial u}{\partial t} = \cdots - k_v(p)u \tag{2.35}$$

$$\frac{\partial v}{\partial t} = \cdots - k_v(p)v, \tag{2.36}$$

where k_v is the wind damping rate and is defined by

$$k_v = k_f \max\left(0, \frac{p - p_b}{p_o - p_b}\right), \tag{2.37}$$

where k_f is the wind damping rate of the lower atmosphere and $p_b = 0.7p_o$ is the top of the boundary layer. I set k_f=1 sol^{-1}, which is consistent with values in the literature (e.g. Lewis et al. [1996], Nayvelt et al. [1997]). Similar terms to the right side of (2.35) and (2.36) are also included in the horizontal momentum equations in the top three model levels as a sponge layer to avoid reflection off the model lid, with k_v set to 9, 3, and 1 sol^{-1} from uppermost to lowermost level, respectively.

2.3.2 Experiments

Each experiment was run at constant L_s for the following seasons: $L_s = 0°$, $L_s = 90°$, and $L_s = 270°$. Given the short radiative timescale of the Martian atmosphere (2 sols) and the lack of oceans with high heat capacity, the atmosphere is expected to respond quickly to changes in radiative forcing compared with the length of a season (one quarter of the Martian year or 167 sols). As such, it was unnecessary to integrate the model over several years to achieve a seasonal equilibrium. The model was run for a total of 180 sols or 6 Martian months, where a Martian month is defined to be 30 sols, and was fully spun up from an initial rest state with T_{eq}=200 K everywhere by the end of the second Martian month. A visual inspection of the zonally and monthly averaged results (i.e. potential temperature, horizontal and vertical velocities, and surface pressure) showed little variation from month to month after the initial spin up.

Figures 2-10 and 2-11 show the simple MGCM results for zonally averaged mass stream function time averaged for sols 60–180 when forced with the pure radiative equilibrium temperatures (Fig. 2-1) and radiative-convective equilibrium temperatures (Fig. 2-2), respectively. With pure radiative forcing, equinox conditions (L_s=0°), and flat topography (Fig. 2-10a), the cells are quite symmetric about the equator. When the north-south sloping component of topography is added (i.e full and mean topographies, Figs. 2-10d and 2-10g, respectively), the dividing streamline protrudes slightly into the southern hemisphere, but its maximum extent is not past −5°. A slight asymmetry between the strengths of the northern and southern cells

develops. For L_s=90° and pure radiative forcing (Figs. 2-10b, 2-10e, and 2-10h), no significant difference arises between the three topographies. The same occurs at L_s=270° (Figs. 2-10c, 2-10f, and 2-10i).

When convective forcing is allowed, a substantial difference arises at equinox between experiments without the north-south sloping component of topography (i.e. flat, Fig. 2-11a) and with it (i.e. full and mean, Figs. 2-11d and 2-11g, respectively). The flat topography produces symmetric cells, while the full and mean topography cases produce a stronger northern cell and shift the latitude of the dividing streamline to about −15° in the lower atmosphere [c.f. about −20° from Takahashi et al., 2003]. At L_s=90°, the cross-equatorial Hadley cell is stronger when the north-south sloping component is removed (compare Fig. 2-11b with Figs. 2-11e and 2-11h). At L_s=270°, the correlation with the presence of the north-south sloping component of topography is less apparent (c.f. Figs. 2-11c, 2-11f, and 2-11i).

2.3.3 Comparison of Hadley Cell Strengths

With pure radiative forcing, the strength of the Hadley cells at a given season varies little among the different topographies and does not appear to be correlated with the presence of the north-south slope. A very different scenario arises for radiative-convective forcing. Figure 2-12 shows the maximum magnitude of the zonally and time averaged stream function from each of the simple MGCM experiments with radiative-convective forcing. Specifically, the maximum magnitude within each thermally direct cell above the boundary layer is plotted for each topography (black symbols). The seasonal variation of Hadley cell strengths for full topography as predicted by the GFDL MGCM is also illustrated in Basu et al. [2006].

As seen in in Fig. 2-12, for flat topography, the strengths of the northern and southern cells are symmetric at equinox, and the strengths at the opposite solstices are equal. For mean topography, at equinox the northern cell is enhanced, while the southern cell is reduced. It is generally recognized from theory [e.g. Lindzen and Hou, 1988] and terrestrial observations [e.g. Peixoto and Oort, 1992, Fig. 7.19] that moving the latitude of maximum equilibrium temperature off the equator, such as what occurs due to changing seasons, produces a weak cell in the same hemisphere as the maximum and a strong cell that spans both hemispheres. The farther the maximum equilibrium temperature moves off equator, the more pronounced this effect becomes[2]. If the north-south slope is acting to shift the maximum equilibrium temperature upslope, as is indicated by Figs. 2-2g and 2-4a, then at equinox a stronger northern cell and weaker southern cell is expected for the mean topography case.

For flat topography at L_s=90°, the maximum equilibrium temperature is shifted far northward (Figs. 2-2b and 2-4b), producing no summer cell at all and a strong winter cell. For mean topography, the strength of the cell is reduced as compared with flat topography. For flat topography at L_s=270°, the latitude of maximum

[2]Compared with Earth, the difference between the equinoctial and solstitial circulations is much more dramatic, since the heat capacity of Martian soil is less than that of Earth's oceans [Haberle et al., 1993]. Without the mediating influence of the ocean, the latitude of maximum equilibrium temperature can move well off the equator.

equilibrium temperature is shifted far southward, producing a strong "winter" cell in the opposite sense as at L_s=90°. However, the addition of zonal mean topography at L_s=270° does not change the strength of the cell as significantly as at L_s=90°.

To further illustrate this seasonal asymmetry, several more experiments were performed with radiative-convective forcing at L_s=90° and L_s=270°, which had the following idealized zonal mean topography:

$$z_{bi} = -2\tanh\left(\frac{\phi - 2^\circ}{m}\right), \tag{2.38}$$

where z_{bi} is the height of the idealized topography in km, ϕ is in degrees, and m controls the steepness of the slope (lower values correspond to steeper slope). Figure 2-13 shows the simple MGCM results for L_s=90° for flat topography and the following three values of m: 40, 20, and 10. As slope steepness increases, the strength of the Hadley cell decreases. Figure 2-14 shows results for L_s=270° with the same topographies. In this case, the steepness of the slope has little effect on the cell strength.

Evidently, a circulation that flows downslope near the surface causes the Hadley cells to lose strength, but that strength is not regained for an upslope flow. This phenomenon further comes into play in comparing full topography and mean topography. In Fig. 2-12, the strengths for full topography are always less than the strengths for mean topography at the corresponding season. As the circulation flows up and down the mountains and valleys, strength is lost as the air flows downward along the topography, but not regained when it flows upward. This diminishing is observed when comparing flat and "wave" (i.e. full topography minus zonal mean, not shown) topographies. For full topography, this mountain effect is superimposed onto the the effect (if any) of the mean sloping component. The effect is associated with the radiative-convective forcing, as runs with pure radiative forcing show little difference in Hadley cell intensity for any topography.

2.3.4 Comparison with the GFDL MGCM

To demonstrate that my simple radiation scheme captures the effect of topography on the Martian Hadley cell, the simple MGCM results are compared to the GFDL MGCM, which uses a full (non-gray) radiation scheme. The GFDL MGCM was originally based on the GFDL SKYHI terrestrial GCM and an early version of the model has been described in Wilson and Hamilton [1996]. Subsequent descriptions appear in Richardson and Wilson [2002] and Hinson and Wilson [2004]. This model has been used to examine tides and planetary waves [Wilson and Hamilton, 1996; Hinson and Wilson, 2002; Wilson et al., 2002; Hinson et al., 2003], the water cycle [Richardson and Wilson, 2002; Richardson et al., 2002], the dust cycle [Basu et al., 2004; Basu et al., 2006], and cloud radiative effects [Hinson and Wilson, 2004; Wilson et al., 2007, 2008]. More recently the physical parameterizations have been adapted to the GFDL Flexible Modeling System (FMS) which includes a choice of dynamical cores (finite difference, finite volume and spectral) and associated infrastructure. The Mars

physics has been tested with all 3 dynamical cores and the finite volume (FV) model was selected.

The model uses the radiation code developed and used by the NASA Ames Mars modeling group [Kahre et al., 2006; Kahre et al., 2008]. This code is based on a two-stream solution to the radiative transfer equation with CO_2 and water vapor opacities calculated using correlated-k values in 12 spectral bands ranging from 0.3 to 250 microns. The two-stream solution is generalized for solar and infrared radiation, with scattering based on the δ-Eddington approximation at visible wavelengths and the hemispheric mean approximation at infrared wavelengths [Toon et al., 1989]. The model has been validated with other MGCMs and the available data, and I consider it to be a robust representation of the Martian atmosphere.

Simulations using the GFDL MGCM were carried out with 5° latitude by 6° longitude horizontal resolution and 46 levels. Simulations were run for 50 sols. The CO_2 condensation cycle was not included; therefore the atmospheric mass remained constant with a global mean surface pressure of 6 hPa. Orbital eccentricity was set to zero to eliminate differences in the solar constant between the two solstice seasons, thus highlighting the asymmetric influence of the topography. Surface albedo and surface thermal inertia were held constant at 0.15 and 350 J m^{-2} $s^{-1/2}$ K^{-1}, respectively. Column dust opacity was set to a globally uniform value of 0.3, a low-dust setting. The topographies considered were flat and idealized zonal mean topography (given by (2.38)) with $m = 20$.

Figure 2-15 shows the results from the GFDL MGCM with flat topography (top row) and idealized zonal mean topography (bottom row) for L_s=90° (left column) and L_s=270° (right column). The results shown are a 10 sol average centered on the solstices. At L_s=90°, the addition of zonal mean topography suppresses the maximum strength of the Hadley cell to 55% of its maximum strength with flat topography, while at L_s=270° the addition of zonal mean topography strengthens the cell to only 109% of its maximum strength with flat topography. The qualitative agreement with Figs. 2-13 and 2-14 indicates that the simplifications to the simple radiation scheme (Section 2.1) are not centrally important. Additionally, experiments (not shown) with the GFDL MGCM were performed with the same idealized topography used in Figs. 2-13 and 2-14. These experiments again showed that the Hadley cell strength at L_s=90° is sensitive to the steepness of the topographic slope, but shows little response to the slope at L_s=270°.

Quantitative differences in Hadley cell strengths between the simple MGCM and the GFDL MGCM are due to fundamental differences in the radiation schemes. The Hadley cell strengths in the simple MGCM are sensitive to the values used for τ_{oo} and k_t. The simple radiation code also fails to produce a difference in the Hadley cell strengths at the opposite solstices for flat topography. The meridional gradient on equilibrium temperature depends on the solar constant by a power of 1/4, implying that the change in the gradient (directly related to the strength of the cells) will be slight between the opposite solstices using the gray radiation scheme, as observed. However, k_t also has a dependence on the solar constant (and is variable in time and space) that has been ignored in the simple MGCM experiments here, but does have an effect on the Hadley cell strength. For example, doubling the mean solar constant

in the specification of equilibrium temperature while keeping k_t at its default value has almost no effect on the Hadley cell strength at L_s=270°. However, changing k_T to a value of 1 sol^{-1}, consistent with the doubled mean solar constant, produces a change in strength by about a factor of 3.

The boundaries of the cells are in quantitative agreement between the simple and GFDL MGCMs and are less sensitive to the particular aspects of my radiation scheme. This fact, along with qualitative agreement in the behavior of Hadley cell strengths between the two models, lends sufficient credibility to my simple radiation scheme.

2.3.5 Comparison with Previous Simulations

As wind data for the Martian atmosphere above the boundary layer is extremely sparse compared with terrestrial data, we are left to compare the simple MGCM stream function results with previous models. The results for stream function strength from the MGCM of Takahashi et al. [2003] are also plotted in Fig. 2-12 (gray symbols). Comparison of mean and full topographies at equinox shows that that the northern cell is stronger for the mean topography case, in agreement with my results. Quantitatively, my simple MGCM predicts a weaker cell for full topography at L_s=270°, a stronger cell for full topography at L_s=90°, and a weaker northern cell for full and mean topographies at equinox. Quantitative disagreement between the two models arises from differences in the radiation schemes between my model and that of Takahashi et al. [2003]. Note that Basu et al. [2006] showed using the GFDL MGCM that the ratio of Hadley cell strengths at the solstices depends on the dust loading in the atmosphere.

Joshi et al. [1995] stated that the Hadley cell at L_s=270° was a factor of 1.5 stronger than at L_s=90° in their "intermediate" global circulation model (based on the Oxford MGCM), which most closely corresponds to my radiative-convective forcing and full topography. My simple MGCM also yielded a factor of $\approx$ 1.5 for this setup, while Takahashi et al. [2003] obtained a factor of $\approx$ 3. Joshi et al. [1995] also noted that the effect was still observed even when solar insolation was kept constant for both seasons. However, they speculated that an enhanced circulation at L_s=270° was because the rising branch is located in an area of lower pressure (i.e. higher elevation) and did not attribute the difference to the thermal affects of the slope.

2.4 Comparison of MGCM and Modified Lindzen and Hou [1988] Model

Figure 2-16 shows the solution to the modified Lindzen and Hou [1988] model replotted so that ϕ_+, ϕ_1, and ϕ_- for each topography and radiative forcing are displayed together. It is now apparent that as L_s approaches 90° and 270°, ϕ_1 approaches the boundary of the summer cell in the summer hemisphere. The physical implication is that the summer cell disappears, which is what is observed in the simple MGCM results (Figs. 2-10 and 2-11). Also plotted in Fig. 2-16 are the values for ϕ_+, ϕ_1, and

ϕ_- determined from the MGCM results for the appropriate topographies, seasons, and radiative forcings, including some runs at seasons not discussed in Section 2.3.

The boundaries of the Hadley cells in the simple MGCM results are computed as follows. For each thermally direct cell (one near solstice, two near equinox), the maximum magnitude of the zonally averaged mass stream function (above the boundary layer) is found. Then, at the same pressure level as each maximum, the latitude where the stream function falls to within 1% of its maximum value is located. The northernmost 1% latitude is ϕ_+ and the southernmost is ϕ_-. When there is one thermally direct cell, ϕ_1 is equal to whichever of ϕ_+ or ϕ_- is in the summer hemisphere. When there are two thermally direct cells, the average of the two innermost 1% latitudes is taken to be ϕ_1. Interpreting the boundaries of the cells from the simple MGCM results can be difficult because in some cases the latitude of the boundary varies with height, e.g. at the boundary in the winter hemisphere at solstice. Also, particularly near equinox on the poleward sides of the cells, multiple 1% latitudes may exist when closed areas of circulation in the opposite direction appear within the thermally direct cell. In this case the innermost 1% latitude is used. Near the solstice, the stream function in the summer hemisphere decreases very gradually, which causes the value derived for the boundary to vary slightly depending on the cutoff percentage used (e.g. 1% vs. 0.1%).

From Fig. 2-16, the agreement of ϕ_1 between the simple MGCM results and the modified Lindzen and Hou [1988] model is generally good. The solutions for the poleward boundary of the summer cell agree for pure radiative forcing, but the simple MGCM results are offset in the equatorward direction for radiative-convective forcing. The solutions for the poleward boundary of the winter cell do not agree. The simple MGCM results are offset equatorward, and they do not follow the same shape as the modified Lindzen and Hou [1988] model solution. One possible explanation is that in the simple MGCM results the latitudinal boundary of the winter cell varies with height, and in fact does extend further poleward at higher altitudes. Another explanation is that the simple MGCM contains eddies, while the Lindzen and Hou [1988] model does not, on account of its axisymmetric nature.

Since the modified Lindzen and Hou [1988] model is axisymmetric, it is perhaps more sensible to compare it to an axisymmetric MGCM. I ran the simple MGCM in axisymmetric mode, where the cube-sphere geometry was replaced by grid points evenly spaced at 2.8° degrees of latitude along a single strip of longitude of width 2.8°. When vertical diffusion of momentum was not included, inertial instabilities developed in the tropics that made it impossible to determine ϕ_1 near equinox. Adding a constant diffusion of 0.0005 $\mathrm{Pa}^2\ \mathrm{s}^{-1}$ everywhere resolved ϕ_1, but induced a Ferrel cell.

Figure 2-17 shows a plot of the modified Lindzen and Hou [1988] model solutions as in Fig. 2-16 but with the axisymmetric simple MGCM results instead of the full 3D simple MGCM. The discrepancy in the poleward boundary of the winter cell remains, possibly due to the Ferrel cell created by adding diffusion. In runs without diffusion, the poleward boundary of the winter cell extends nearly to the winter pole, in agreement with the modified Lindzen and Hou [1988] results.

To further assess the role of eddies and the mean circulation in the 3D simple

MGCM simulations, I decomposed the momentum budget as follows. Ignoring the effects of the boundary layer (i.e. mountain torque and friction) on the momentum budget, the total derivative of the absolute angular momentum given by (2.12) may be set equal to zero,

$$\frac{\partial M_a}{\partial t} + \frac{u}{a\cos\phi}\frac{\partial M_a}{\partial \lambda} + \frac{v}{a}\frac{\partial M_a}{\partial \phi} + \omega\frac{\partial M_a}{\partial p} - fa\cos\phi v = 0, \tag{2.39}$$

where λ is longitude, ω is the vertical velocity in pressure coordinates, and $M_a = a\cos\phi u$ is the relative angular momentum. Averaging zonally and in time and making use of the continuity equation,

$$\frac{1}{a\cos\phi}\frac{\partial}{\partial\phi}\left(\cos\phi\left[\overline{vM_a}\right]\right) + \frac{\partial}{\partial p}\left(\left[\overline{\omega M_a}\right]\right) = fa\cos\phi\left[\overline{v}\right], \tag{2.40}$$

where the bracket notation indicates a zonal average and the over bar indicates a time average. The term $\left[\overline{vM_a}\right]$ may be further written as

$$\left[\overline{vM_a}\right] = a\cos\phi\left(\left[\overline{u}\right]\left[\overline{v}\right] + \overline{\left[u\right]'\left[v\right]'} + \left[\overline{u^*v^*}\right]\right) \tag{2.41}$$

where primes indicate a departure from the time average, and asterisks indicate a departure from the zonal average. The first term on the right hand side of (2.41) is the meridional transport of angular momentum by the steady mean circulation, the second is the transport by the transient circulation, and the third is the transport by spatial eddies. The second term was found to be much smaller than the other two; thus it was neglected. Similarly, (2.41) may be written for the vertical transport of angular momentum, where v is replaced by ω. Substituting (2.41) and the equivalent expression for ω into (2.40) (after noting that the vertical transport by the transient and spatial eddies is small) leaves

$$\frac{1}{a\cos\phi}\frac{\partial}{\partial\phi}\left(a\cos^2\phi\overline{[u^*v^*]}\right) + \frac{1}{a\cos\phi}\frac{\partial}{\partial\phi}\left(a\cos^2\phi\left[\overline{u}\right]\left[\overline{v}\right]\right) + \frac{\partial}{\partial p}\left(a\cos\phi\left[\overline{u}\right]\left[\overline{\omega}\right]\right) = fa\cos\phi\left[\overline{v}\right], \tag{2.42}$$

where the term on the right hand side is the planetary term.

Figure 2-18 shows the three terms on the left hand side of (2.42) calculated from the simple MGCM results with radiative-convective forcing and full topography at L_s=0, 90, and 270°. Within the Hadley cells, the planetary term is balanced by the meridional transport by the steady mean circulation during the solstices. At equinox, all three terms are small within the Hadley cells. Outside the Hadley cells, the meridional transport by spatial eddies nearly balances the planetary term. The presence of eddies near the poleward boundary of the Hadley cell, and the fact that the axisymmetric simple MGCM runs without diffusion (i.e. no spatial eddies) show better agreement with the Lindzen and Hou [1988] model, suggests that by driving the extratropical Ferrell cell, eddies may be important in determining the poleward boundaries of the Hadley cells at equinox and in the winter hemisphere at the solstices.

Walker and Schneider [2006] showed in idealized GCM simulations that the strength

of the Hadley cell is related to the eddy momentum flux divergence. In Fig. 2-18, the spatial eddy term is greater in the northern (winter) hemisphere at L_s=270° than in the southern (winter) hemisphere at L_s=90°. This effect is also seen in my simple MGCM simulations with flat topography. Eddies may also be important in addition to the topography in determining the seasonal asymmetry in Hadley cell strength, but this has not been tested.

2.5 Discussion and Conclusions

I have continued the investigation of the effect of a latitudinally varying slope on the Martian Hadley cells initiated in detail by Richardson and Wilson [2002] and Takahashi et al. [2003]. The problem was approached by revising the Hadley cell model of Lindzen and Hou [1988] to include topography, which allowed us to solve for the latitudinal boundaries of the cells. This theory was compared with the results from a simple MGCM. Both models were thermally forced using Newtonian relaxation to one of two equilibrium temperature states: one that included the effects of convection and one that did not. In the case of the latter, almost no dependence on the topography was observed in either model. When convective forcing was allowed, both models predicted that the latitude of the dividing streamline is shifted upslope at equinox. The effect of the slope on the radiative-convective equilibrium temperature aloft was found to dominate over the geometrical effects of the slope.

From the simple MGCM results, an analysis of the strengths of the Hadley cells was carried out. At equinox with radiative-convective forcing, the presence of the slope strengthens the southern cell and weakens the northern cell as the latitude of maximum equilibrium temperature moves upslope. At L_s=90° with radiative-convective forcing, the cross-equatorial cell is weakened with sloping topography, while at L_s=270°, the strength of the cell is independent of slope. Further experiments with idealized zonal mean topography showed that as the steepness of the slope is increased, the strength of the cell decreases at L_s=90°.

A discrepancy arose between my simple MGCM results and the modified Lindzen and Hou [1988] model results regarding the latitude of the poleward boundary of the Hadley cell in the winter hemisphere around the solstice seasons. This difference could be caused by eddies, since the simple 3D MGCM allows for their presence but the Lindzen and Hou [1988] model does not. Axisymmetric simple MGCM runs without diffusion and hence without eddies produced better agreement with the modified Lindzen and Hou [1988] model. A breakdown of the momentum budget showed that the spatial eddies are relatively weak within the Hadley cells at the solstices, but that eddies are relatively strong outside the Hadley cells. Eddies are stronger during northern winter (L_s=270°) than southern winter (L_s=90°). Eddies may play a role in determining the strengths and poleward boundaries of the Hadley cell, as also suggested by Walker and Schneider [2006] in idealized terrestrial GCM runs.

Molnar and Emanuel [1999] considered the radiative-convective equilibrium case when absorbers, namely water vapor, are present within the atmosphere. In the limit in which the atmosphere is opaque to solar radiation, the temperature at any level

aloft becomes independent of the height of the surface. The Molnar and Emanuel [1999] study may be applicable to periods when the Martian atmosphere is experiencing very dusty conditions [Viking Lander 1 measured optical depths in excess of 4 during a dust storm, Colburn et al., 1989], since atmospheric dust is a strong absorber. Basu et al. [2006] showed with the GFDL MGCM that as dust optical depth increases, the ratio of the stream function maximum at L_s=270° to L_s=90° decreases, which implies that dust inhibits the effect of the slope. However, dust also decreases the radiative relaxation time. It would be interesting to use the modified Lindzen and Hou [1988] model to study the effects of increased dust on the Hadley cell boundaries, provided that the appropriate changes could be made to my radiation scheme.

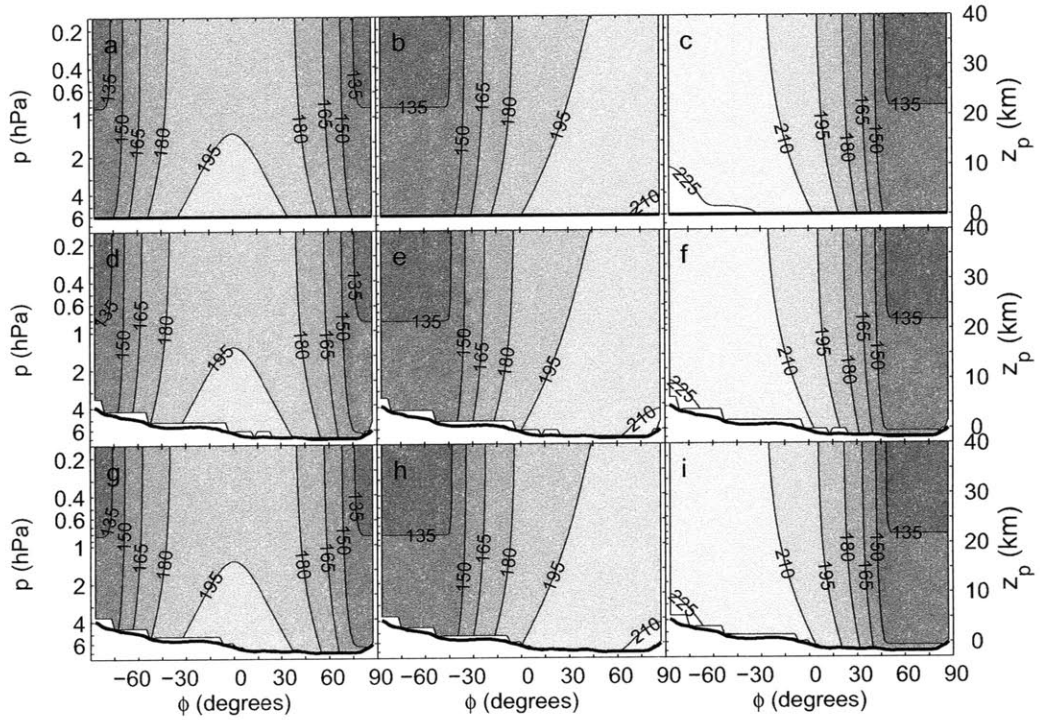

Figure 2-1: Zonally averaged pure radiative equilibrium temperature (units in K). Latitude is plotted on the x-axis, pressure is plotted on the left y-axis, and log pressure height is plotted on the right y-axis, assuming a scale height of 11 km and a reference pressure of 6 hPa. Only temperatures below ~0.2 hPa (40 km log pressure height) are shown. From left to right, the columns are L_s=0, 90, and 270°, respectively. From top to bottom, the rows are flat, full, and mean topography. Contour interval is 15 K.

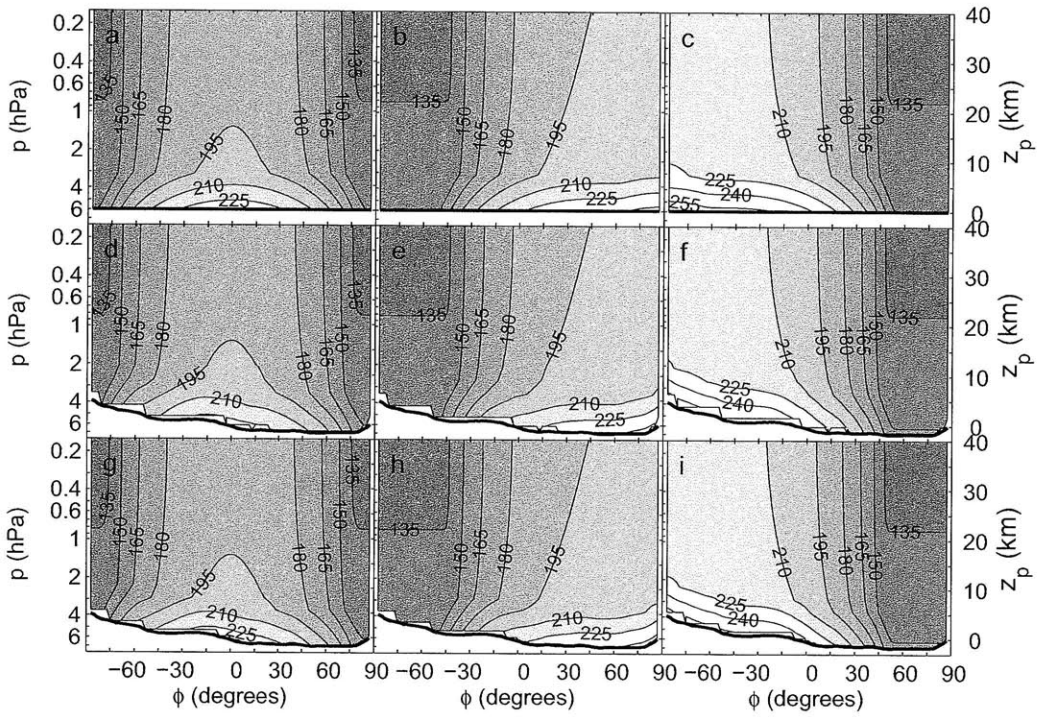

Figure 2-2: Zonally averaged radiative-convective equilibrium temperature (units in K). Latitude is plotted on the x-axis, pressure is plotted on the left y-axis, and log pressure height is plotted on the right y-axis, assuming a scale height of 11 km and a reference pressure of 6 hPa. Only temperatures below ~0.2 hPa (40 km log pressure height) are shown. From left to right, the columns are L_s=0, 90, and 270°. From top to bottom, the rows are flat, full, and mean topography. Contour interval is 15 K.

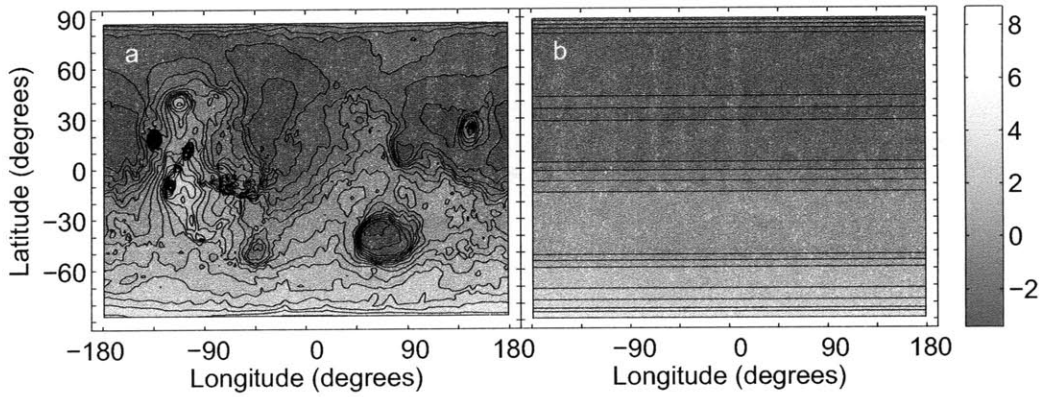

Figure 2-3: The topography of Mars. Panel (a) is the full topography measured by MOLA ("full") and (b) is the zonal mean MOLA topography ("mean"). Elevations are in km; contour interval is 0.5 km.

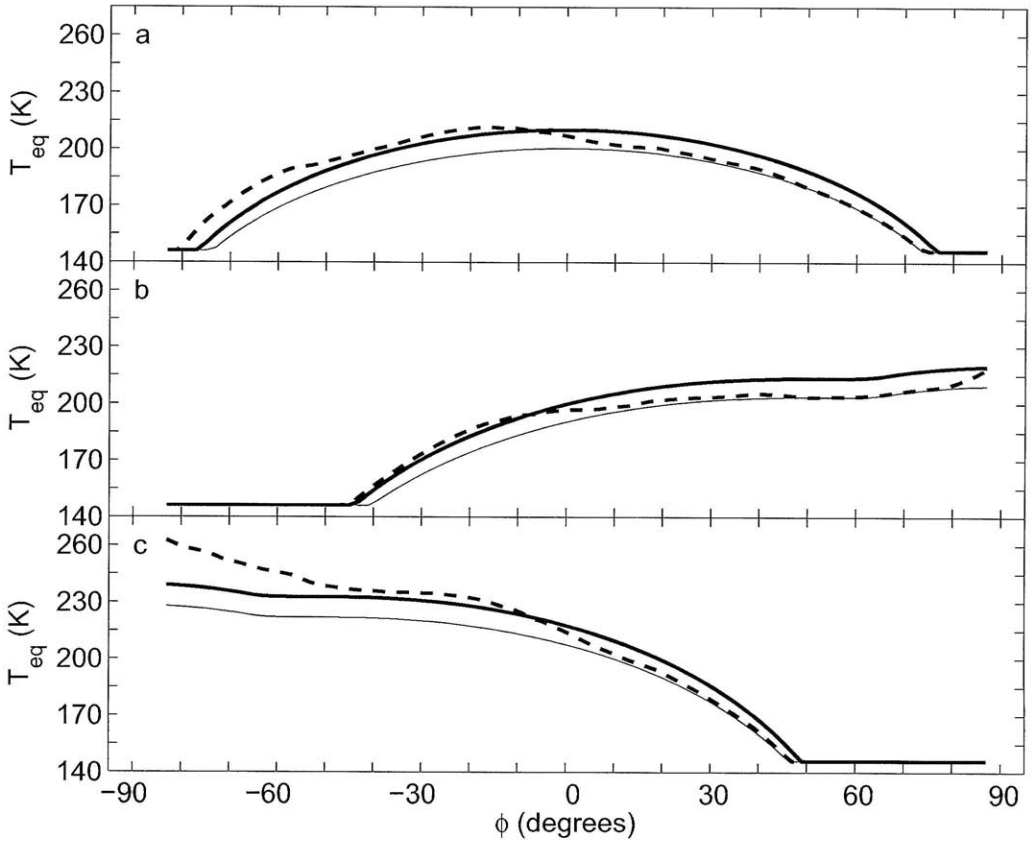

Figure 2-4: Equilibrium temperature at a constant pressure of 3.8 hPa (5 km log pressure height). Panel (a) is for L_s=0°, (b) is L_s=90°, and (c) is L_s=270°. The thin solid line is $T_{eq,R}$ (independent of topography), the heavy solid line is $T_{eq,RC}$ with flat topography, and the dashed solid line is $T_{eq,RC}$ with mean topography.

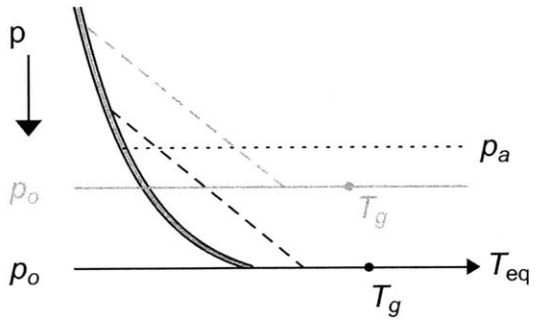

Figure 2-5: Schematic of equilibrium temperatures for two different surface elevations (black and gray horizontal lines). The pure radiative equilibrium temperature (black and gray curve) is the same at a given level aloft (p_a) for any surface height. The surface temperature in pure radiative equilibrium (T_g) is lower for the elevated surface due to the reduced greenhouse effect, but this effect is negligible in the optically thin Martian atmosphere. The dashed lines are adiabats drawn in radiative-convective equilibrium. For this case, the equilibrium temperature at some level p_a is warmer above the elevated surface.

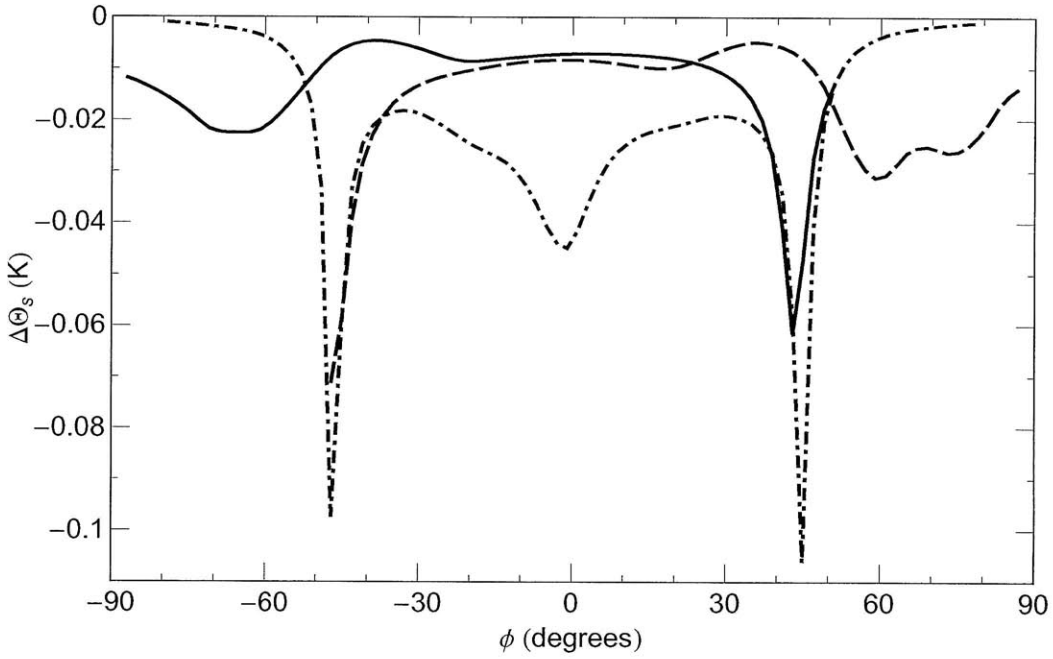

Figure 2-6: Plot of $\Delta\Theta_s$ vs. latitude. The dash-dot line is for L_s=0°, the dashed is L_s=90°, and the solid is L_s=270°. The curves are not plotted in the regions where the temperature falls below the CO_2 frost temperature. Several sharp minima occur at latitudes that correspond to the sinking branches of the Hadley cell, while broader minima correspond to the rising branches.

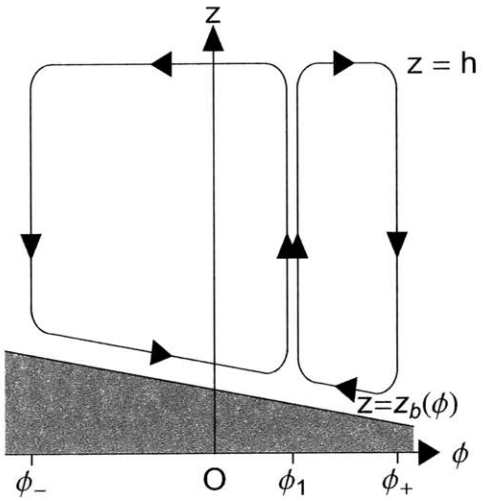

Figure 2-7: Parameters in the model of Lindzen and Hou [1988] with a bottom topography $z_b(\phi)$ added. The x-axis is latitude; the y-axis is height. Arrows indicate the direction of flow.

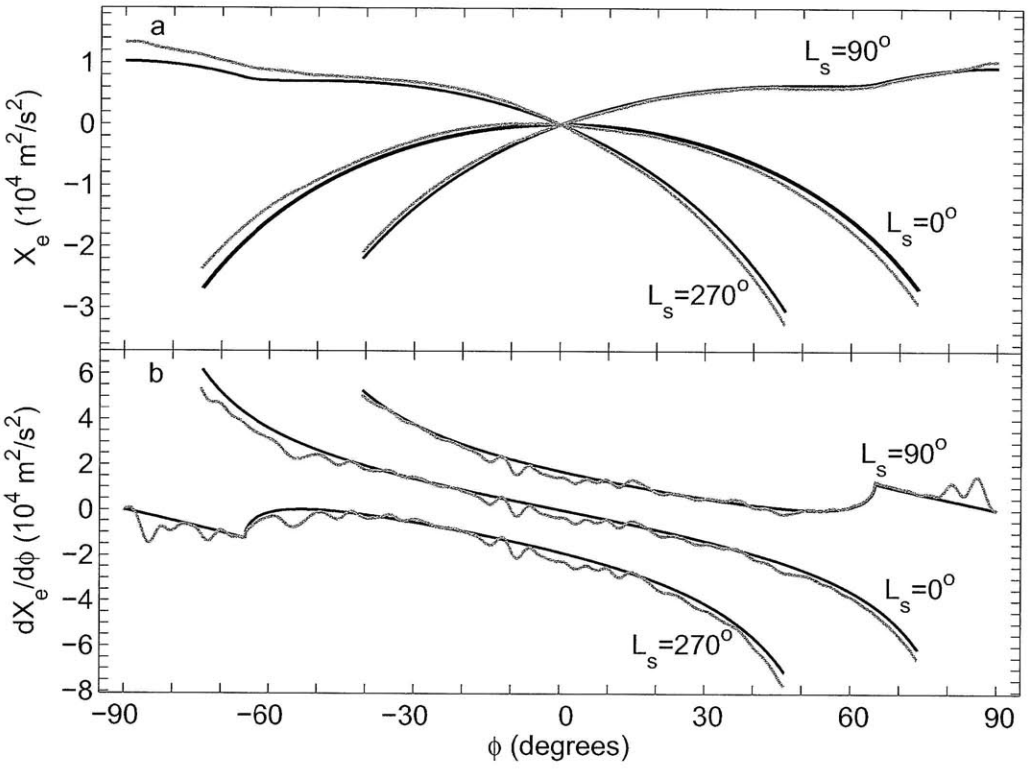

Figure 2-8: (a) Forcing function given by (2.27) for L_s=0, 90, and 270°. The black curve is flat topography and the gray curve is zonal mean topography. Each curve has been normalized such that its value at the equator is subtracted from each point in the curve. Regions where the temperature is equal to the CO_2 condensation temperature are not plotted. (b) Latitudinal derivative of the forcing function given in panel (a). The noise in the curves with topography is a result of the fact that the derivative of the measured topography is noisy. The net effect of topography is to reduce the latitudinal derivative of the forcing function.

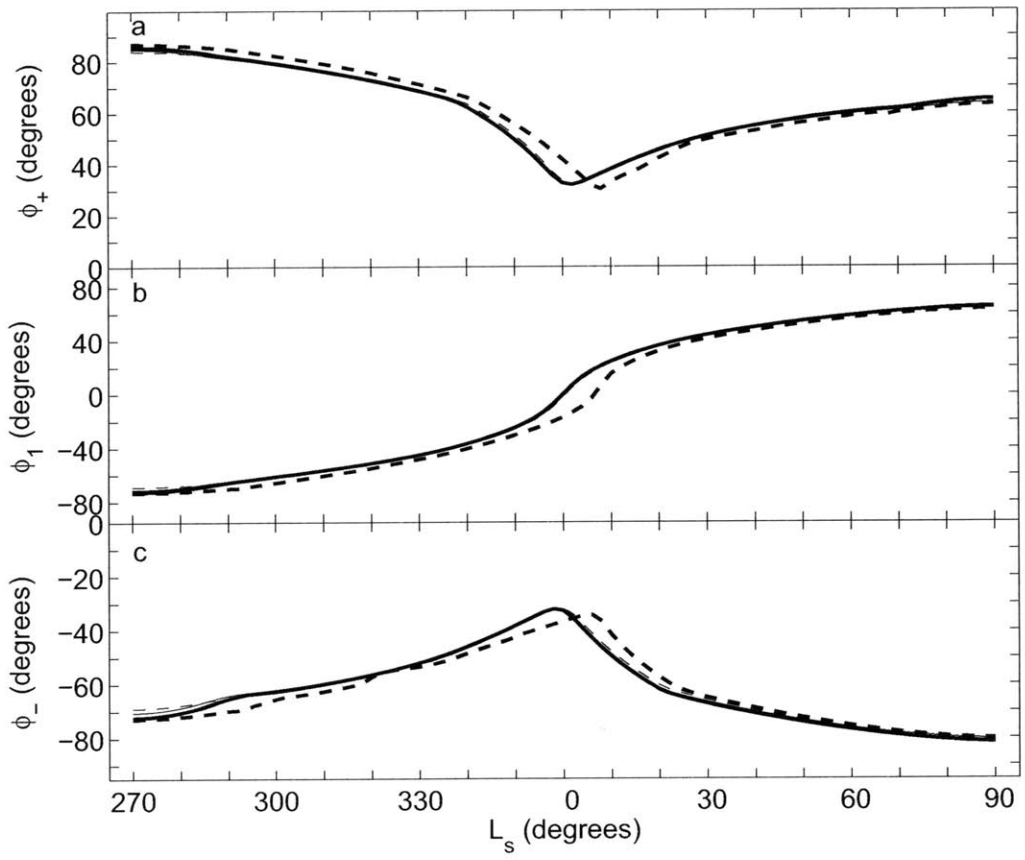

Figure 2-9: Solutions to (2.22)–(2.25). Panel (a) is the solution for ϕ_+, (b) for ϕ_1, and (c) for ϕ_-. The heavy solid line is the solution for flat topography for both pure radiative and radiative-convective forcing, which differ by less than 2%. The thin dashed line (barely visible as it is almost indistinguishable from the heavy solid line) is the solution for zonal mean MOLA topography with pure radiative forcing, and the heavy dashed line is the same but for radiative-convective forcing.

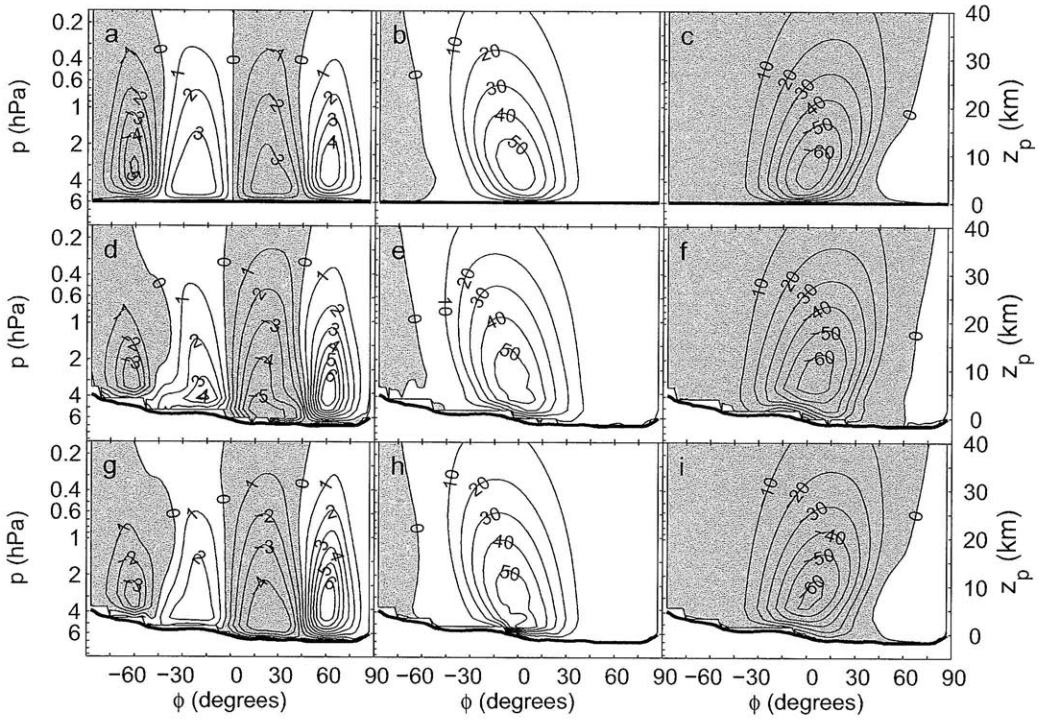

Figure 2-10: Simple MGCM results for zonally and time averaged mass stream function with pure radiative forcing. Units are 10^8 kg s^{-1}. Positive flow is counterclockwise; negative contours are shaded. Latitude is plotted on the x-axis, pressure is plotted on the left y-axis, and log pressure height is plotted on the right y-axis, assuming a scale height of 11 km and a reference pressure of 6 hPa. Only results below ~0.2 hPa (40 km log pressure height) are shown. From left to right, the columns are L_s=0, 90, and 270°. From top to bottom, the rows are flat, full, and mean topography. Note the different contour intervals (1×10^8 kg s^{-1} for L_s=0°and 10×10^8 kg s^{-1} for L_s=90° and L_s=270°).

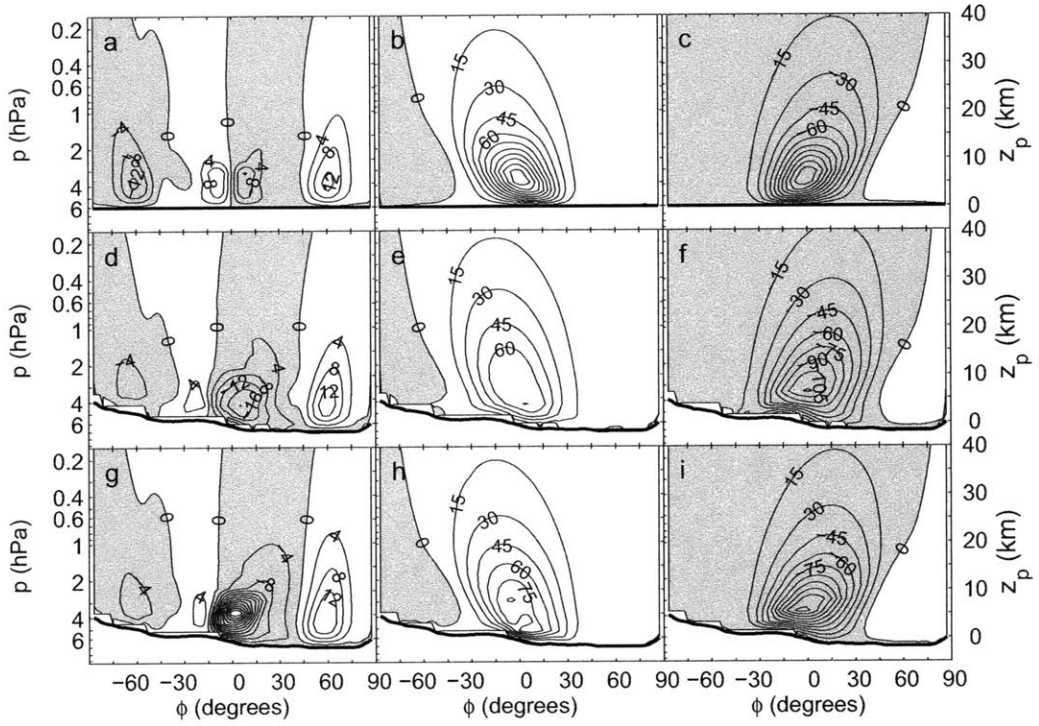

Figure 2-11: Simple MGCM results for zonally and time averaged mass stream function with radiative-convective forcing. Units are 10^8 kg s^{-1}. Positive flow is counterclockwise; negative contours are shaded. Latitude is plotted on the x-axis, pressure is plotted on the left y-axis, and log pressure height is plotted on the right y-axis, assuming a scale height of 11 km and a reference pressure of 6 hPa. Only results below $\sim$0.2 hPa (40 km log pressure height) are shown. From left to right, the columns are L_s=0, 90, and 270°. From top to bottom, the rows are flat, full, and mean topography. Note the different contour intervals (4×10^8 kg s^{-1} for L_s=0°and 15×10^8 kg s^{-1} for L_s=90° and L_s=270°).

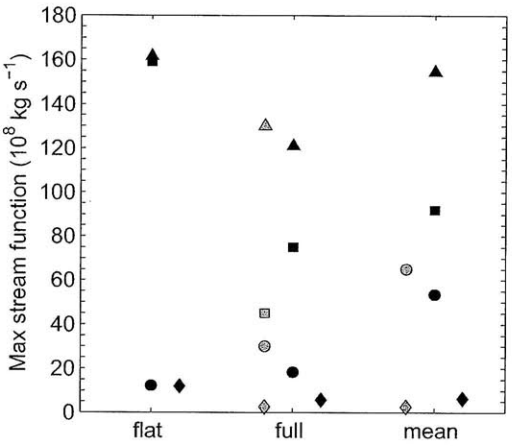

Figure 2-12: Maximum magnitude (above the boundary layer) of the zonally and time averaged mass stream function from the simple MGCM results with radiative-convective forcing (black symbols). The gray symbols are from Takahashi et al. [2003]. The results are grouped by the various topographies. The squares are for L_s=90°, the triangles are for L_s=270°, the circles are for the northern cell at L_s=0°, and the diamonds are for the southern cell at L_s=0°.

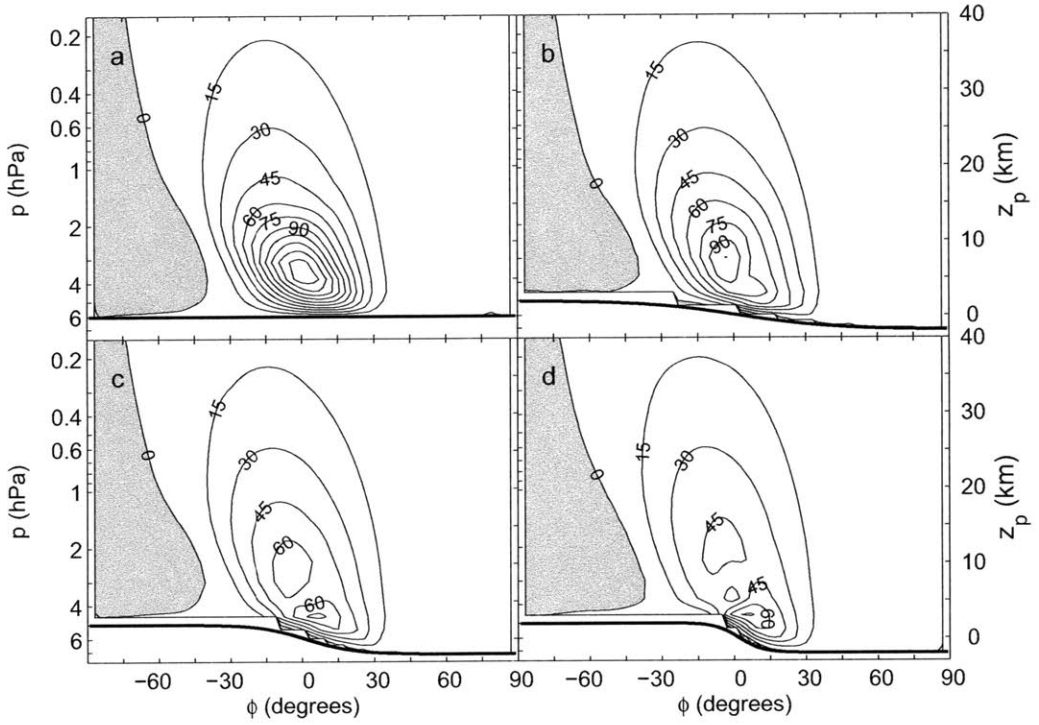

Figure 2-13: Zonally averaged mass stream function simple MGCM results for L_s=90°, radiative-convective forcing, and idealized zonal mean topography. Units are 10^8 kg s^{-1}. Positive flow is counterclockwise; negative contours are shaded. Contour interval is 15×10^8 kg s^{-1}. Latitude is plotted on the x-axis, pressure is plotted on the left y-axis, and log pressure height is plotted on the right y-axis, assuming a scale height of 11 km and a reference pressure of 6 hPa. Only results below ~0.2 hPa (40 km log pressure height) are shown. Panel (a) is for flat topography (same as Fig. 2-11b), and panels (b)–(d) are for idealized zonal mean topography of increasing steepness (m equal to 40, 20, and 10, respectively). The maximum magnitudes for panels (a), (b), (c), and (d) are 161, 106, 80, and 77 $\times 10^8$ kg s^{-1} respectively; thus, stream function strength decreases as the topographic slope's steepness increases.

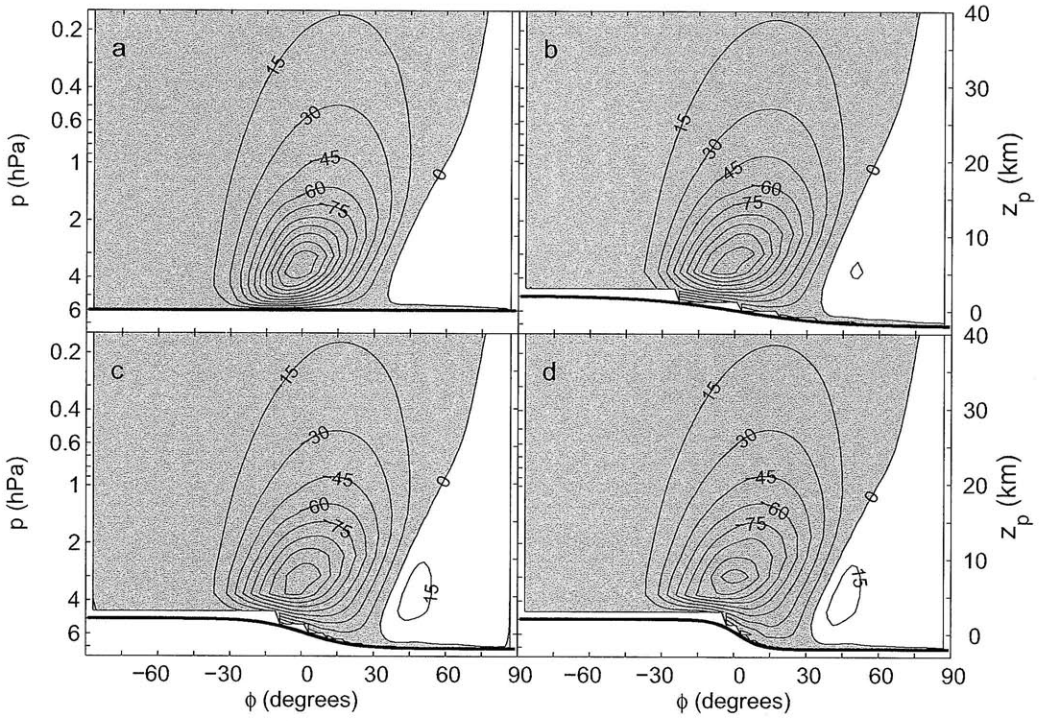

Figure 2-14: Zonally averaged mass stream function simple MGCM results for L_s=270°, radiative-convective forcing, and idealized zonal mean topography. Units are 10^8 kg s^{-1}. Positive flow is counterclockwise; negative contours are shaded. Contour interval is 15×10^8 kg s^{-1}. Latitude is plotted on the x-axis, pressure is plotted on the left y-axis, and log pressure height is plotted on the right y-axis, assuming a scale height of 11 km and a reference pressure of 6 hPa. Only results below ~0.2 hPa (40 km log pressure height) are shown. Panel (a) is for flat topography (same as Fig. 2-11c), and panels (b)–(d) are for idealized zonal mean topography of increasing steepness (m equal to 40, 20, and 10, respectively). The maximum magnitudes for panels (a), (b), (c), and (d) are 163, 144, 140, and 140 $\times 10^8$ kg s^{-1} respectively; thus, stream function strength is independent of the topographic slope's steepness, contrary to at L_s=270° (Fig. 2-13).

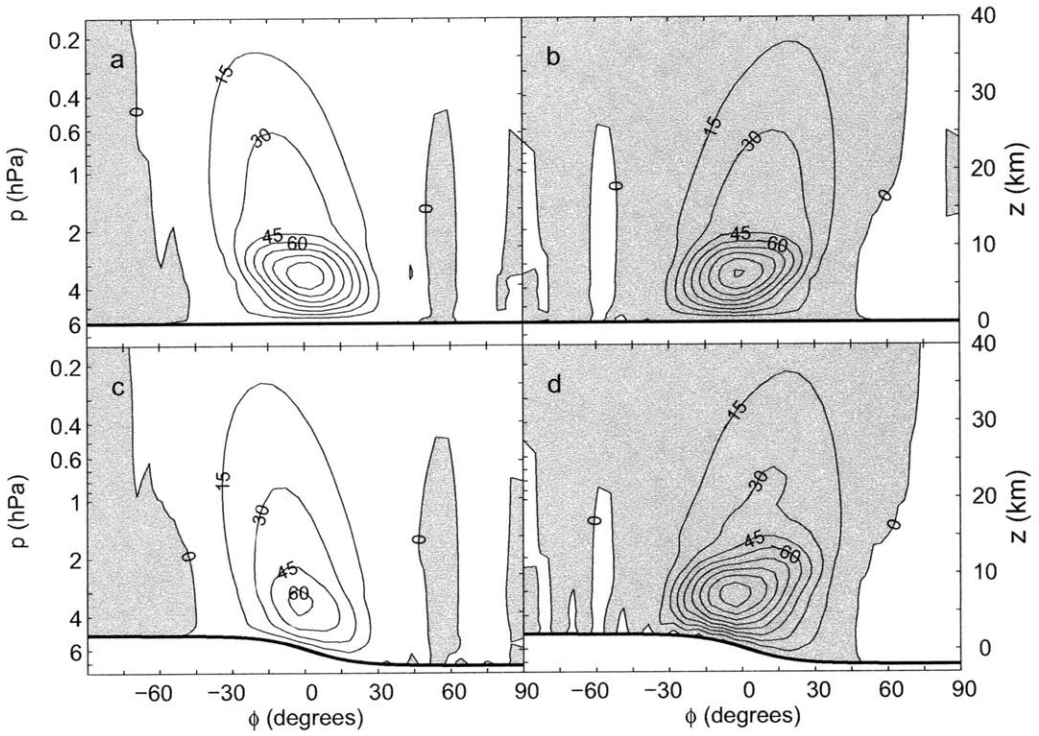

Figure 2-15: Zonally averaged mass stream function results from the GFDL MGCM, which uses a full radiation scheme. Units are 10^8 kg s^{-1}. Only temperatures below $\sim$0.2 hPa (40 km) are shown. The top row is for flat topography; the bottom is for idealized zonal mean topography (m=20). The left column is L_s=90° and the right is L_s=270°. Positive flow is counterclockwise; negative contours are shaded. Latitude is plotted on the x-axis, pressure is plotted on the left y-axis, and height is plotted on the right y-axis. Contour interval is 15×10^8 kg s^{-1}. The maximum magnitudes for panels (a), (b), (c), and (d) are 117, 121, 65, and 131 $\times 10^8$ kg s^{-1} respectively.

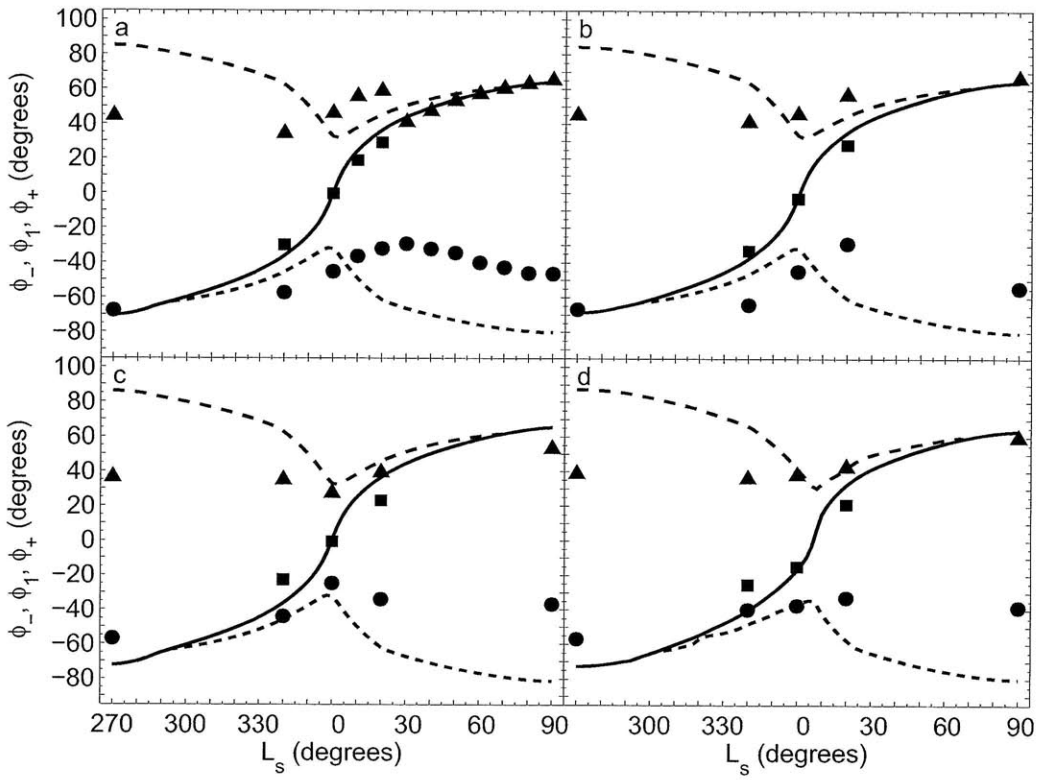

Figure 2-16: Solutions to (2.22)–(2.22). Panel (a) is the solution for pure radiative forcing with flat topography, (b) is the same as (a) but with zonal mean MOLA topography, (c) is radiative-convective forcing with flat topography, and (d) is the same as (c) but with zonal mean MOLA topography. In each panel, the dashed line is ϕ_+, the solid is ϕ_1, and the dotted is ϕ_-. Also plotted are the boundaries of cells obtained from the simple MGCM results. The triangles are ϕ_+, the squares are ϕ_1, and the circles are ϕ_-. As L_s approaches 90° and 270°, ϕ_1 and the poleward boundary of the summer cell becomes indistinguishable, and the value of ϕ_1 is not plotted.

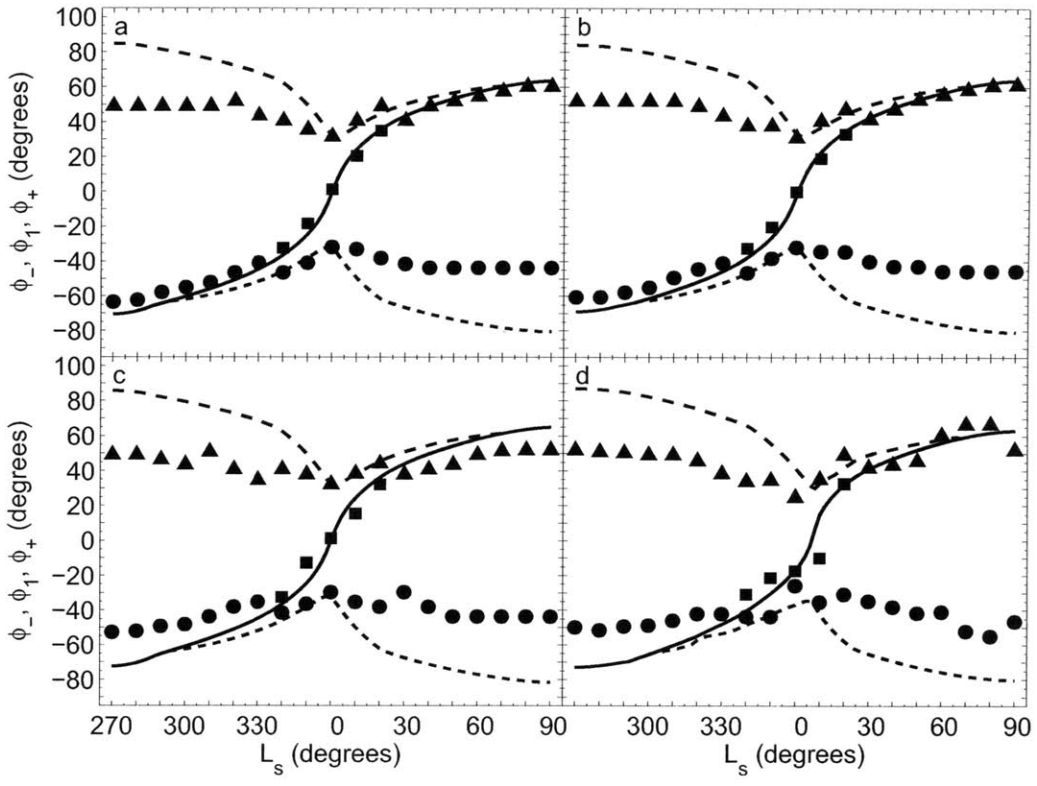

Figure 2-17: Same as Fig. 2-16, but the results for the axisymmetric simple MGCM are shown instead of the 3D simple MGCM.

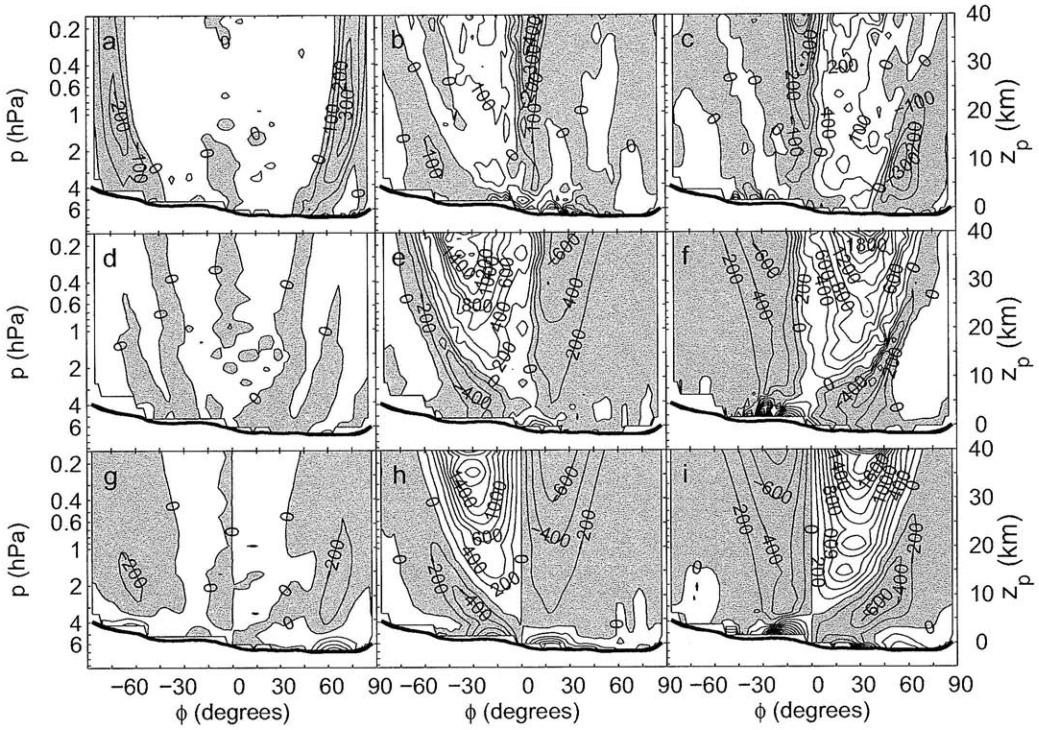

Figure 2-18: Simple MGCM results with radiative-convective forcing for the momentum budget derived in (2.42). Units are $m^2\ s^{-2}$. Latitude is plotted on the x-axis, pressure is plotted on the left y-axis, and log pressure height is plotted on the right y-axis, assuming a scale height of 11 km and a reference pressure of 6 hPa. Only results below ~0.2 hPa (40 km log pressure height) are shown. From left to right, the columns are L_s=0, 90, and 270°. From top to bottom, the rows are the meridional transport by spatial eddies (first term on the left hand side of (2.42)), combined meridional and vertical transport by the steady mean circulation (second and third terms on the left hand side of (2.42)), and the planetary term (right hand side of (2.42)). Negative contours are shaded. Note the different contour intervals (100 $m^2\ s^{-2}$ for the top row and 200 $m^2\ s^{-2}$ otherwise).

Chapter 3

The Effect of Zonally Varying Topography on the Martian Circulation in the Tropics

In the theory of Hadley circulation, a maximum in the diabatic heating at a specific latitude drives a circulation in the meridional and vertical directions. The most ubiquitous factor in determining the latitudinal boundaries of the circulation from a thermodynamic standpoint is the location of the subsolar latitude. The presence of an ocean with a high heat capacity (and the distribution of land and ocean) is important in modifying the circulation in the case of Earth, while the mean north-south topographic slope is important in the case of Mars.

We may also look for closed circulation patterns that occur in the zonal and vertical directions. One such example on Earth is in the equatorial Pacific, referred to as the Walker circulation. Latent heating from deep, convective regions of clouds over Indonesia provide a localized heat source. The air over this region rises, flows eastward along the equator (reaching as far as the South American coast), cools and sinks, then returns westward at low levels. The Martian atmosphere is not expected to have an exact equivalent, since latent heating due to CO_2 condensation occurs near the poles. However, we may return to elevated regions of topography acting as a localized heat source. An examination of Fig. 2-3a shows a relatively broad region of high topography located in the tropics between $-90°$ and $-135°$ longitude (known as the Tharsis region) that deserves further attention.

Webster [1977] paid particular attention to the effect of zonally varying topography on the Martian atmosphere in their study of the global circulation of Mars. They used a two-layer model containing the primitive equations on a sphere in pressure coordinates, linearized about a basic state. Dissipative terms were introduced that included surface drag, small-scale eddy turbulent exchange in the vertical, and Newtonian cooling. In addition to the Newtonian cooling, the diabatic heating contained a term to represent the heating effect of topography, given by

$$Q^* = C_v \Gamma(\phi, t) z_b(\phi, \lambda) k_w \tag{3.1}$$

where Q^* is the component of the heating rate due to topography, C_v is the specific heat at constant volume, Γ is the lapse rate, λ is the longitude, and k_w is the inverse of the time scale over which the temperature anomaly develops. Note that Γ is a function of latitude and time, prescribed as a cosine function maximizing at the latitude equal to the Sun's declination angle.

While the topography dataset used by Webster [1977] did not include the north-south slope, and therefore did not capture this aspect of the general circulation, it did capture the effects of the Tharsis region. These authors concluded that the heating effects of the mountains dominated over the mechanical effects, because the upward velocity was centered on the highest elevations and not upstream. They also noted an equatorial Kelvin wave.

The Webster [1977] model was aimed at being a general circulation model, its simplicity dictated in part by the available computing resources at the time. Gill [1980] performed a study whose goal was to investigate the response of the (terrestrial) tropical atmosphere given a distribution of heating with a deliberately simple model. The Gill [1980] model solves the forced shallow water equations with Rayleigh friction and Newtonian cooling on an equatorial beta-plane. If the diabatic heating perturbation is given as a sine function, then only the normal mode corresponding to the perturbation's frequency is excited and solutions are obtained from this mode.

Several important features are present in the solution for a diabatic heating perturbation located at 10° latitude north of the equator (i.e. one equatorial Rossby radius of deformation) and having a longitudinal extent of 40°. They are as follows: a concentrated region of upwelling located over the heat source and a broad region of downwelling at other longitudes; an eastward propagating Kelvin wave at low levels along the equator to the east of the heat source, resulting in easterly flow towards the heat source; a westward propagating Rossby wave at low levels to the west of the heat source, resulting in westerly flow towards the heat source; and a cyclone located slightly west of the maximum upwelling and a weaker anticyclone symmetric about the equator with respect to the cyclone. Due to the the slower propagation of the Rossby wave by a factor of three as compared with the Kelvin wave, the structures to the west of the heat source extend one third of the distance of the eastern extent.

It is worthwhile to revisit the circulation near the Tharsis region with a modern GCM, specificaly the simple MGCM of Section 2.3, and to compare with the Gill [1980] model. Figures 3-1–3-3 show a longitude-height cross section of the flow (u and $-\omega$ components) from the simple MGCM results with radiative-convective forcing at L_s=0, 90, and 270°, respectively. The flow is time averaged and meridionally averaged between latitudes −30 to 30°. This range corresponds to the approximate width of the Hadley cells (see Fig. 2-11). The zonally averaged component has been subtracted to more easily see the effect of topography, since the flow is dominated by zonal jets, especially at higher altitudes.

At all three seasons, strong upwelling occurs over the topographic feature between -90 and -135° longitude. This upwelling must be caused by the elevated heating aloft at this longitude associated with the higher topography, since the results with pure radiative forcing do not show this type of flow. Downwelling, albeit less intense, is present at −180° longitude and at 0 to −45° longitude at equinox and −45 to −90°

longitude at the solstices. The circulation does not exhibit the behavior of the Gill [1980] solution in which the circulation pattern extends three times farther in the eastward direction than in the westward direction.

Divergence occurs at around 2 hPa in the region of the most elevated topography; convergence at 4 to 5 hPa. Figures 3-4–3-6 show horizontal cross sections of the u and v flow at the model levels that most closely match the levels with convergent flow for L_s=0, 90, and 270°, respectively. The flow does not appear to show any structure in the vicinity of the elevated topography, such as a Kelvin or Rossby wave along the equator or circular flow indicating a cyclone or anticyclone offset from the equator.

Since the MOLA topography is data and contains small scale variations that could be affecting the circulation, the simple MGCM experiments were redone with an idealized topography having a broad mountain offset from the equator superimposed on the zonally averaged MOLA topography. This specification for topography attempts to capture the Tharsis region while preserving the north-south slope, which is crucial to the global circulation. While surface topography data is important, this step attempts to deconstruct the topography to determine the affects of these specific components. The topography z_m (in km) is given by:

$$z_m = z_{mm} + 10 \exp\left\{-\left[(\phi + 10°)^2 + (\lambda + 105°)^2\right]/100\right\} \tag{3.2}$$

where z_{mm} is the MOLA mean topography (in km) and ϕ and λ are in degrees. This idealized topography with an off-equatorial mountain is shown in Fig. 3-7.

Figures 3-8–3-10 show longitude-height cross sections of the flow for the idealized topography with an off-equatorial mountain for L_s=0, 90, and 270°, respectively; Figures 3-11–3-13 show horizontal cross sections of the flow. The results for these experiments are puzzling in that they are as noisy as the runs with full MOLA topography and still do not resemble the Gill [1980] model. One possible reason for discrepancy with the Gill [1980] model is that in the case of Mars, the heat source (i.e. the mountain) creates a physical obstruction that alters the flow. Moreover the radiative forcing in the Gill [1980] model has no height dependence, while the heating anomaly imposed by the idealized mountain becomes smaller in area at higher levels as the top of the convecting layer is reached on the fringes of the mountain.

The internal equatorial Rossby radius of deformation is given by $\sqrt{NHa/2\Omega}$, where N is the Brunt-Väisälä frequency and H is the equivalent depth. Taking H = 15 km (the same as the depth used in the Lindzen and Hou [1988] model) and the remaining parameters from Table 1.2, the radius of deformation is $\sim$ 1500 km, which is higher than the terrestrial value of $\sim$ 1000 km. A higher radius of deformation implies that the heat source (i.e. the mountain) must be placed at a higher distance from the equator to obtain a setup analogous to the example of an off-equatorial heat source at one deformation radius presented in Gill [1980]. The smaller planetary radius of Mars results in the heat source being at 25° latitude off the equator (1° latitude = 59 km on Mars). Apparently, this Gill [1980] example is not quite as applicable to Mars as our early intuition suggested.

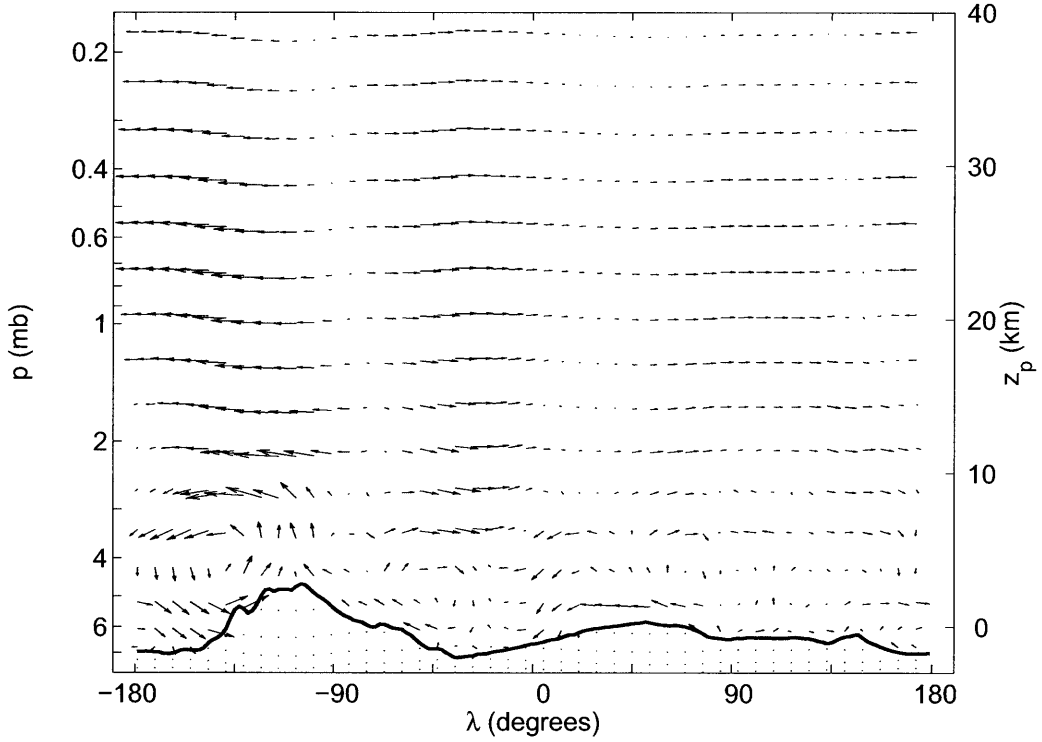

Figure 3-1: Longitude-height cross section of flow from simple MGCM results with radiative-convective forcing, with vectors (arrows) calculated from time-averaged u (m s^{-1}) and $-\omega$ (10^{-4} Pa s^{-1}) for L_s=0° and MOLA topography. Meridional averaging was performed over latitudes −30 to 30°. The vectors have been plotted about every 10° longitude for easier viewing. The zonal mean has been subtracted from the flow field, which is scaled to the largest magnitude vector in the field. Longitude is plotted on the x-axis, pressure is plotted on the left y-axis, and log pressure height is plotted on the right y-axis, assuming a scale height of 11 km and a reference pressure of 6 hPa. Only results below ~0.2 hPa (40 km log pressure height) are shown. The solid line denotes the latitudinally averaged topography for this range of latitudes.

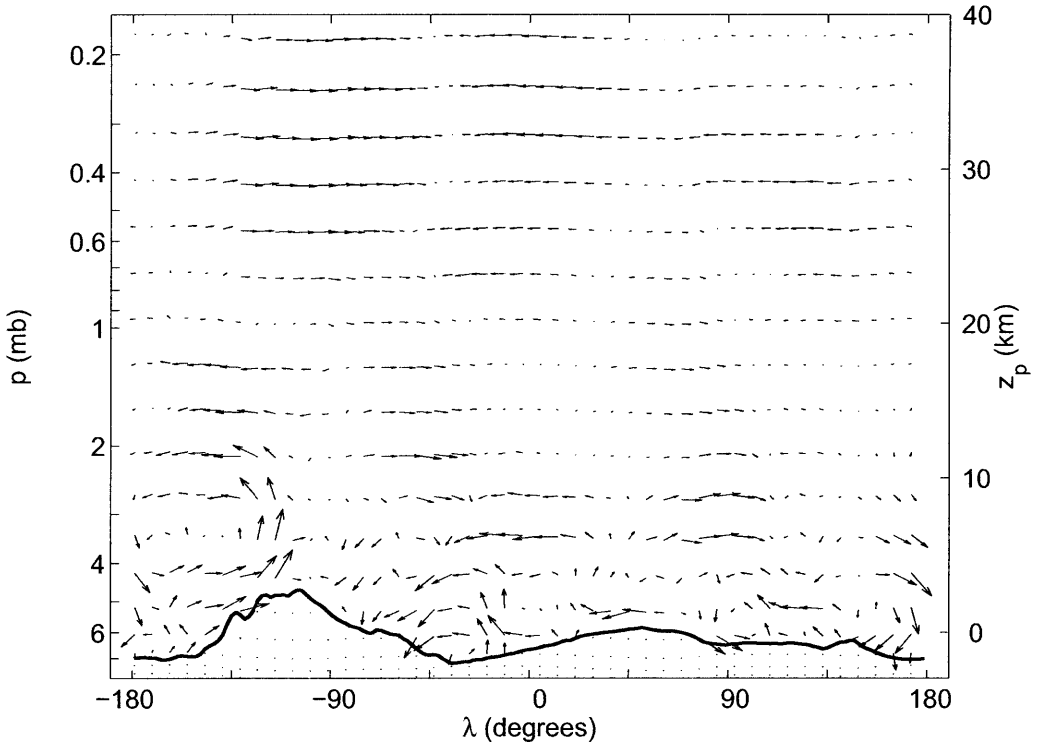

Figure 3-2: Same as Fig. 3-1 but for L_s=90°.

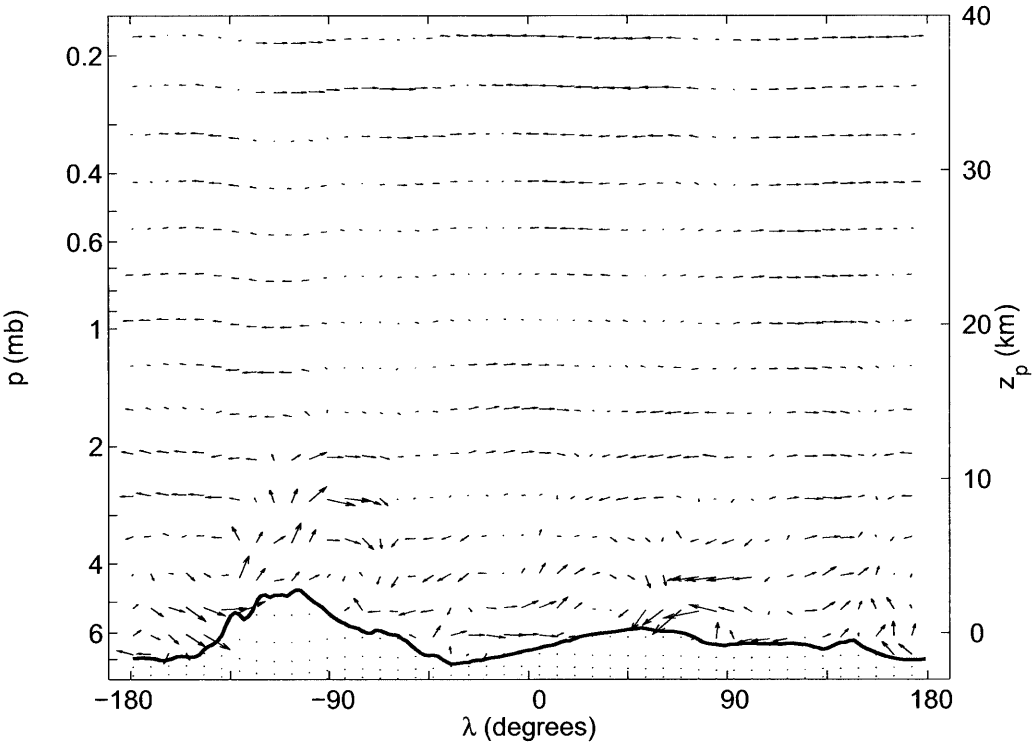

Figure 3-3: Same as Fig. 3-1 but for L_s=270°.

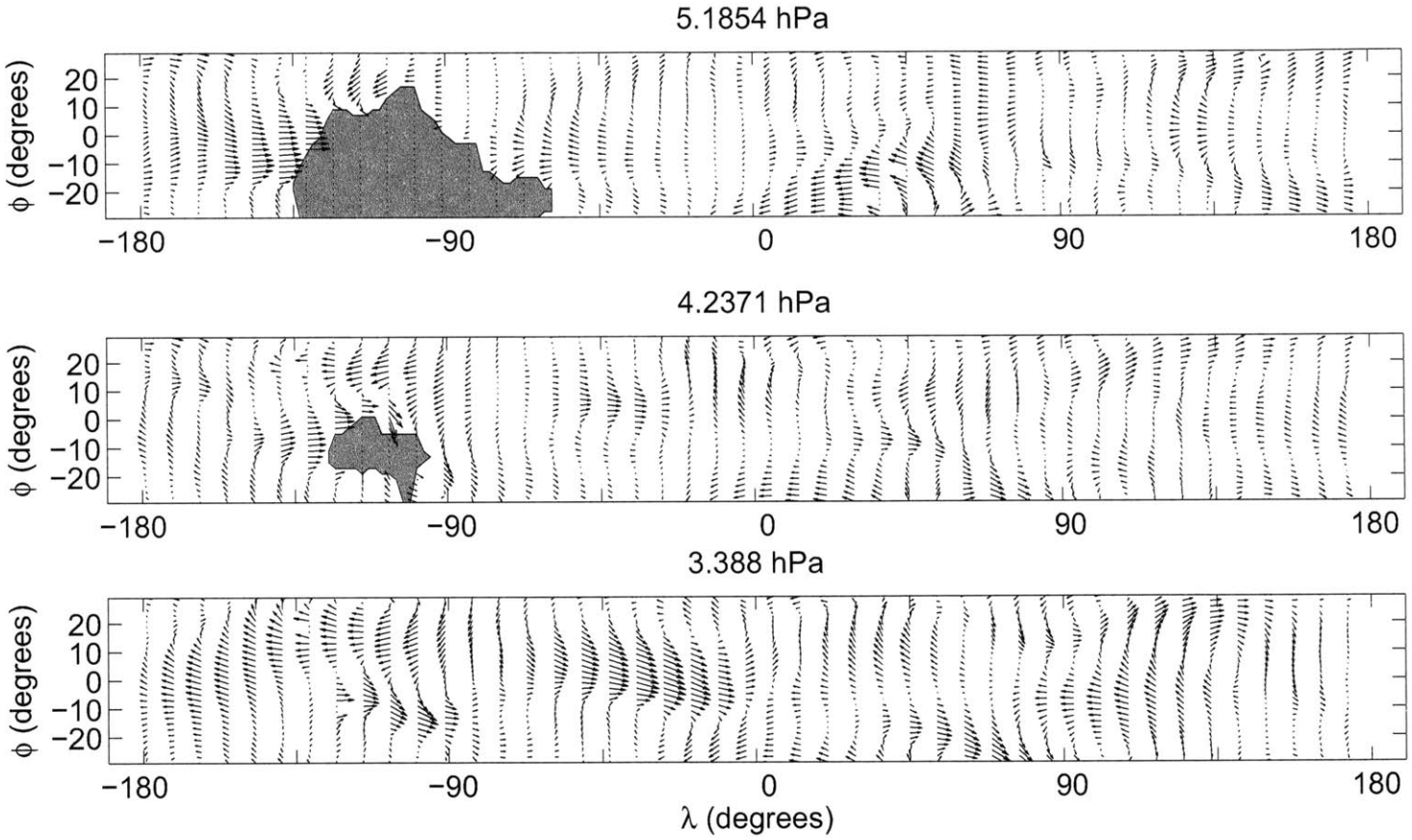

Figure 3-4: Horizontal cross section of flow from simple MGCM results with radiative-convective forcing, with vectors (arrows) calculated from time-averaged u and v for L_s=0° and MOLA topography. Meridional averaging was performed over latitudes −30 to 30°. The vectors have been plotted about every 10° longitude for easier viewing. The zonal mean has been subtracted from the flow field, which is scaled to the largest magnitude vector in the field in each panel. The label above each panel indicates the initial pressure of that level; the nature of the η coordinate system causes the pressure on each model level to adjust based on the surface pressure at subsequent time steps. The gray shaded area denotes regions where the ground intersects the pressure surface. The log pressure height of the surfaces from top to bottom are 1.6 km, 3.8 km, and 6.3 km.

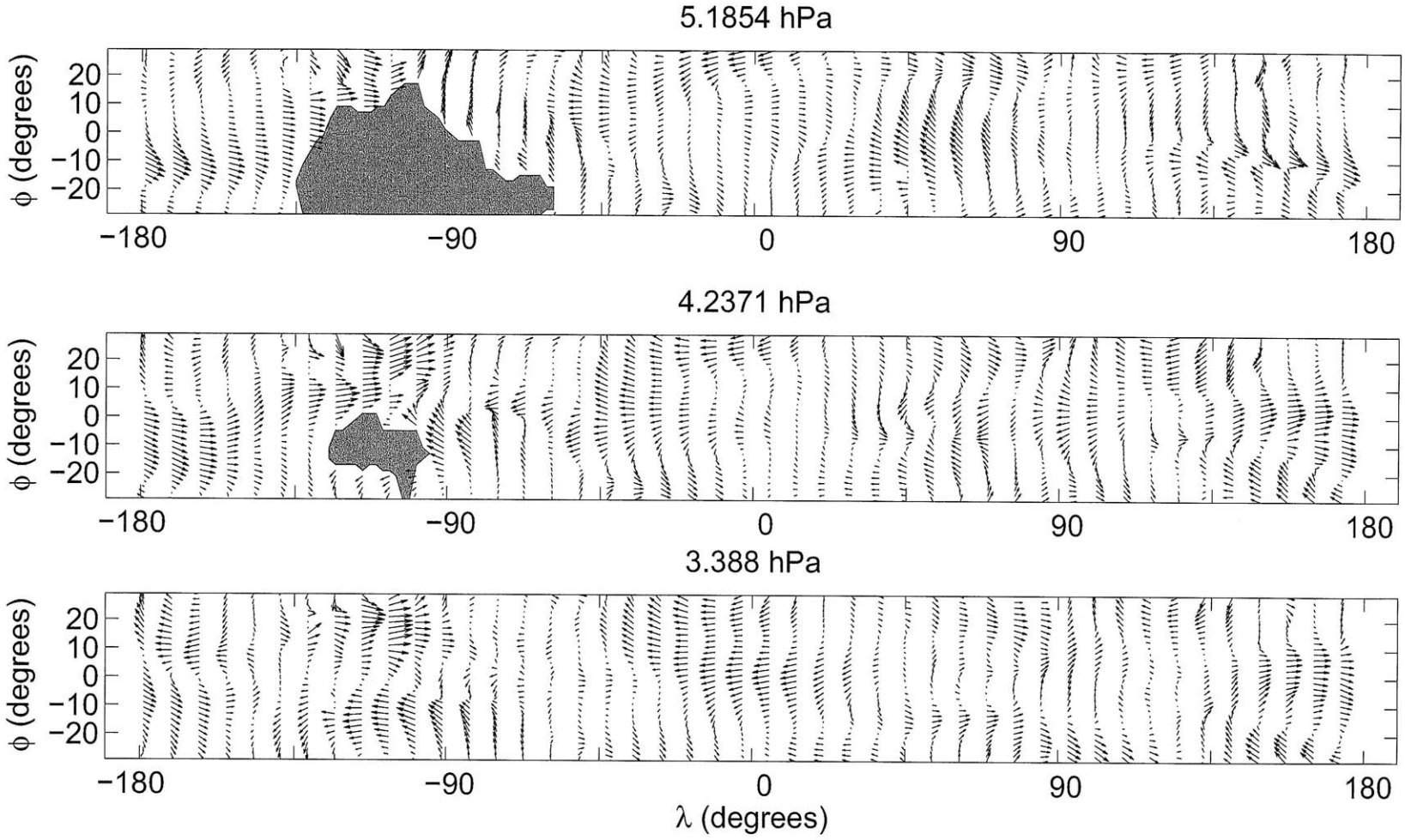

Figure 3-5: Same as Fig. 3-4 but for L_s=90°.

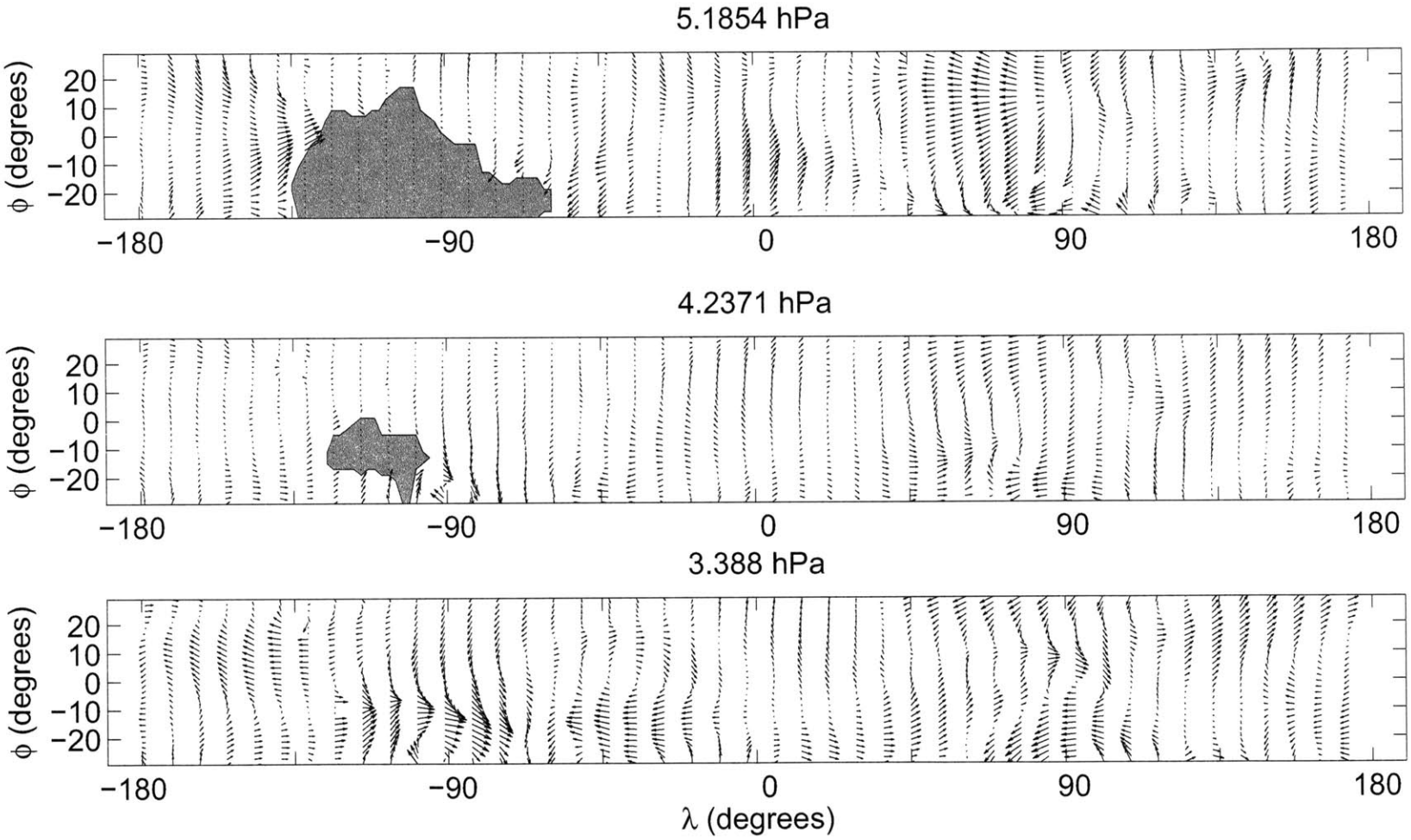

Figure 3-6: Same as Fig. 3-4 but for L_s=270°.

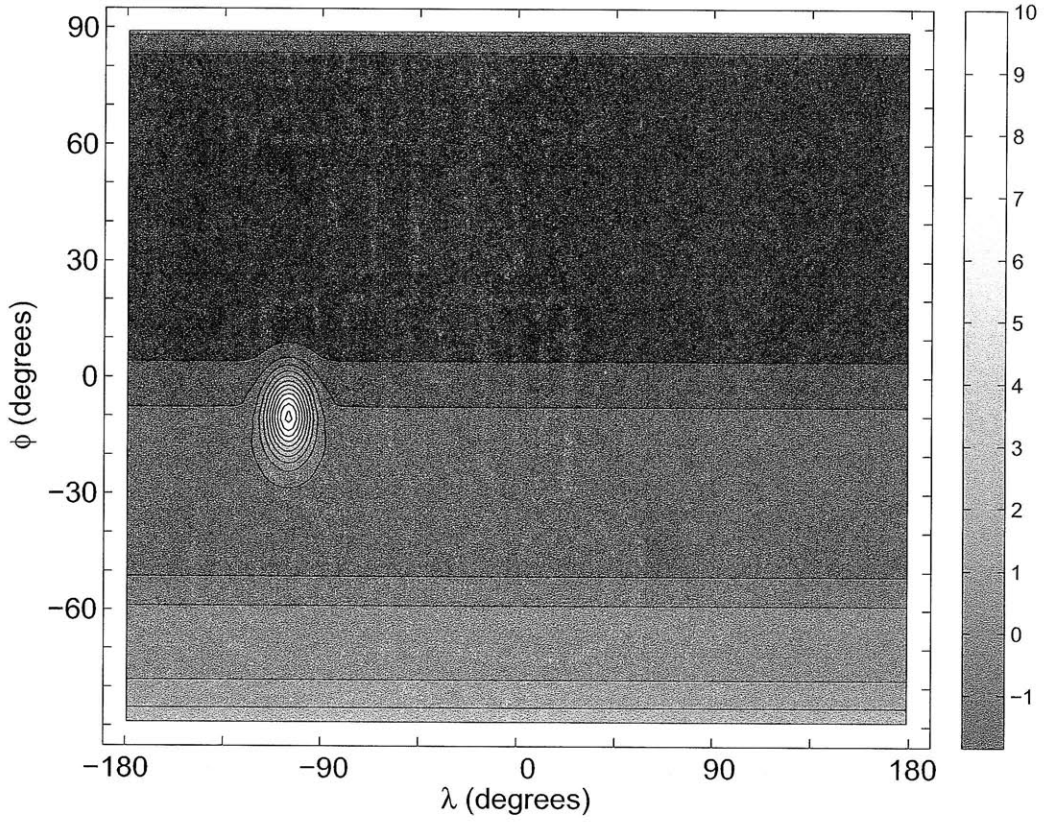

Figure 3-7: MOLA mean topography with an off-equatorial mountain (km). Contour lines are drawn at 1 km intervals.

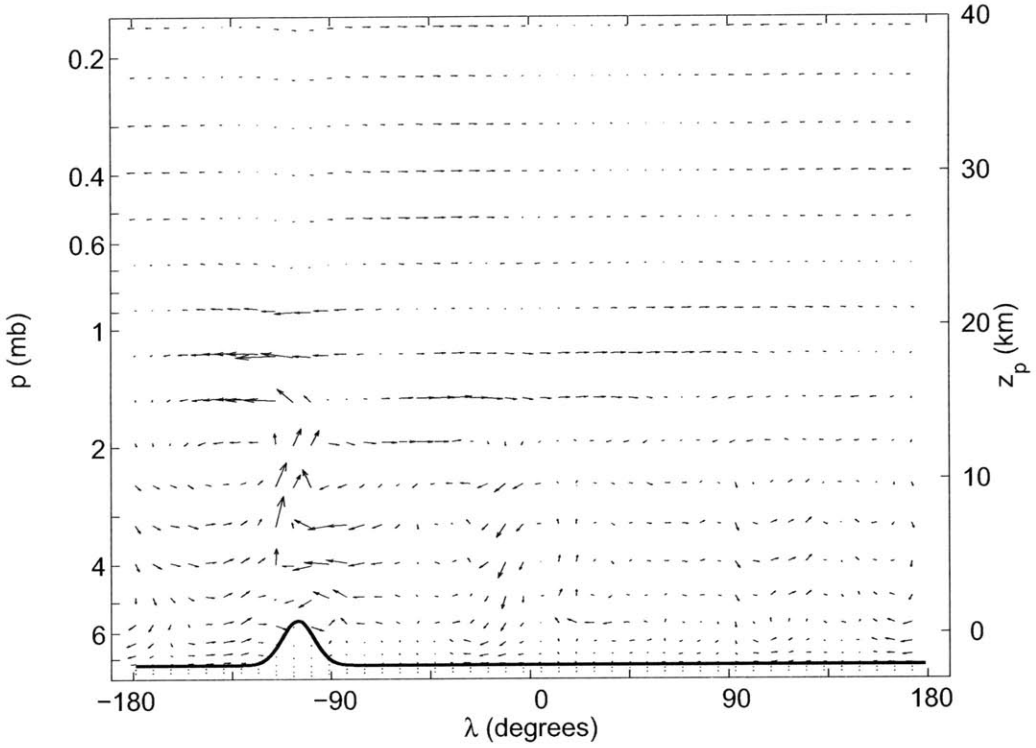

Figure 3-8: Longitude-height cross section of flow from simple MGCM results with radiative-convective forcing, with vectors (arrows) calculated from time-averaged u (m s^{-1}) and $-\omega$ (10^{-4} Pa s^{-1}) for L_s=0° and MOLA mean topography with an off-equatorial mountain. Meridional averaging was performed over latitudes −30 to 30°. The vectors have been plotted about every 10° longitude for easier viewing. The zonal mean has been subtracted from the flow field, which is scaled to the largest magnitude vector in the field. Longitude is plotted on the x-axis, pressure is plotted on the left y-axis, and log pressure height is plotted on the right y-axis, assuming a scale height of 11 km and a reference pressure of 6 hPa. Only results below ~0.2 hPa (40 km log pressure height) are shown. The solid line denotes the latitudinally averaged topography for this range of latitudes.

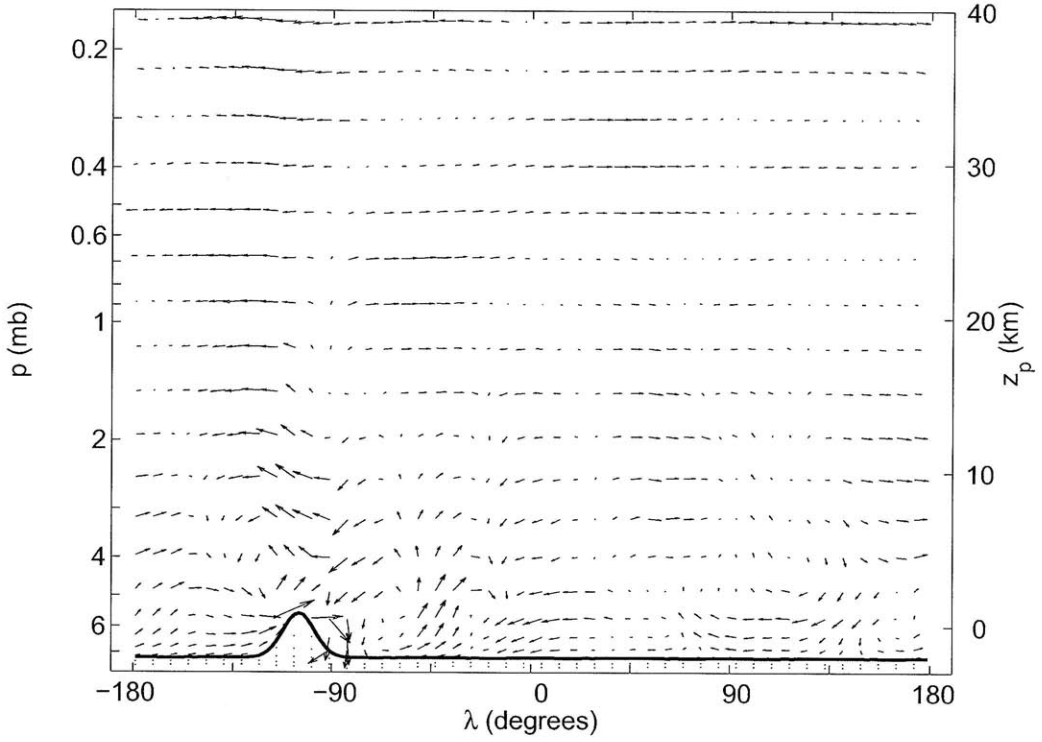

Figure 3-9: Same as Fig. 3-8 but for L_s=90°.

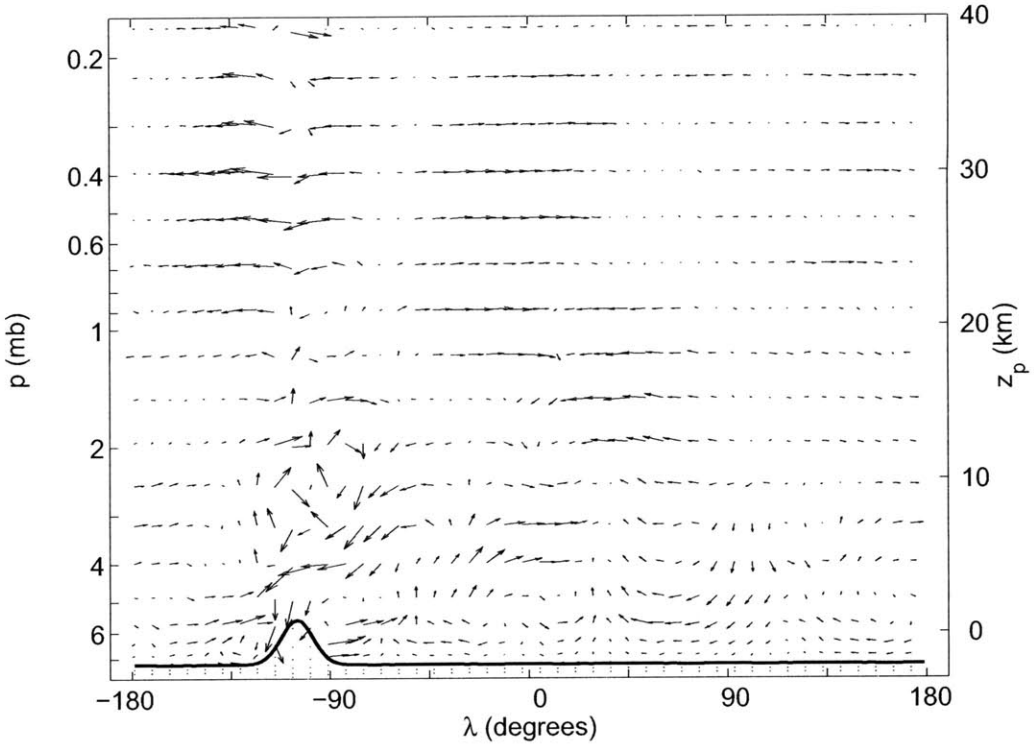

Figure 3-10: Same as Fig. 3-8 but for L_s=270°.

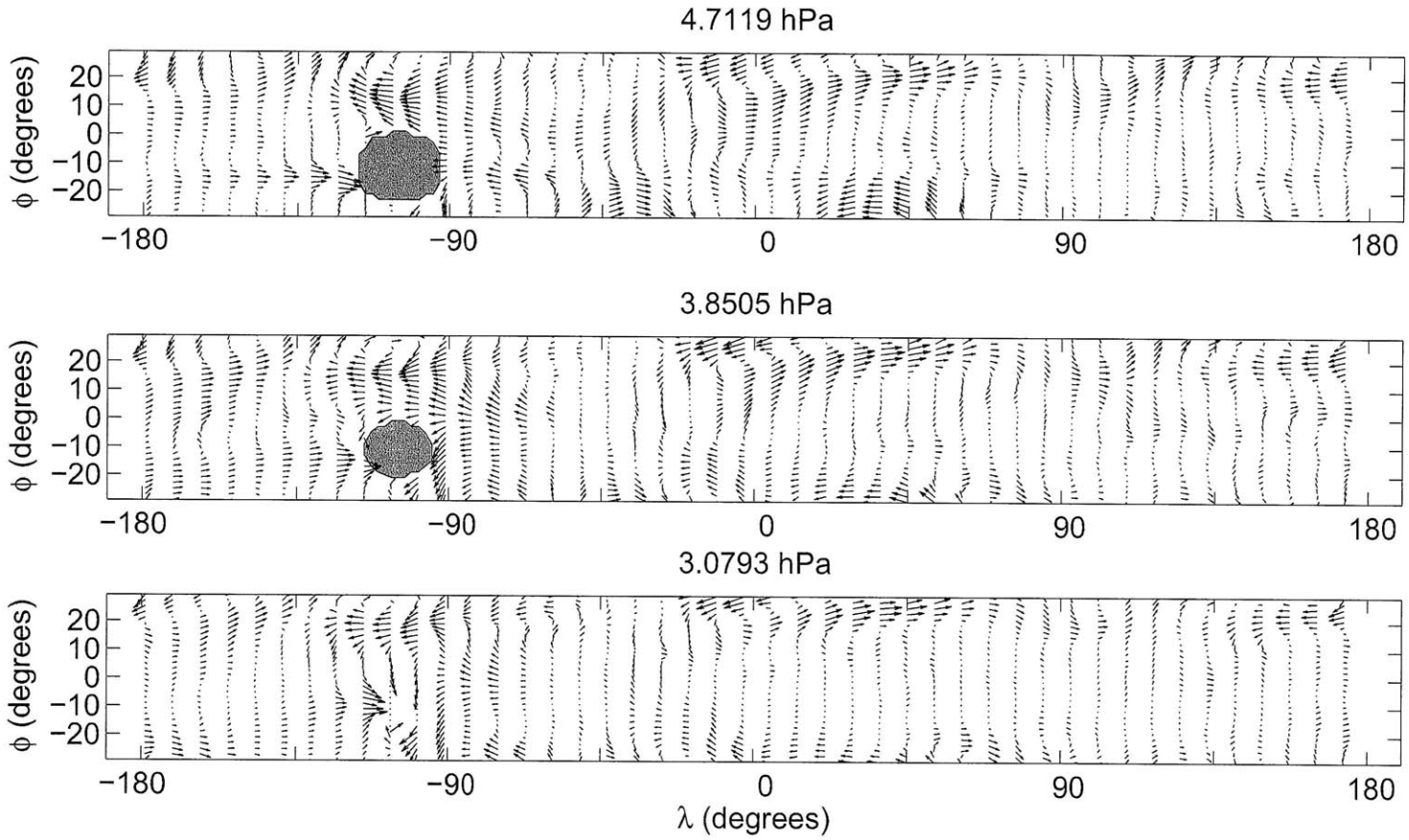

Figure 3-11: Horizontal cross section of flow from simple MGCM results with radiative-convective forcing, with vectors (arrows) calculated from time-averaged u and v for L_s=0° and MOLA mean topography with an off-equatorial mountain. Meridional averaging was performed over latitudes −30 to 30°. The vectors have been plotted about every 10° longitude for easier viewing. The zonal mean has been subtracted from the flow field, which is scaled to the largest magnitude vector in the field in each panel. The label above each panel indicates the initial pressure of that level; the nature of the η coordinate system causes the pressure on each model level to adjust based on the surface pressure at subsequent time steps. The gray shaded area denotes regions where the ground intersects the pressure surface. The log pressure height of the surfaces from top to bottom are 2.7 km, 4.9 km, and 7.3 km.

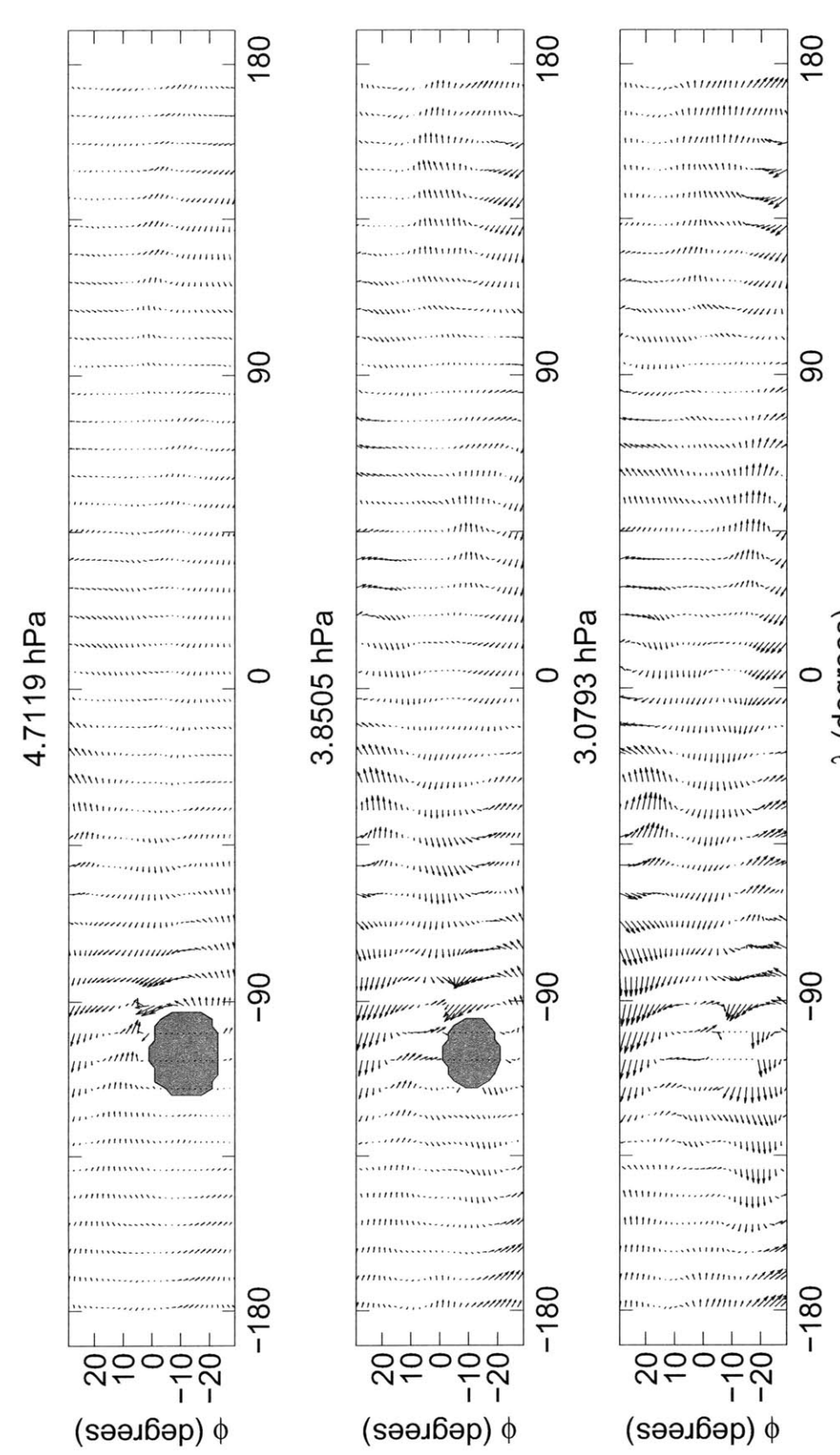

Figure 3-12: Same as Fig. 3-11 but for L_s=90°.

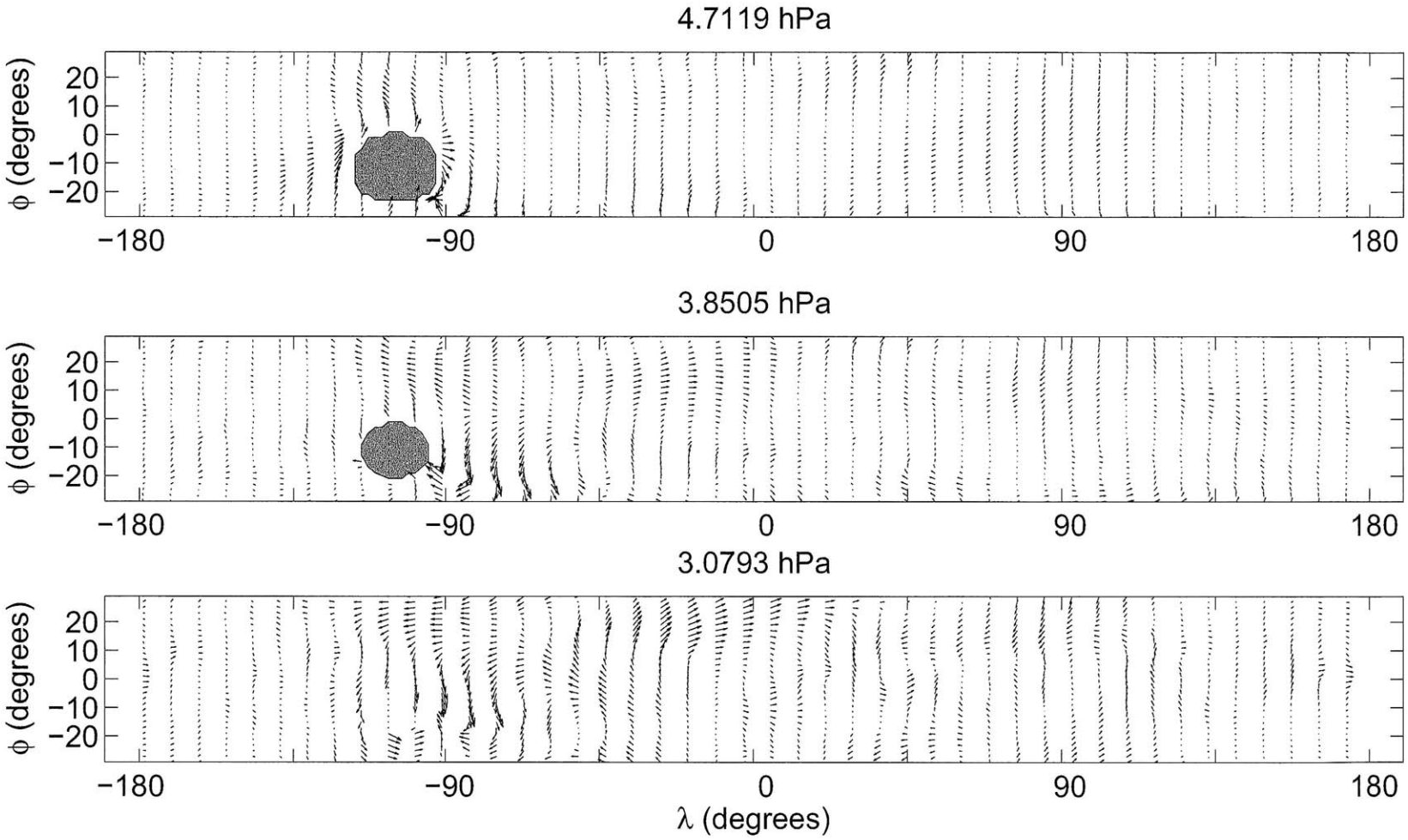

Figure 3-13: Same as Fig. 3-11 but for L_s=270°.

Chapter 4

An Analysis of Pluto Occultation Light Curves Using an Atmospheric Radiative-conductive Model

4.1 Calculating model light curves

4.1.1 Radiative-conductive atmospheric model

Strobel et al. [1996] describe in detail their model for calculating Pluto's atmospheric temperature as a function of height, and the model will be only briefly summarized here. Assuming a hydrostatic atmosphere, the following 1-D heat balance equation is solved numerically for T in the steady state:

$$c_p \rho \frac{\partial T}{\partial t} = \frac{1}{r} \frac{\partial}{\partial r} \left(r^2 K \frac{\partial T}{\partial r} \right) + R_{net}, \tag{4.1}$$

where t is time, c_p is the specific heat at constant pressure, ρ is the density, K is the thermal conductivity, and R_{net} is the heating rate. A primarily N_2 atmosphere is assumed with smaller amounts of CH_4 and CO. For an N_2, CH_4, and CO mixture,

$$K = K_o T^{\alpha} \tag{4.2}$$

with $K_o = 5.63 \times 10^{-5}$ J m^{-1} s^{-1} K$^{-(\alpha+1)}$ and $\alpha = 1.12$ [Hubbard et al., 1990]. The most mathematically complex part of the model is the specification of R_{net}, which is the sum of the non-local thermodynamic equilibrium (LTE) heating rate by solar near-IR absorption in the CH_4 2.3 and 3.3 μm vibrational bands, the non-LTE cooling rate due to the CH_4 7.6 μm vibrational band, and the LTE cooling rate by CO rotational line emission. Disk-averaged solar flux is used to compute the heating rates. At present, I assume a stratosphere only model (i.e. no troposphere is included).

The top boundary condition is given by

$$K\frac{\partial T}{\partial r} = 0, \tag{4.3}$$

or no net heat flux. The model top is set at an altitude of $\sim$ 600 km. Since we are interested in the thermal structure of the lower atmosphere, the model top is arbitrary, as long as it is well above the region of interest, but low enough that the continuum fluid assumption still applies. The bottom boundary condition is given by specifying surface radius (r_s), surface pressure (p_s), and surface temperature (T_s). Given that Pluto occultation light curves do not probe down to the surface, this choice of free parameters may not seem ideal; however, the values of atmospheric variables at the surface affect the entire model temperature profile (since radiative balance must be maintained) and thus the light curve, as shown below.

The CH_4 volume mixing ratio (with respect to N_2), γ, is

$$\gamma(r) = \gamma_o \left(\frac{n(r)}{n_o}\right)^{\beta}, \tag{4.4}$$

where γ_o is the mixing ratio at the surface, n is the number density, n_o is the value of n at the surface, and β is the CH_4 power index. I assume here that CH_4 is well mixed, i.e. β=0, based on chemical models that indicate that CH_4 mixing ratios must be an order of magnitude lower than observed before chemical loss dominates diffusion [Summers et al., 1997]. The CO volume mixing ratio (with respect to N_2), η, is also assumed constant throughout the depth of the atmosphere, as photochemical sources and sinks of CO are negligible.

4.1.2 Light curve model

Using the ideal gas law and assuming hydrostatic balance, n may be derived from the solutions to (4.1). The total atmospheric refractivity ν may be related to n using

$$\nu\,(r) = \nu_{STP}\frac{n\,(r)}{L_o}, \tag{4.5}$$

where L_o is the Loschmidt constant and ν_{STP} is the refractivity at standard temperature and pressure. The latter is a function of wavelength, and is calculated for a pure N_2 atmosphere from Peck and Khanna [1966]. As a light ray passes through an atmosphere, it is bent by a refraction angle θ given by

$$\theta(r) = \int_{-\infty}^{\infty} \frac{r}{r'}\frac{d\,\nu(r')}{d\,r'}\,dx \tag{4.6}$$

and whose derivative is

$$\frac{d\theta(r)}{dr} = \int_{-\infty}^{\infty}\left[\frac{x^2}{r'^3}\frac{d\nu(r')}{dr'} + \frac{r^2}{r'^2}\frac{d^2\nu(r')}{dr'^2}\right]dx \tag{4.7}$$

[Chamberlain and Elliot, 1997]. In (4.6) and (4.7), x is the distance along the ray path measured from the point of closest approach, or

$$x^2 = r'^2 - r^2, \tag{4.8}$$

where r' is the radial distance from the center of the body along the path of the ray. See Fig. 4-1 for a schematic of occultation geometry.

The integrals in (4.6) and (4.7) are integrated numerically after interpolating $d\nu/dr$ and $d^2\nu/dr^2$ in r space. When $r > r_{top}$, where r_{top} is the top radius of the model, I assume constant temperature, or $T(r > r_{top}) = T(r_{top})$, and calculate the appropriate values for the refractivity first and second derivatives. In practice, x may not be taken to infinity, for this requires ν to be evaluated at infinite r'. The numerical integration is carried out to a finite value of $r' = r_{max}$, where $r_{max} \gg r_{top}$.

From Elliot and Young [1992], the light curve flux ψ for a single limb is given by

$$\psi = \left(\frac{1}{1 + D[d\theta(r)/dr]}\right)\left(\frac{1}{1 + D\theta(r)/r}\right)\exp[-\tau_{los}(r)], \tag{4.9}$$

where τ_{los} is the optical depth along the path of the ray, and D is the distance to the observer. To obtain the total flux, perpendicular limb points must be summed (see Elliot and Olkin [1996] for more details). I assume a spherical atmosphere. Light curve data is flux as a function of time t while (4.9) is flux as a function of r. Implicitly, t and r are related by

$$y = r + D\theta(r) \tag{4.10}$$

and

$$y^2 = y_{min}^2 + V^2(t - t_{min})^2, \tag{4.11}$$

where y is the distance from the center of the shadow plane, y_{min} is the distance of closest approach to the center of the shadow plane, V is the relative velocity between the observer and the occulting body, and t_{min} is the time of closest approach. I assume that the light curve is symmetric about t_{min}, i.e. that the atmospheric properties on the immersion limb are the same as those on the emersion limb.

Whether or not Pluto's atmosphere is clear (i.e. $\tau_{los} = 0$) for each occultation event is inconclusive. The kink in the 1988 KAO light curve prompted Elliot and Young [1992] to develop a haze model to explain the rapid drop off in flux below the kink. Presumably, an absorbing haze layer was extinguishing the starlight. Stansberry et al. [1994] found that they were able to explain the kink by invoking a steep temperature gradient with temperature decreasing with depth in the lower atmosphere, but did not provide a physical explanation for how this steep gradient could be accomplished. Elliot et al. [2003b] noted a wavelength dependence in the 21 August 2002 occultation data that was too large to be due to the dependence of refractivity on wavelength, and was thus attributed to a wavelength-dependent haze extinction. However, Young et al. [2008b] observed no wavelength dependence in their observations of the 31 July 2007 occultation. For the light curves analyzed here, I assume a clear atmosphere.

4.1.3 Sensitivity of light curve to model parameters

To show the effect of the radiative-conductive atmospheric model parameters on the light curve, a series of test cases was performed where T_s, p_s, γ_o, η, and r_s were varied about control values of 37 K, 18 μbar, 6×10^{-3}, 5×10^{-4}, and 1152 km, respectively. A summary of the test cases is given in Table 4.1. The choice of parameters and their variations is meant to be illustrative. T_s is constrained by observations of surface ice and the assumption that the atmosphere is in vapor pressure equilibrium with the surface ice [Tryka et al., 1994]. The range in p_s was chosen to demonstrate the effect of doubling surface pressure as suggested by the analysis of Elliot et al. [2003b]. The choice of γ_o is subjective since the temperature profiles and light curves depend nonlinearly on γ_o. The range chosen reflects values obtained in previous measurements [Young et al., 1997; Lellouch et al., 2009] while still affording a relatively large variability in the light curves. The range in η was chosen to show that the model light curves are highly insensitive to this parameter. The chosen range of r_s is approximately the values spanned by the radius and its upper error bar determined from stellar occultation measurements by Elliot et al. [2007] of 1152±32 km.

Figures 4-2–4-6 show the light curves calculated for each test case in addition to the control light curve and the residuals (*control* − *test*). The light curves are calculated for a geometry corresponding to that of the Siding Spring light curve from the 12 June 2006 occultation [Elliot et al., 2007]. The difference in the test case light curve with the control case is apparent for a variation in p_s (case 2), and barely discernible in the light curve plot for a change in γ_o (case 3) or r_s (case 5). For a change in T_s or η, (cases 1 and 4, respectively), the difference with the control is not easily seen at this scale. Figure 4-7 shows the percent difference, defined as $((control - test)/control) \times 100$, for each of the five test cases, so that the relative difference between the control and the test cases can be more easily seen. It is clear that for this set of parameters, the variation in p_s affects the light curve the most, followed secondarily by r_s and γ_o. Changes in T_s and η have a tertiary effect. Further sensitivity tests (not shown) indicate that above $\gamma_o \approx 6 \times 10^{-3}$, the variations between the light curves become much less pronounced than those between lower values of γ_o.

Figure 4-8 shows the temperature profiles that correspond to the five test cases plotted with the control case. For an increase in surface temperature from 37 to 42 K (upper left panel), the warmer surface creates a warmer profile overall, but the difference decreases with height. For a decrease in surface pressure from 18 to 9 μbar (left middle panel), the temperature below 1450 km radius cools by as much as 8 K. For a decrease in γ_o from 6×10^{-3} to 2×10^{-3} (lower left panel), a net cooling of about 10–15 K occurs everywhere except in the lowest 20 km above the surface. For an increase in η from 5×10^{-4} to 200×10^{-4} (upper right panel), a net cooling exists that increases with radius. At the model top the difference in temperature is $\sim$ 50 K. Because the light curve is not sensitive to this magnitude of difference in η (see Fig. 4-7), cooling at high altitudes would not be detected by the light curve fitting procedure if the true atmosphere lies in this range. The effect of changing surface radius is to simply shift the entire temperature profile vertically (middle right panel of Fig. 4-8).

4.2 Least-squares fitting of the light curve data to the radiative-conductive atmospheric model

As demonstrated in Fig. 4-7, the model light curve is much less sensitive to values of T_s and η than the remaining parameters; these parameters were fixed at 37 K and 5×10^{-4}, respectively for the least-squares fitting procedure. Note that this value for η is less than the upper limit of 5×10^{-3} set by Lellouch et al. [2010] assuming a 15 μbar surface pressure. The refractivity derivatives $d\nu/dr$ and $d^2\nu/dr^2$ were calculated from the radiative-conductive atmospheric model and numerical differentiation of (4.5) for a grid of p_s, γ_o, and r_s values. The grid increments (nonlinear in the case of γ_o) were chosen with fine enough resolution so that interpolation using a cubic polynomial approximated points in between the grid well. The interpolation was performed at this step as recommended by Chamberlain and Elliot [1997] instead of on the light curve flux, since the light curve flux is not as smooth as the refractivity derivatives and may contain discontinuities and abrupt changes. With the interpolated refractivity derivatives, (4.6)–(4.11) were used to calculate a model light curve as a function of t, p_s, γ_o, r_s and the particular geometry (v, y_{min}, t_{min}, D) of the station and event.

Background flux present in the data was added to the model light curve as [following Elliot and Young, 1992]

$$\Lambda = \chi(t)(1 - s_{bf})[s_{fs} + s_s(t - t_{min})] + s_{bf}[s_{fs} + s_s(t - t_{min})], \qquad (4.12)$$

where Λ is the unnormalized light curve flux, χ is the normalized light curve flux, s_{bf} is the background fraction, s_{fs} is the full scale flux, and s_s is the slope. The background fraction was determined separately from the observations by calculating the ratio of fluxes (Pluto+Charon)/(Pluto+Charon+star). In addition to the atmospheric parameters (p_s, γ_o, and r_s), s_{fs}, s_s, and t_{min} were left as free parameters in the least-squares fit.

Table 4.2 shows the dates, stations, and signal-to-noise ratio (SNR) per scale height for the occultation data under consideration, specifically, 9 June 1988 [Elliot et al., 1989; Millis et al., 1993], 21 August 2002 [Elliot et al., 2003b], 12 June 2006 [Elliot et al., 2007], 18 March 2007 [Person et al., 2008], and 24 June 2008 [Gulbis et al., 2010]. Lines in bold indicate datasets which are included in the analysis below. Appendix B shows light curve data for the stations and events listed in Table 4.2.

To test the effect of SNR per scale height on the least-squares fitting procedure, a model light curve was calculated with synthetic, normally distributed random noise added at a level so as to obtain the desired SNR per scale height. The synthetic data was then least-squares fit to the parameters p_s, γ_o, and r_s and the results compared with the parameters used to generate the original light curve. Below a SNR of approximately 90 per scale height, the least-squares fit results no longer agreed with the parameters originally used to generate the synthetic light curve. This test implied that the only observations that can be potentially reliably fit using these three parameters are the 1988 KAO, the 2002 UH 2.2m, the 2006 Siding Spring, and the 2007 MMT (visible and IR).

Figure 4-9 shows the normalized 2006 Siding Spring data, best-fit light curve, and

residuals. Since the residuals do not show any low frequency structure, I concluded that the model fit is satisfactory. This dataset is the only one for which I could fit for all three parameters (p_s, γ_o, and r_s) and for the entire range of flux.

The 2007 MMT residuals (not shown) exhibit an increase in the scatter during the occultation that is not present before immersion or after emersion, which was attributed to waves in the atmosphere [Person et al., 2008]. This dataset (Figs. B-7c and B-8a) had the highest SNR per scale height, and any waves present during the other occultations were apparently not resolved. Since the radiative-conductive atmospheric model does not include waves, I do not consider any fits to the 2007 MMT data using the atmospheric model to be trustworthy. The 1988 KAO residuals (not shown) contain structure, as is to be expected since the atmospheric model is not capable of generating a kink in the light curve [c.f. Stansberry et al., 1994]. The 2002 UH 2.2m residuals (not shown) also contain structure, and it is apparent from a visual inspection of the data that the fit disagrees with the data particularly at low flux levels. If there is extinction in the lower part of the 1988 KAO light curve (Fig. B-1a), the extinction-causing agent is apparently still present in the 2002 UH 2.2m data (Fig. B-4a), but has subsided by 2006. Although Elliot and Young [1992] presented an extinction model, this model would not be physically consistent with the radiative-conductive model so I cannot use it here. As such I chose to do a new fit on the 1988 KAO light curve above the kink, or about the 0.4 normalized flux level. Since an abrupt kink is not readily obvious in the 2002 UH 2.2m data, I also do a new fit for this data above the 0.4 normalized flux level.

Again using synthetic light curve tests, I found that it was impossible to reliably fit only the top portion of the light curve with p_s, γ_o, and r_s as free parameters at the SNR per scale height levels of the 1988 KAO and 2002 UH 2.2m light curve data. r_s was fixed to be that found from the 2006 Siding Spring best-fit of 1180±2 km. With r_s fixed, synthetic light curve tests show that reliable fits to the remaining parameters (p_s, γ_o, s_{fs}, s_s, and t_{min}) may still be obtained when considering only the top portions of the 1988 and 2002 data. Figures 4-10 and 4-11 show the normalized data, best-fit light curve, and residuals for 2002 UH 2.2m and 1988 KAO, respectively, for fits to data above the 0.4 normalized flux level. The residuals in this case do not show structure (but do increase in scatter as 0.4 normalized flux is reached in the 2002 UH 2.2m data).

With r_s fixed at the Siding Spring best-fit surface radius of 1180±2 km, fits were able to be performed to other datasets in Table 4.2 since synthetic light curve tests show reliable fits down to approximately 5 SNR per scale height for fits to only two parameters. The following datasets are free of apparent systematic errors and have background fraction calibrations available: 2002 Lick (Fig. B-4b), 2006 Black Springs (Fig. B-5c), 2006 Mt. Stromlo (Fig. B-6b), and 2008 IRTF (Fig. B-9b). The normalized data, best-fit light curve, and residuals for these light curves are shown in Figs. 4-12–4-15. The 2002 Lick light curve was fit above the 0.4 normalized flux level as was done with the 2002 UH 2.2m light curve.

4.3 Discussion

The least-squares fitting results are summarized in Table 4.3. The reported errors are for the formal least-squares fit, and do not include any other errors such as those from uncertainties in the position of each station in the shadow plane (i.e. closest approach distance) or those from the background fraction calibration, quantified below. The formal least-squares fits implicitly assume the radiative-conductive model is "exact" and propagates no uncertainties from the observationally determined half-light radius to the inference of the surface radius. The error bars on fits with r_s fixed do take into account the uncertainty in the value of r_s from the least-squares fit.

4.3.1 Surface radius

My surface radius determination of 1180±2 km is consistent with previously reported values. (The error bar here is from the least-squares fit and is quite small; other sources of error are discussed below.) Elliot et al. [2007] extrapolated their 12 June 2006 inversion temperatures until they reached the surface ice temperature and found a value of 1168±10 km for the surface radius. Upon considering other factors [including the Strobel et al. [1996] radiative-conductive model presented here], they believe their best estimate is 1152±32 km. My value is also consistent with mutual event estimates of 1173±23 km by Young and Binzel [1994].

I stress the importance of the dependence of the surface radius result and its error bar on the assumptions made in the model. One major assumption of the radiative-conductive model is the lack of a troposphere, the presence of which would probably modify the surface radius result. Also, the assumption of radiative equilibrium by definition does not include the effects of heat transport by atmospheric circulation. Otherwise temperature and refractivity are rather insensitive to the surface radius and depend more on the altitude above the surface. This can be understood in terms of the solar constant and the greenhouse effect. The solar constant, which determines the amount of heat input to the atmosphere, depends on the inverse square of the distance from the Sun. A change in the surface radius of tens of kilometers will not affect the value of the solar constant significantly, since the Sun's distance is of order 10^{10} km. The heating and cooling properties of the atmosphere are a function of optical depth, or how much "atmosphere" lies along the path of the light ray, dependent on altitude. Thus the surface radius result is more affected by assumptions about the occultation itself.

I found that for a 0.2% change in the background fraction, the fit result to the 2006 Siding Spring data for surface radius just barely agreed with the fit with unoffset background fraction. The calculated error bar on the 2006 Siding Spring background fraction is 0.05%, so errors in the background fraction are not likely to be a major source of additional error in the surface radius result. Likewise, a 10 km change in the distance of closest approach produced a fit result for surface radius that just barely agreed with the fit result with unoffset distance of closest approach. The calculated error on distance of closest approach is comparable to 10 km, and with this source of error, I revise the surface radius error bars upwards. The fit results for surface

pressure and CH_4 mixing ratio are much less affected by the errors in distance of closest approach.

Finally, I examined the residuals for the 2006 Siding Spring data with model curves that had the same parameters as the best-fit result, but with surface radius varied. The standard deviation of the residuals during the occultation differed by more than 10% as compared with the standard deviation of the residuals in the baseline for surface radii less than 1170 km and greater than 1200 km. This result implies that a wider range of surface radii are possible than indicated by the formal least-squares fit, and I conclude that the surface radii indicated by my model analysis is 1180^{+20}_{-10} km. The range of these error bars now roughly match the determination by Young and Binzel [1994], but the upper end is higher than that by Elliot et al. [2007]. Elliot et al. [2007] consider many factors in the surface radius they present, but the basis for their value is the result from the inversion temperature, which may contain systematic errors due to the boundary condition they assume [the Elliot and Young, 1992, model].

4.3.2 Surface pressure

The surface pressure fit results show an increasing trend with time (see Fig. 4-16), when less weight is given to the 2002 Lick result in light of its relatively large error bar. However the change between 1988 and 2002 is much smaller than the factor of two derived by Elliot et al. [2003b] and Sicardy et al. [2003]. Moreover a change between 2002 and 2006 exists in my results that was not observed by the analysis of Elliot et al. [2007]. A change between 2006 and 2008 is not distinguishable, in contrast to the 28% increase between 2006 and 2007 reported by Olkin et al. [2009]. Perhaps the surface pressure increased between 2006 and 2007 but then returned to its 2006 value between 2007 and 2008. My values agree with the lower limit of 6.5 μbar obtained by the stratosphere-only models of Lellouch et al. [2009]. However, these authors combine light curves from 2002 with CH_4 spectra from 2008, which leads to skepticism of their results in light of the apparent change in Pluto's atmosphere with time.

Depending on the tuning of the input parameters, the surface frost model of Hansen and Paige [1996] is able to produce a trend in surface pressure with time that qualitatively agrees with my fit results. This model includes the effect of orbital parameters (e.g. distance from the sun and latitude of the subsolar point) and of surface properties (e.g. surface thermal inertia and albedo) on the distribution of ice in time and space, which is directly related to the surface pressure as the surface and atmosphere are thought to be in vapor pressure equilibrium. The model of Hansen and Paige [1996] does not include any radiation from the atmosphere or atmospheric dynamics. Mars general circulation models (GCMs), which are similar to Pluto in that they have a condensible gas as their main atmospheric constituent and temperatures near the frost point, show a net flow of mass from the sublimating ice cap to the condensing one [e.g. Pollack et al., 1990]. This flow is of unknown importance on Pluto and could be important for the distribution of ice and hence surface pressure variations.

Hadley cells are ubiquitous in models of atmospheric circulation, and the latitude

of the rising and sinking branches are associated with regions of high and low surface pressure, respectively. The Mars GCM described in Section 2.3 shows that for most of the year, the Hadley circulation lies in a solstice configuration, namely a single cell that rises in the summer hemisphere and sinks in the winter hemisphere. During a short period near equinox, the circulation quickly passes through a transition to a two-cell configuration, with rising near the equator and sinking in at poleward latitudes, then reverts back to a solstice configuration (but in the opposite sense about the equator). Intuition suggests that a Pluto year-long experiment using a Pluto version of this GCM (see Chapter 5) would also behave in the same way[1] (at present such a run is computationally too expensive). Pluto was near equinox during the 1988 observation and by the 2008 observation might have had sufficient time to transition into a solstice circulation. A comprehensive picture of any atmospheric dynamics has yet to be published for Pluto.

4.3.3 CH_4 mixing ratio

The values for γ_o in Table 4.3 do not all agree with each other, nor do they show a monotonically increasing or decreasing trend with time (see Fig. 4-17), contrary to the conclusion by Lellouch et al. [2009] that the CH_4 mixing ratio is decreasing with time. Model sensitivity tests presented in §4.1.3 showed that above $\gamma_o \approx 6 \times 10^{-3}$ the model light curve becomes significantly less sensitive to variations in γ_o. This is further evidenced by the fact that the formal error bars on the least-squares fit are larger for larger values of γ_o. My results for γ_o show that it is in the range of 1.8 to 17.8×10^{-3}, which overlaps with $7.2^{+18.9}_{-5.2} \times 10^{-3}$ (here assuming a 10 μbar surface pressure) found by Young et al. [1997] and $(5 \pm 1) \times 10^{-3}$ found by Lellouch et al. [2009]. The lack of any obvious pattern in the variation of γ_o in my results suggests that the distribution of CH_4 in Pluto's atmosphere is highly variable temporally or spatially, or a combination of both. It is interesting to note that the 2006 chords were geographically aligned in the shadow plane as Mt. Stromlo, Black Springs, Siding Spring, and the results show an increase in γ_o from Mt. Stromlo to Black Springs. An increase in γ_o from Black Springs to Siding Spring is consistent with the results within the error bars; however the large Siding Spring error bar does not allow us to rule out other explanations. The complexities associated with the balance between gaseous and solid methane, their distribution relative to other constituents on the surface and in the atmosphere, and their transport are not processes that are included in the model.

The radiative-conductive model used in our analysis is in radiative equilibrium, which by definition does not include the transport of heat by wind. In general advection of temperature by the wind causes the true atmospheric temperature to depart from radiative equilibrium. It is possible that deviations from radiative equilibrium

[1] Dima and Wallace [2003] show in terrestrial data (the only planet for which we have sufficient wind data to compute the mass stream function) that global circulation does not lie in a solstice configuration for as long a period as suggested by idealized models [e.g. Lindzen and Hou, 1988]. Comparison with Earth, however, is problematic because of the strong influence of Earth's oceans on the atmosphere.

are being incorrectly attributed to changes in CH_4 mixing ratio (or surface pressure). Including the effects of atmospheric dynamics (for instance using a GCM) is the subject of future work (also see Chapter 5)

4.3.4 Temperature results

Model temperature profiles corresponding to the best-fit light curves with the highest SNR per scale height (i.e. 2006 Siding Spring, 2002 UH 2.2m, and 1988 KAO) are plotted in Fig. 4-18. The gray shaded areas correspond to the range of the formal error from the least-squares fit. As demonstrated in §4.1.3, the light curve is not sensitive to CO mixing ratio, but the temperature structure is. Thus, additional error (not shown) is present in the temperature profile from uncertainty in CO cooling. Any effect on the temperature profile will follow the form shown in the upper right panel of Fig. 4-8, with the strength of the effect corresponding to the difference between the true CO mixing ratio and my assumption. The 1988 KAO model temperature profile (bottom panel of Fig. 4-18) is the coolest above 1200 km radius, due to its lower p_s and γ_o. While the UH 2.2m best-fit results have a lower p_s than 2006 Siding Spring, its relatively large γ_o causes the model temperature profile to be warmer than 2006 Siding Spring.

Young et al. [2008a] derive a temperature of 103.9±3.2 K at 1275 km from independently obtained data not listed in Table 4.2 for the 2006 occultation. This value is lower than my model value of 112±6, 123^{+3}_{-14}, and 125^{+1}_{-3} K at this radius for the 2006 Black Springs, Mt. Stromlo, and Siding Spring occultations, respectively.

The vertical temperature gradients in the model profiles corresponding to the best-fit light curves with the highest SNR per scale height are at their maximum at the surface and have values of 8.4, 12.6, and 11.4 K km^{-1} for 1988 KAO, 2002 UH 2.2m, and 2006 Siding Spring, respectively. Even though the light curve data does not reach all the way down to the surface (and in the case of 1988 and 2002 fits is truncated well above the surface), model values near the surface are still constrained because the entire atmospheric column must be in radiation balance. My temperature gradients agree with the range of 3–15 K km^{-1} concluded by Lellouch et al. [2009] using 2002 light curve data.

4.3.5 Half-light radius and temperature

Also shown in Table 4.3 are the half-light radius r_H and half-light temperature T_H (the model temperature evaluated at r_H) for comparison with previous fits that used the model of Elliot and Young [1992]. The errors on T(r_H) are directly due to the formal errors from least-squares fit and don't incorporate the errors on r_H. Note that it is the half-light radius that is robustly determined by the Elliot and Young [1992] model, and variations (or lack thereof) in time of the half-light radius are what led to the inference of changing (or unchanging) surface pressure by Elliot et al. [2003b], Elliot et al. [2007], Person et al. [2008], and Young et al. [2008a].

Elliot et al. [2007] used the Elliot and Young [1992] model to perform simultaneous fits on all of the light curves in each year for the 1988, 2002, and 2006 events listed in

Table 4.2. Their values for r_H for 1988, 2002, and 2006, respectively were 1233 ± 4, 1279 ± 5, and 1276 ± 4 km. My r_H values are higher than these results for 1988, lower for 2002, and about equal for 2006. Moreover my r_H values show an increase with time directly related to the increase in surface pressure. Elliot et al. [2007] model fits results for T_H were 114 ± 10, 108 ± 9, and 97 ± 5 K for the events of 1988, 2002, and 2006, respectively. My values are about equal in 1988 and higher than Elliot et al. [2007] in 2002 (if greater weight is given to the lower error bars on the UH 2.2m derived value) and 2006 and do not show a trend with time as theirs do. Young et al. [2008a] derive from their 2006 data a half-light *shadow* radius of 1216±8.6 km, which is higher than my values of 1206^{+7}_{-5}, 1198^{+7}_{-2}, and 1200±3 km for the 2006 Black Springs, Mt. Stromlo, and Siding Spring occultations, respectively.

I believe my temperature determinations to be more accurate than the values reported by other authors above, which assume that the temperature profile follows a power law as $T = T_H(r/r_H)^b$ or some other idealized shape. Such a representation of the atmosphere is rather idealized and may not describe a planetary atmosphere accurately. My atmospheric model makes a temperature prediction based on physical considerations of the chemical species causing heating and cooling specific to Pluto's atmosphere.

It is apparent from Table 4.3 that our temperature results, at least for T_H do not unanimously agree for a particular year, nor is a clear trend apparent from year to year. As in discussed in Section 4.3.3 regarding the CH_4 mixing ratio results, spatial variations may be present. The spatial variations may be a direct result of the spatial variations in CH_4 mixing ratio, or may be associated with heat transport by atmospheric circulation. The effects of the atmospheric circulation on temperature will be assessed in future work with a general circulation model (also see Chapter 5).

4.4 Conclusions

I have used the radiative-conductive model of Strobel et al. [1996] to least-squares fit Pluto stellar occultation data from the years 1988, 2002, 2006, and 2008. This model predicts atmospheric temperature as a function of surface temperature, pressure, and radius and CH_4 and CO mixing ratios. This model uses a state of the art radiative transfer scheme to compute model light curves. This scheme improves upon previous methods for analyzing Pluto light curves, many of which make a general assumption that the temperature follows a power law with height or some other idealized behavior, by including the effects of heating and cooling by gases that (presumably) exist in Pluto's atmosphere. I found that the light curves are most sensitive to surface pressure and radius and CH_4 mixing ratio, although a high SNR per scale height is required to fit all three parameters. For the 2006 Siding Spring data, I was able to make a surface radius determination of 1180^{+20}_{-10} km; this surface radius estimate is likely to be affected by the assumption of a stratosphere only model. The CH_4 mixing ratio was calculated to be 1.8 to 17.8×10^{-3} and does not show a monotonically increasing or decreasing trend with time. I found that the surface pressure was increasing with time, but that the increase is not as substantial as indicated by others.

A new development to the radiative-conductive model is the option of a troposphere, where the effects of vertical transport by eddy mixing and moist convection (due to CH_4 condensation) are included. Appending a troposphere to the bottom of the stratosphere not only modifies the temperature at the lowest altitudes, but affects the entire temperature profile as well. In turn a different temperature profile may yield different fit results for surface radius, surface pressure, and CH_4 mixing ratio. Previous studies [Stansberry et al., 1994; Lellouch et al., 2009] have investigated the possibility of a troposphere, but at present the data is still ambiguous with regard to its presence and depth. Model fits using the troposphere feature in the Strobel et al. [1996] model are the subject of future study.

I have made the assumption that the light curve is symmetric about some time t_{min}, which is a free parameter in my least-squares fits. This assumption is equivalent to assuming that the part of the atmosphere probed by immersion has the same properties (e.g. p_s or γ_o) as the part of the atmosphere probed by emersion. Because of Pluto's high obliquity with respect to the ecliptic, the immersion part of the atmosphere tends to lie in the southern hemisphere (using the IAU convention), while the emersion part lies in the northern hemisphere. Light curve fits that treat the immersion and emersion portions of the atmosphere separately will be attempted in future work.

The temperature profiles from the radiative-conductive model are in radiative equilibrium, which means they do not incorporate any heat transport by dynamical processes in the atmosphere. Such dynamical processes not only cause the temperature to depart from radiative equilibrium, but create seasonal and latitudinal variations in surface pressure that arise from the Hadley circulation. Moreover, the temperature may be affected by the presence or absence of underlying surface ice, and the surface pressure affected by condensation and sublimation of ice. To add all of these effects to the temperature profile, a GCM could be thermally forced using the radiative-conductive model with a surface frost package included. Numerous GCM studies with an atmosphere whose primary constituent exchanges mass with the surface have already been explored for Mars [e.g. Hourdin et al., 1995]. GCM runs could be performed under a number of different values for T_s, p_s, γ_o, η, and r_s so that light curves could be calculated from the resulting temperatures and compared to observations.

Table 4.1: Summary of test cases

Case	T_s (K)	p_s (μbar)	γ_o (10^{-3})	η (10^{-4})	r_s (km)
control	37	18	6	5	1152
1 (ΔT_s)	42	18	6	5	1152
2 (Δp_s)	37	9	6	5	1152
3 ($\Delta \gamma_o$)	37	18	2	5	1152
4 ($\Delta \eta$)	37	18	6	200	1152
5 (Δr_s)	37	18	6	5	1180

Table 4.2: Occultation data

Date	Station	SNR[a]	Reference	Figure
9 Jun 1988	**KAO**	**118**	**Elliot et al. [1989]**	**B-1a**
9 Jun 1988	Charters Towers immersion	73	Millis et al. [1993]	B-1b
9 Jun 1988	Charters Towers emersion	74	Millis et al. [1993]	B-1c
9 Jun 1988	Aukland	46	Millis et al. [1993]	B-2a
9 Jun 1988	Black Birch	47	Millis et al. [1993]	B-2b
9 Jun 1988	Toowoomba	15	Millis et al. [1993]	B-2c
9 Jun 1988	Mt. John	24	Millis et al. [1993]	B-3a
9 Jun 1988	Mt. Tambourine	13	Millis et al. [1993]	B-3b
9 Jun 1988	Hobart	51	Millis et al. [1993]	B-3c
21 Aug 2002	**UH 2.2m[b]**	**159**	**Elliot et al. [2003b]**	**B-4a**
21 Aug 2002	**Lick**	**16**	**Elliot et al. [2003b]**	**B-4b**
21 Aug 2002	Palomar	5	Elliot et al. [2003b]	B-4c
21 Aug 2002	Maui	74	Elliot et al. [2003b]	B-5a
21 Aug 2002	Lowell	6	Elliot et al. [2003b]	B-5b
12 Jun 2006	**Black Springs**	**47**	**Elliot et al. [2007]**	**B-5c**
12 Jun 2006	Hobart	33	Elliot et al. [2007]	B-6a
12 Jun 2006	**Mt. Stromlo**	**29**	**Elliot et al. [2007]**	**B-6b**
12 Jun 2006	**Siding Spring**	**96**	**Elliot et al. [2007]**	**B-6c**
12 Jun 2006	Stockport	14	Elliot et al. [2007]	B-7a
18 Mar 2007	Fremont Peak	8	Person et al. [2008]	B-7b
18 Mar 2007	MMT[c] (IR)	490	Person et al. [2008]	B-7c
18 Mar 2007	MMT[c] (visible)	336	Person et al. [2008]	B-8a
18 Mar 2007	MRO[d]	45	Person et al. [2008]	B-8b
18 Mar 2007	USNO[e]	70	Person et al. [2008]	B-8c
18 Mar 2007	LBTO[f]	88	Person et al. [2008]	B-9a
24 Jun 2008	**IRTF[g]**	**29**	**Gulbis et al. [2010]**	**B-9b**

[a]SNR is the signal-to-noise ratio for one scale height in Pluto's atmosphere, assumed to be 60 km.

[b]University of Hawaii 2.2m telescope at Mauna Kea Observatory

[c]Multiple Mirror Telescope Observatory

[d]Magdalena Ridge Observatory

[e]United States Naval Observatory, Flagstaff Station

[f]Large Binocular Telescope Observatory

[g]Infrared Telescope Facility at Mauna Kea Observatory

Table 4.3: Least-squares fit results of atmospheric model to occultation data

Year	Station	$p_s(\mu\text{bar})$	$\gamma_o(10^{-3})$	r_s (km)	r_H (km)	T_H (K)
1988	KAO	9.2±0.6	$5.1^{+1.7}_{-1.1}$	fixed	1255±3	117±3
2002	UH 2.2m	$10.9^{+0.6}_{-0.7}$	$17.8^{+21.9}_{-10.3}$	fixed	1263^{+4}_{-3}	127^{+2}_{-5}
2002	Lick	$8.1^{+5.2}_{-1.2}$	$1.8^{+1.0}_{-1.3}$	fixed	1261^{+17}_{-6}	92^{+17}_{-24}
2006	Black Springs	$12.1^{+1.1}_{-0.8}$	$2.7^{+1.3}_{-0.7}$	fixed	1271^{+3}_{-4}	112±6
2006	Mt. Stromlo	12.1±1.1	$8.5^{+7.6}_{-6.0}$	fixed	1269^{+5}_{-7}	124^{+3}_{-14}
2006	Siding Spring	13.2±0.4	9.4±2.7	1180 ± 2	1274±3	124^{+1}_{-3}
2008	IRTF	$11.6^{+1.5}_{-1.4}$	$6.9^{+6.2}_{-5.4}$	fixed	1268^{+6}_{-12}	122^{+4}_{-26}

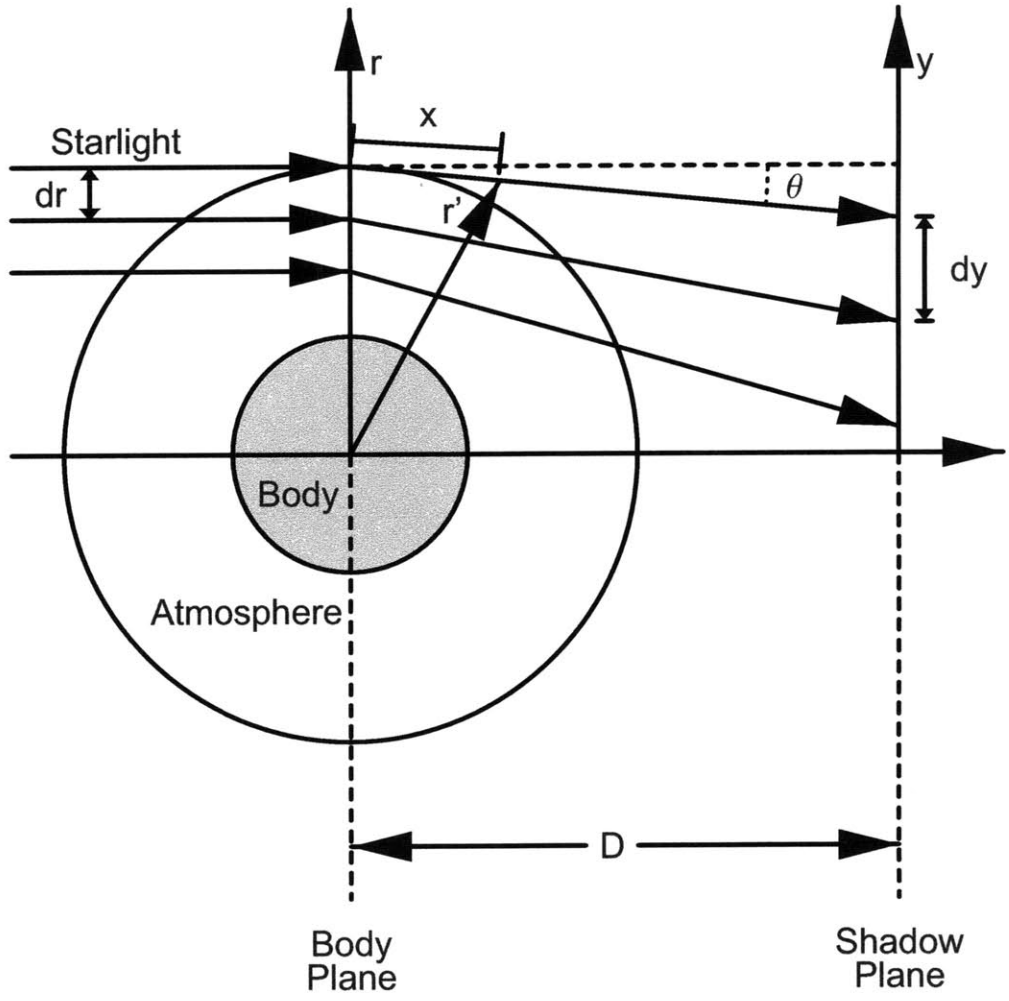

Figure 4-1: Diagram of occultation variables [adapted from Elliot et al., 2003a; Zalucha et al., 2007]. Starlight enters the body's atmosphere, is refracted in the body plane, and reaches the observer in the shadow plane. r is the radial distance from the body's center, y is the distance from the center of the shadow plane, θ is the refraction angle, x is the distance along the ray path measured from the point of closest approach, r' is the radial distance from the body's center along the ray path, and D is the distance between the body plane and shadow plane.

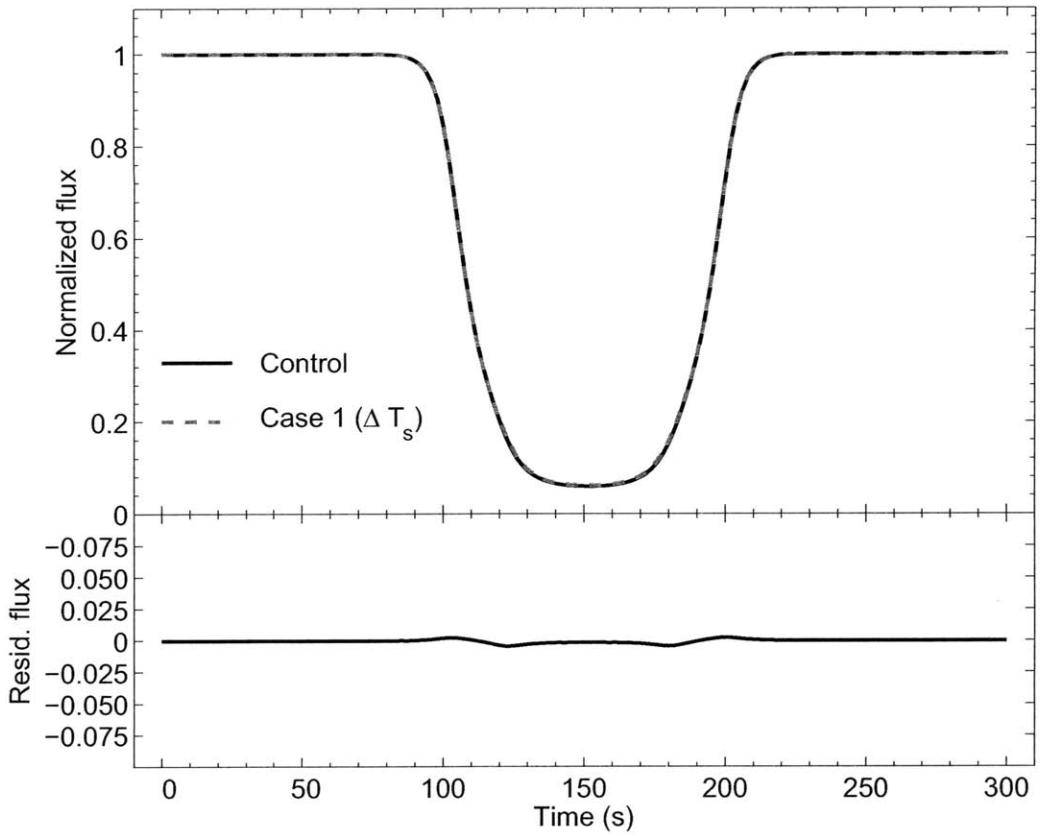

Figure 4-2: Normalized light curve flux vs. time for test case 1 and control. Below the light curve the corresponding residual flux is also shown. The geometry corresponds to that of the 12 June 2006 occultation observed at Siding Spring, and the time scale has been set to zero at an arbitrary point before the start of the occultation. The difference between the test case and the control light curve is so slight for this case that it is not discernible in the normalized flux plot.

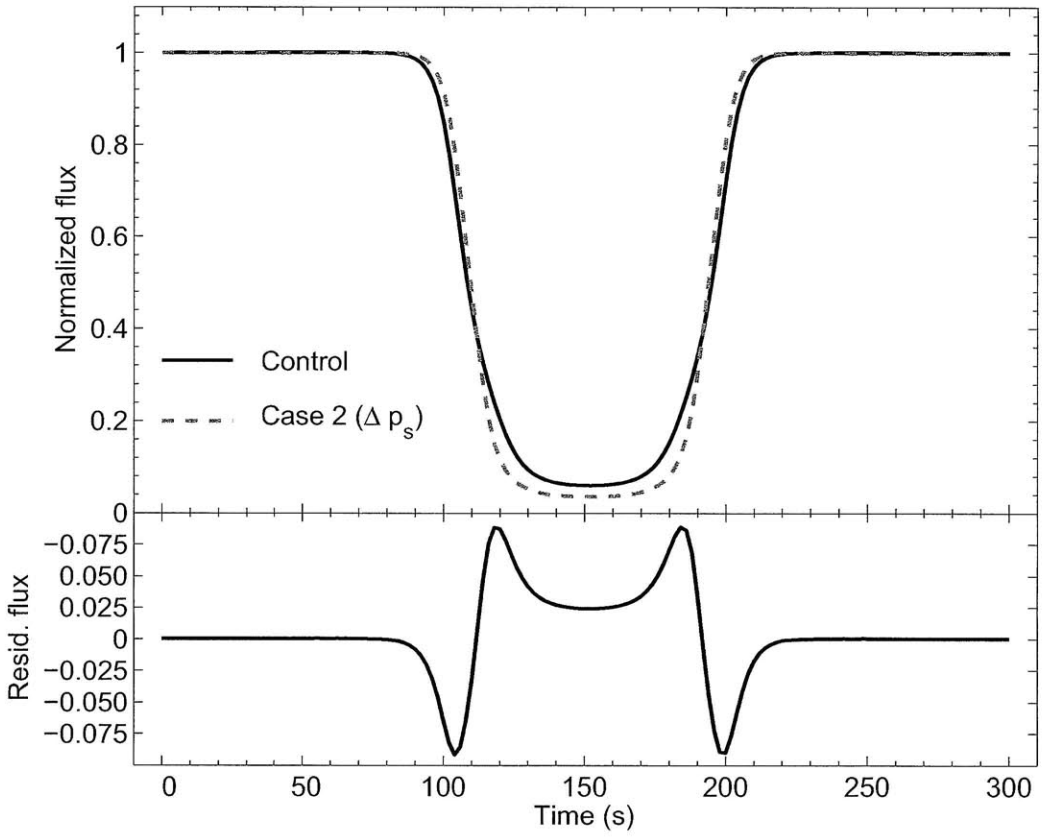

Figure 4-3: Normalized light curve flux vs. time for test case 2 and control. Below the light curve the corresponding residual flux is also shown. The geometry corresponds to that of the 12 June 2006 occultation observed at Siding Spring, and the time scale has been set to zero at an arbitrary point before the start of the occultation.

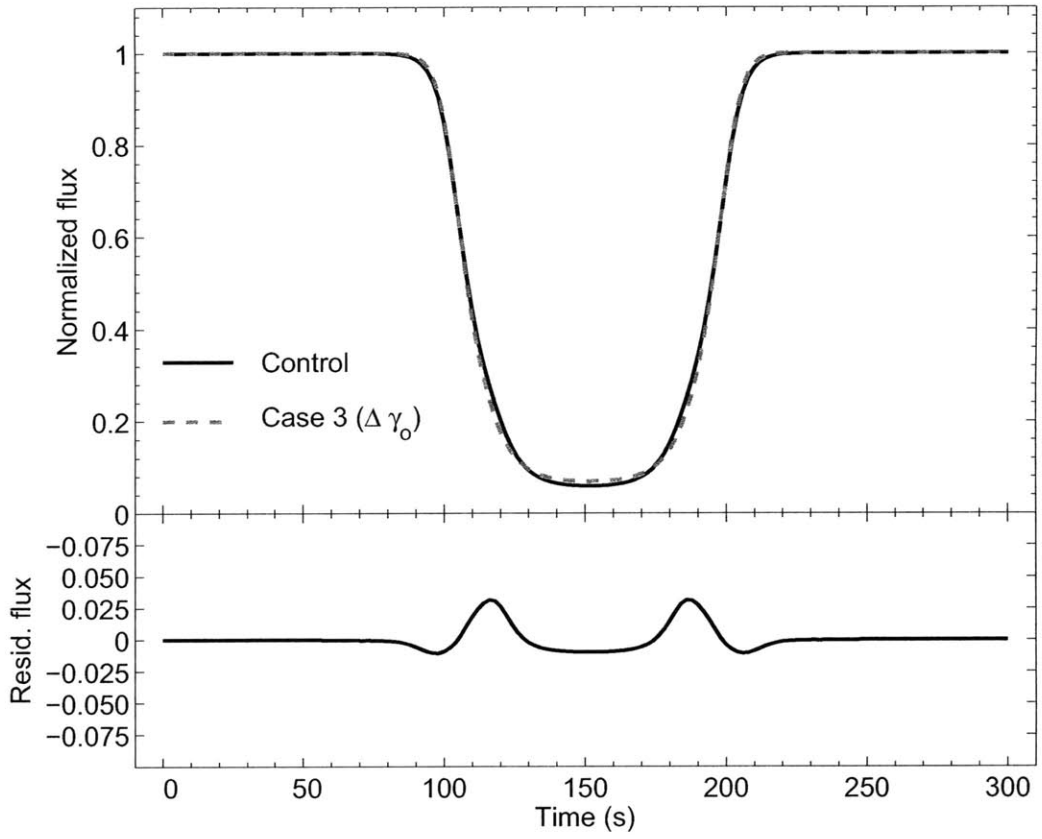

Figure 4-4: Normalized light curve flux vs. time for test case 3 and control. Below the light curve the corresponding residual flux is also shown. The geometry corresponds to that of the 12 June 2006 occultation observed at Siding Spring, and the time scale has been set to zero at an arbitrary point before the start of the occultation. Due to the nonlinear dependence of the light curve on γ_o, the variations between higher values of γ_o do not show such large magnitudes in the residual (e.g. the residual between $\gamma_o = 12$ and 16×10^{-3} is much smaller than the range of 2 and 6×10^{-3} shown here).

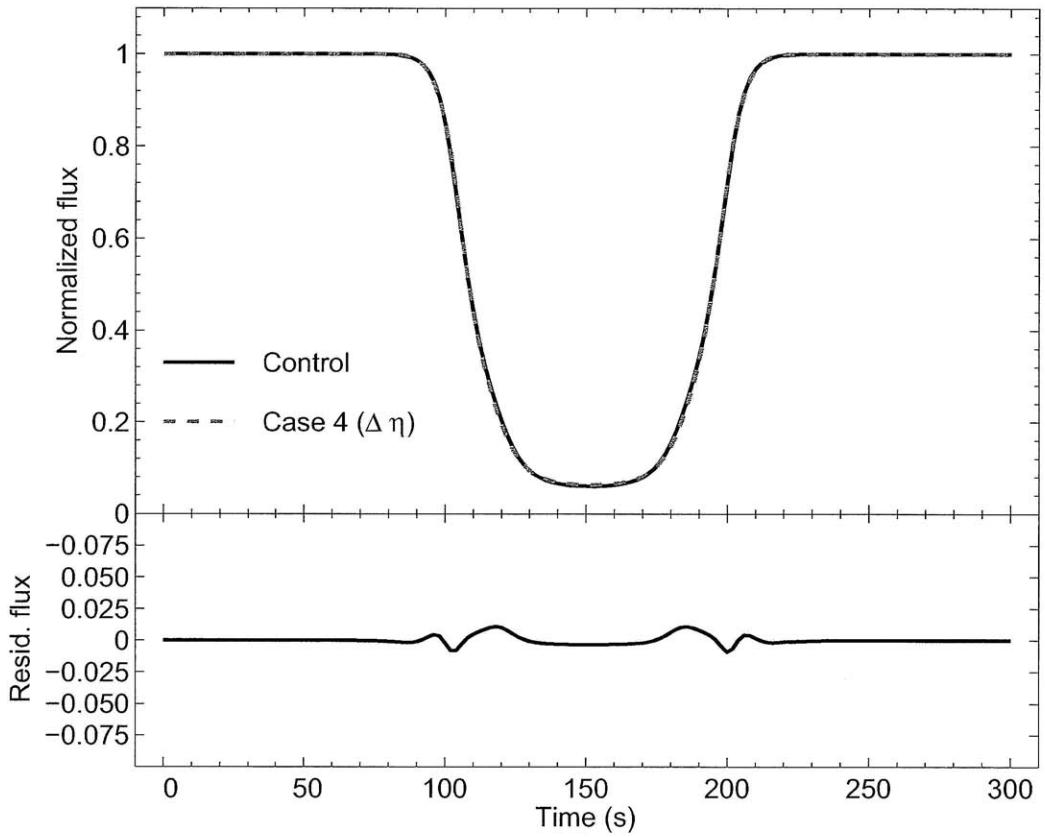

Figure 4-5: Normalized light curve flux vs. time for test case 4 and control. Below the light curve the corresponding residual flux is also shown. The geometry corresponds to that of the 12 June 2006 occultation observed at Siding Spring, and the time scale has been set to zero at an arbitrary point before the start of the occultation. The difference between the test case and the control light curve is so slight for this case that it is not discernible in the normalized flux plot.

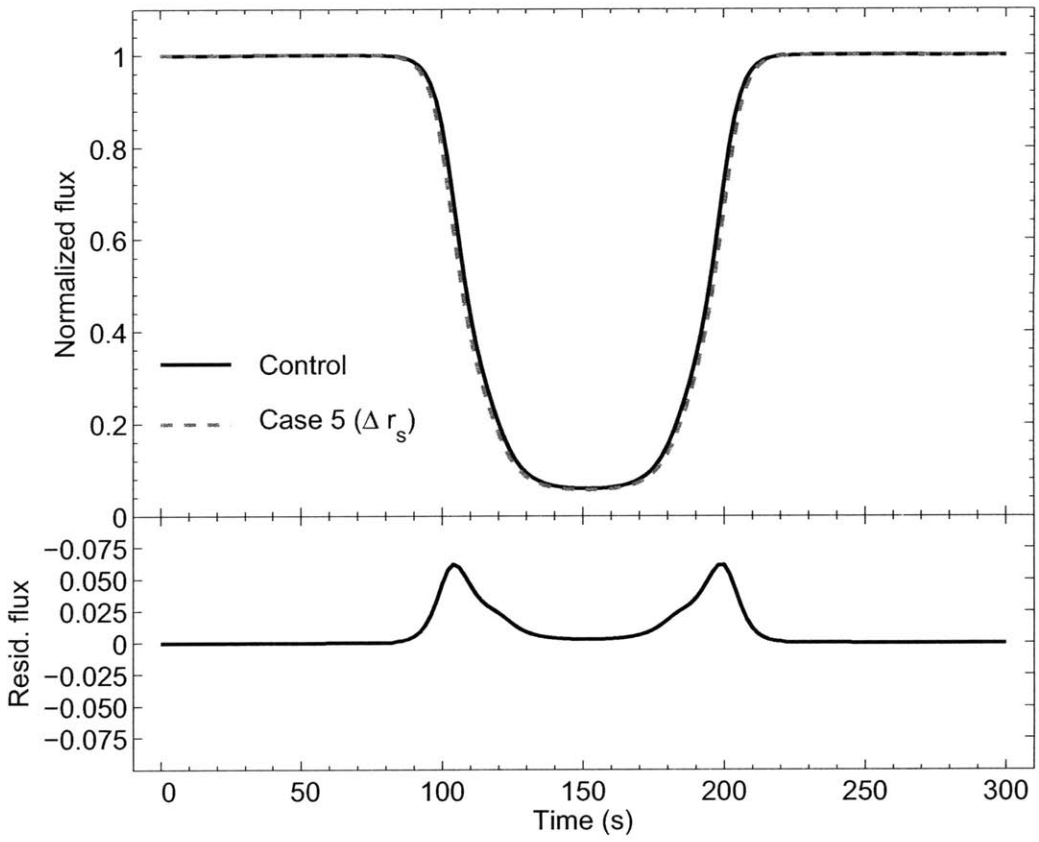

Figure 4-6: Normalized light curve flux vs. time for test case 5 and control. Below the light curve the corresponding residual flux is also shown. The geometry corresponds to that of the 12 June 2006 occultation observed at Siding Spring, and the time scale has been set to zero at an arbitrary point before the start of the occultation.

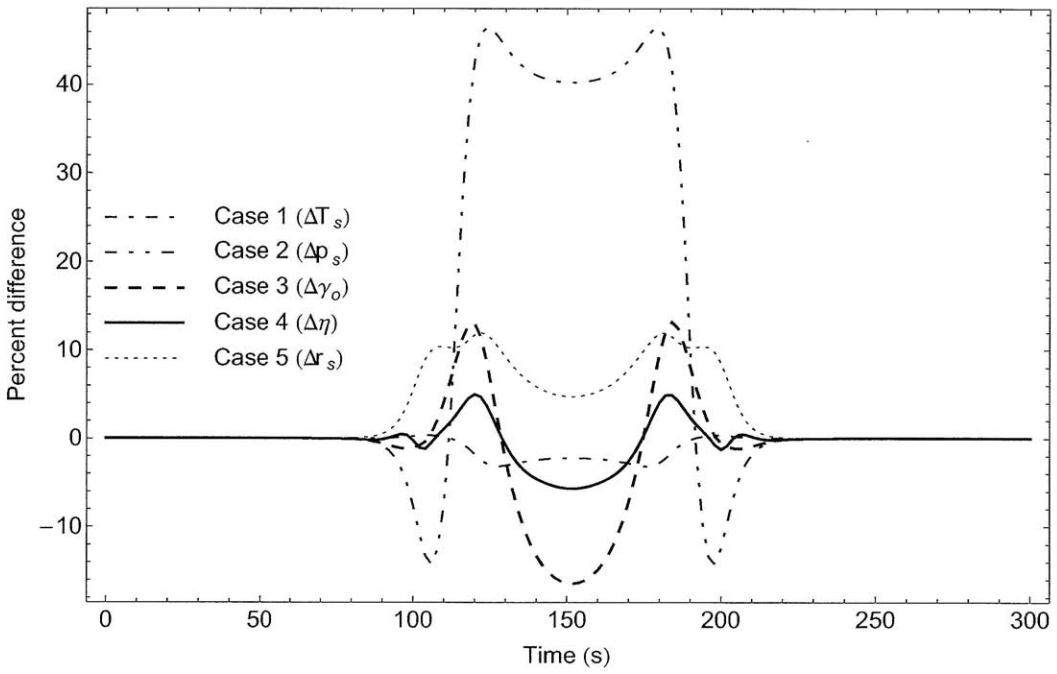

Figure 4-7: Percent difference between the the control and test case light curves. The primary difference in the light curve is from Δp_s (case 2), followed by $\Delta\gamma_o$ (case 3) and Δr_s (case 5), then ΔT_s (case 1) and $\Delta\eta$ (case 4).

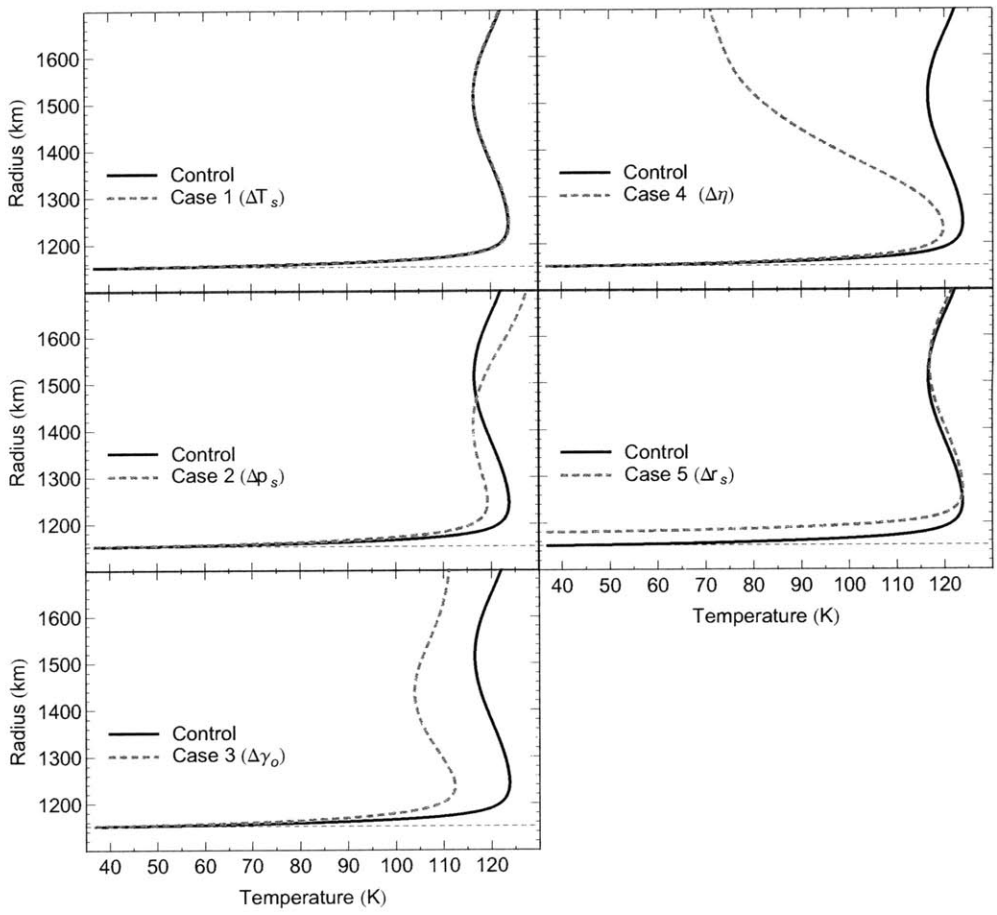

Figure 4-8: Temperature profiles corresponding to test cases and control. A change in T_s produces slight changes in both the light curve and the temperature profile. Changes in p_s or γ_o are discernible in both the light curve and the temperature profile. A change in η produces large temperature changes, especially at high radii, but a relatively minor effect on the light curve. A change in r_s shifts the temperature profile vertically but otherwise does not affect the magnitude.

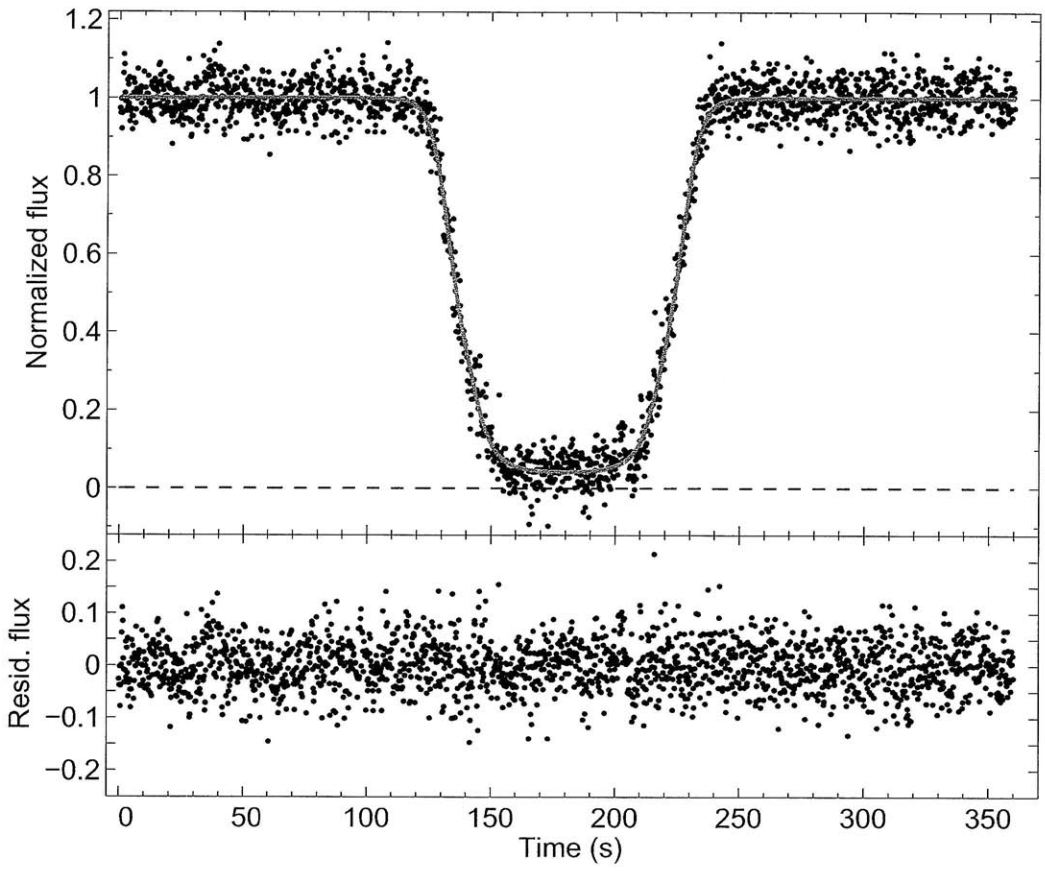

Figure 4-9: Observed light curves (black points) and best-fit light curves (gray line) for the 2006 Siding Spring occultation. The dashed line marks the level of zero normalized flux. The time scale has been set to zero at the start of the dataset.

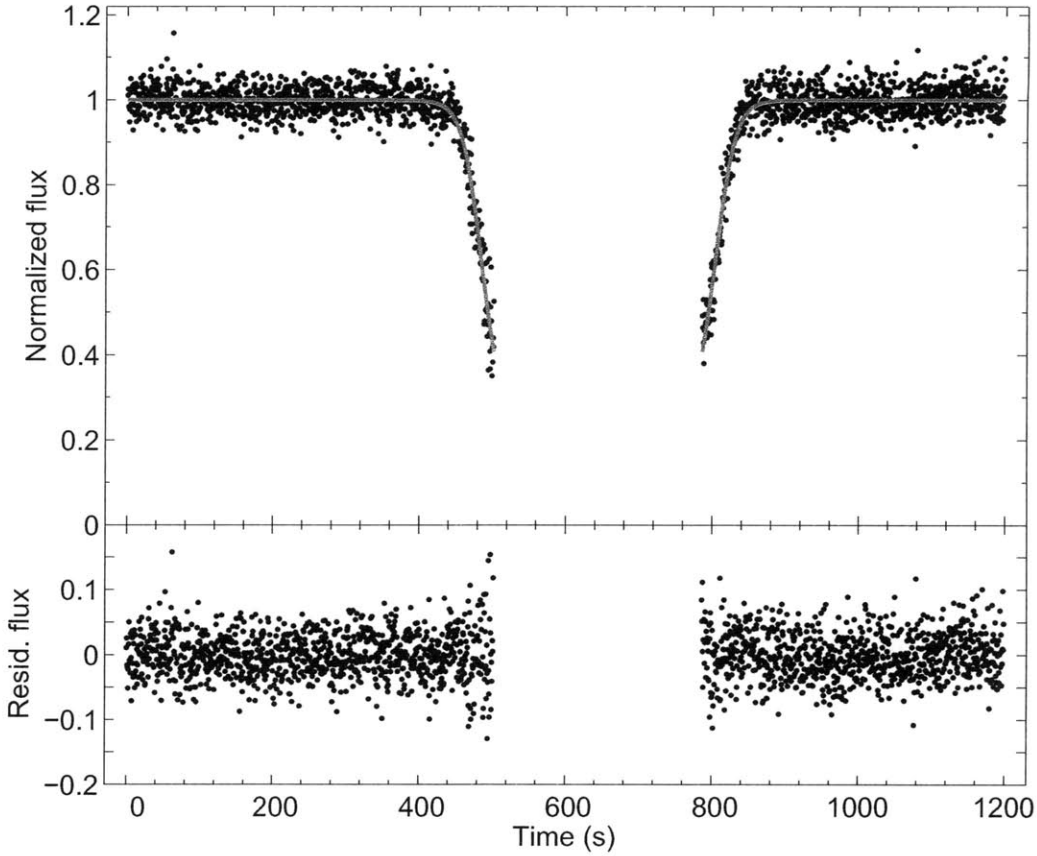

Figure 4-10: Observed light curves (black points) and best-fit light curves (gray line) for the 2002 UH 2.2m occultation. Only data that was used in the least-squares fit is plotted. The time scale has been set to zero at the start of the dataset.

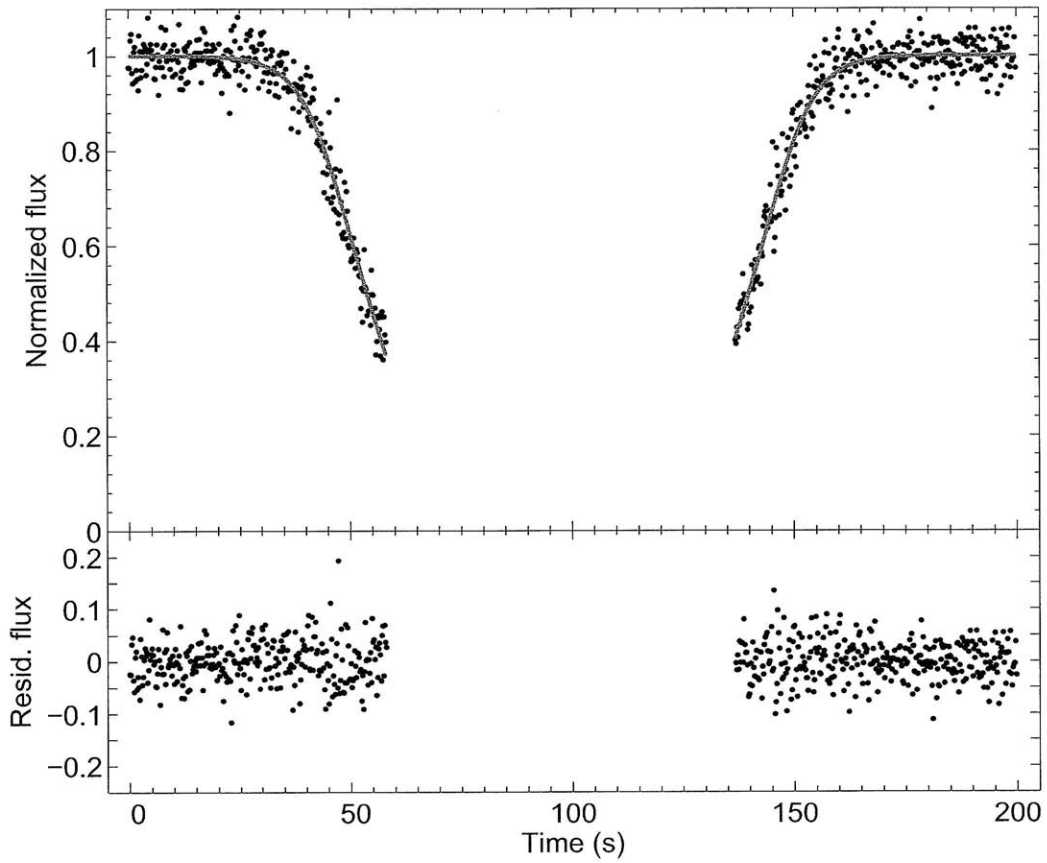

Figure 4-11: Observed light curves (black points) and best-fit light curves (gray line) for the 1988 KAO occultation. Only data that was used in the least-squares fit is plotted. The time scale has been set to zero at the start of the dataset.

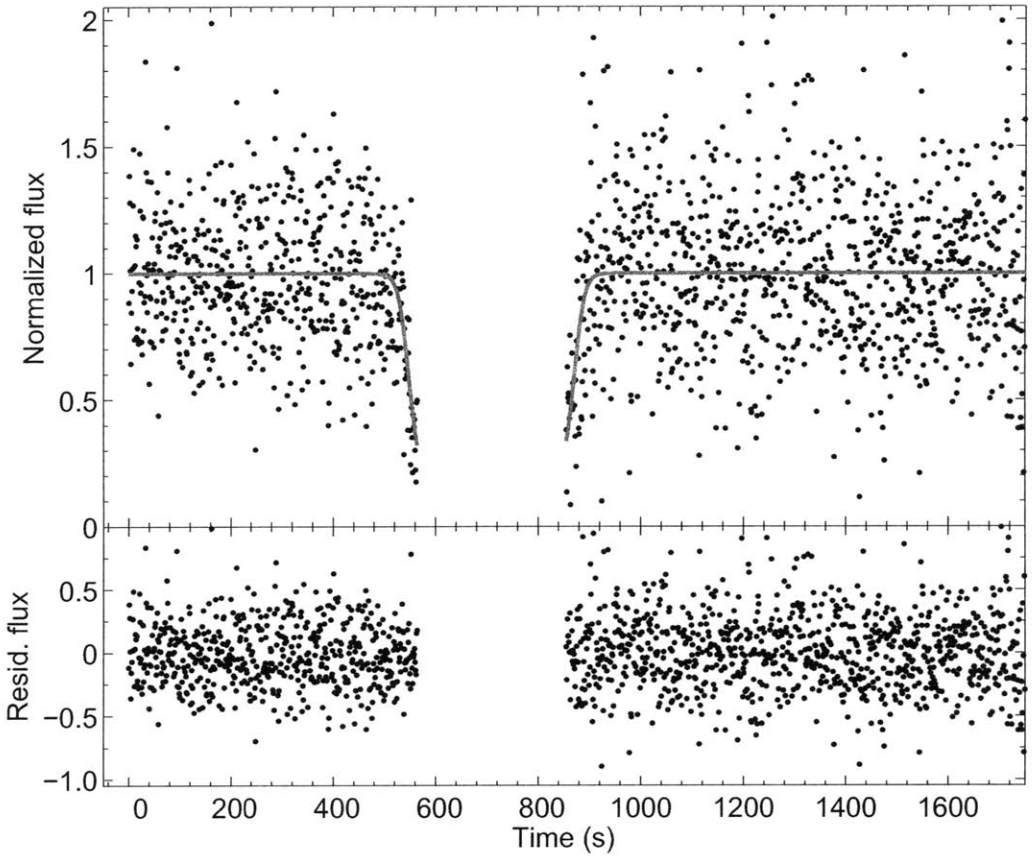

Figure 4-12: Observed light curves (black points) and best-fit light curves (gray line) for the 2002 Lick occultation. Only data that was used in the least-squares fit is plotted. The time scale has been set to zero at the start of the dataset.

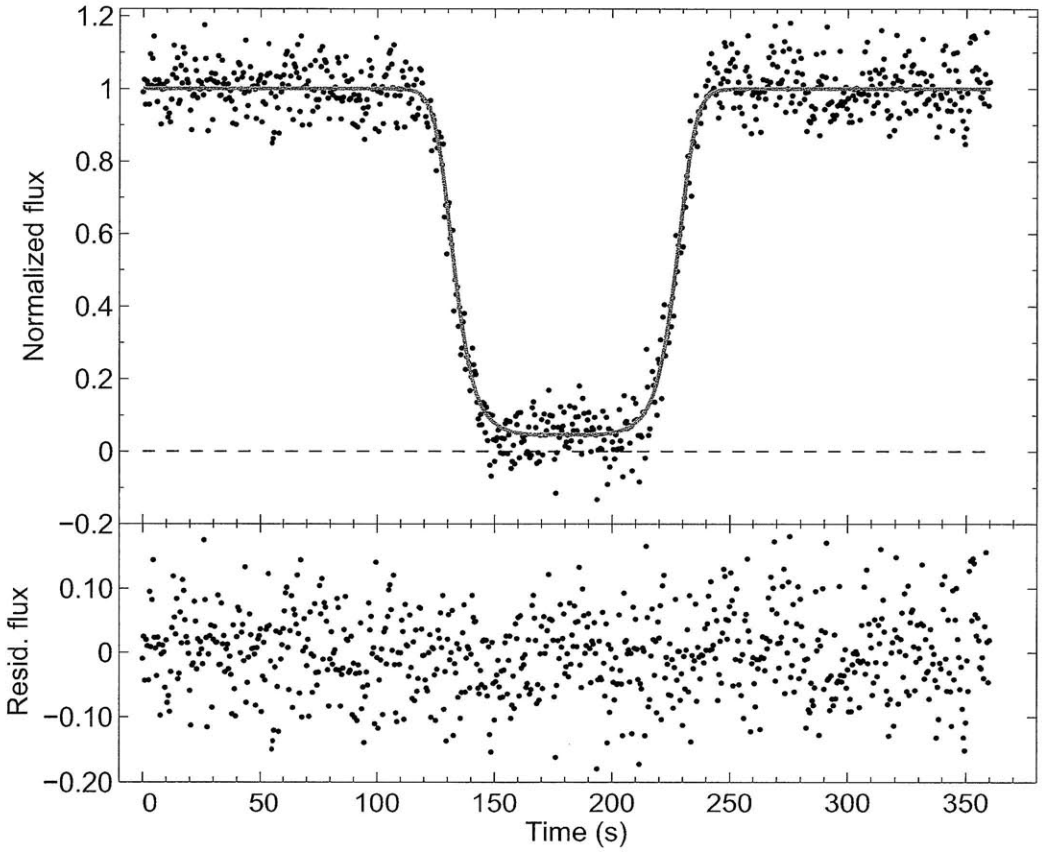

Figure 4-13: Observed light curves (black points) and best-fit light curves (gray line) for the 2006 Black Springs occultation. The dashed line marks the level of zero normalized flux. The time scale has been set to zero at the start of the dataset.

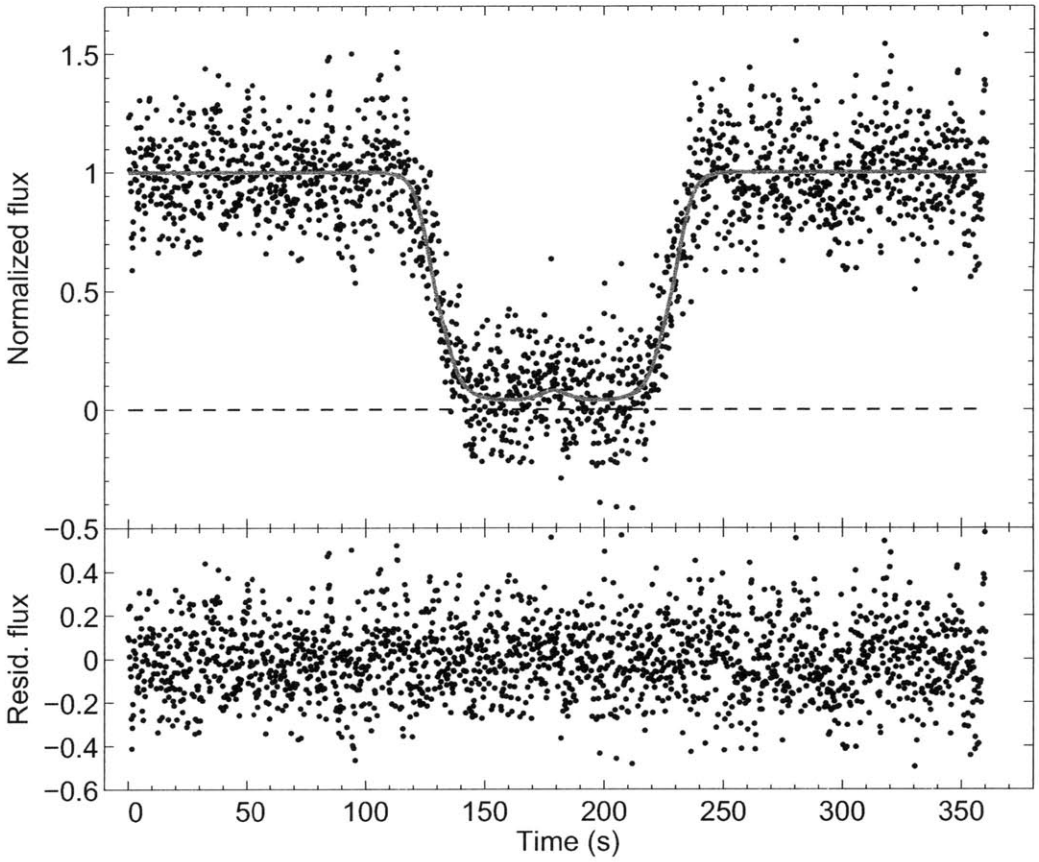

Figure 4-14: Observed light curves (black points) and best-fit light curves (gray line) for the 2006 Mt. Stromlo occultation. The dashed line marks the level of zero normalized flux. The time scale has been set to zero at the start of the dataset.

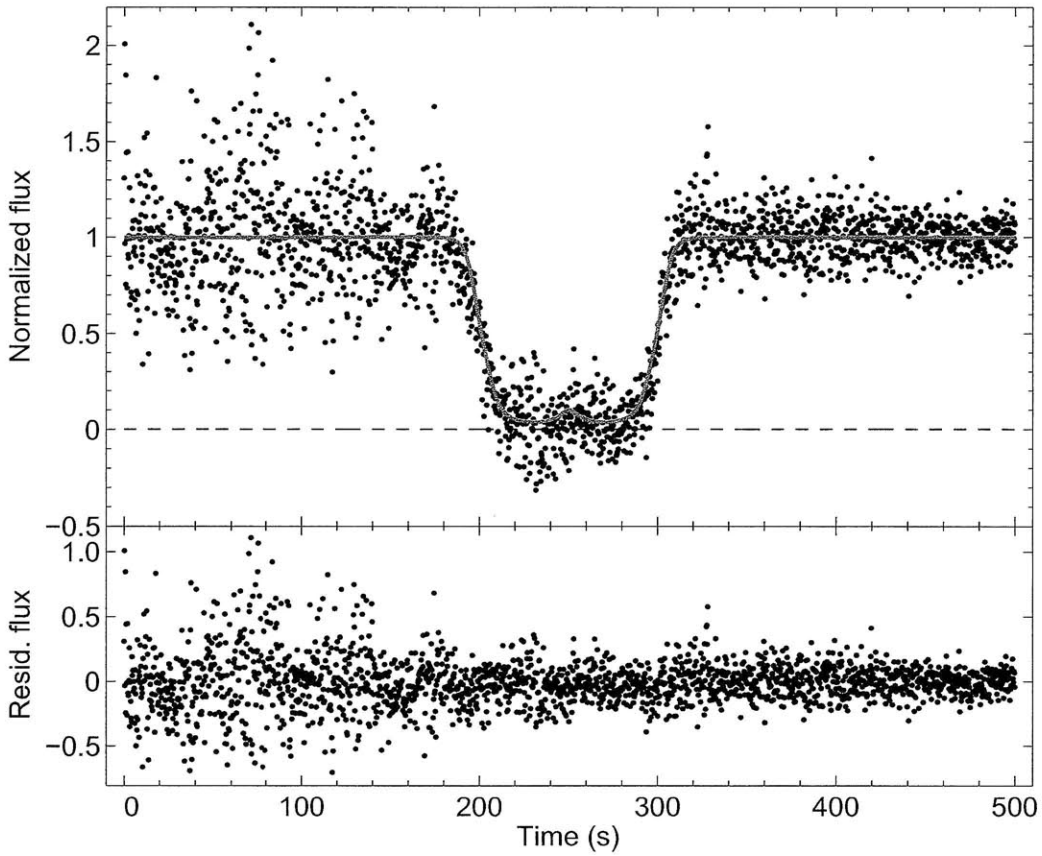

Figure 4-15: Observed light curves (black points) and best-fit light curves (gray line) for the 2008 IRTF occultation. The dashed line marks the level of zero normalized flux. The time scale has been set to zero at the start of the dataset.

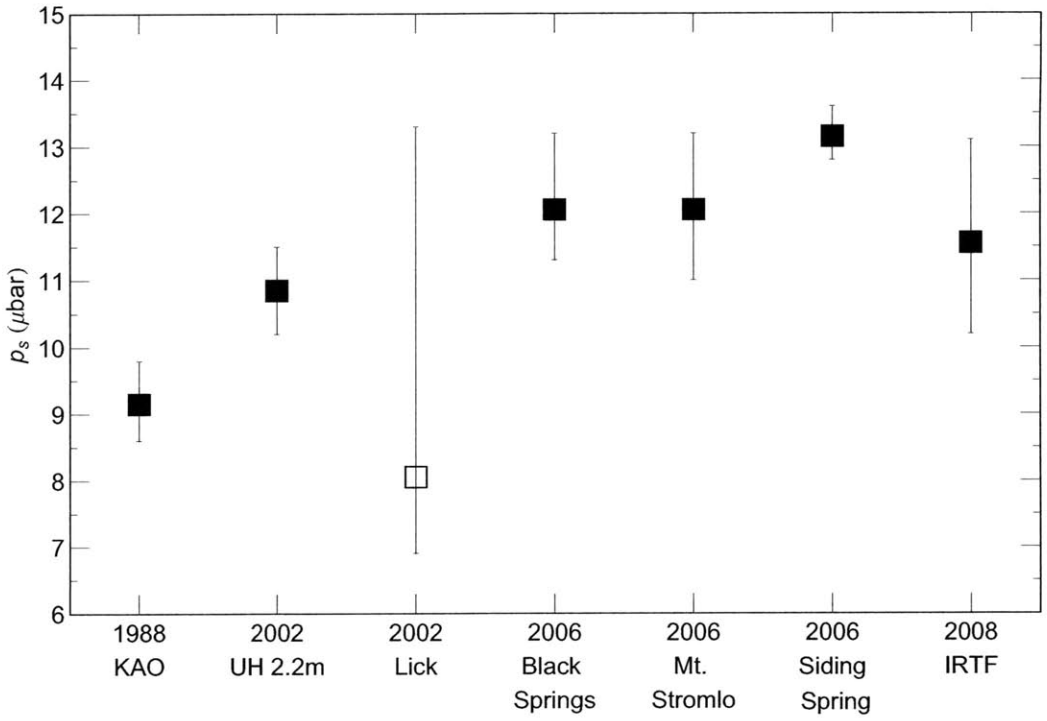

Figure 4-16: Fit results for p_s vs. year. The 2002 Lick data is plotted with a white box to indicate that less weight should be given to this measurement, since its error bars are of much greater magnitude than the other measurements. An increasing trend with time can be seen from 1988 to 2006, then a steady trend from 2006 to 2008.

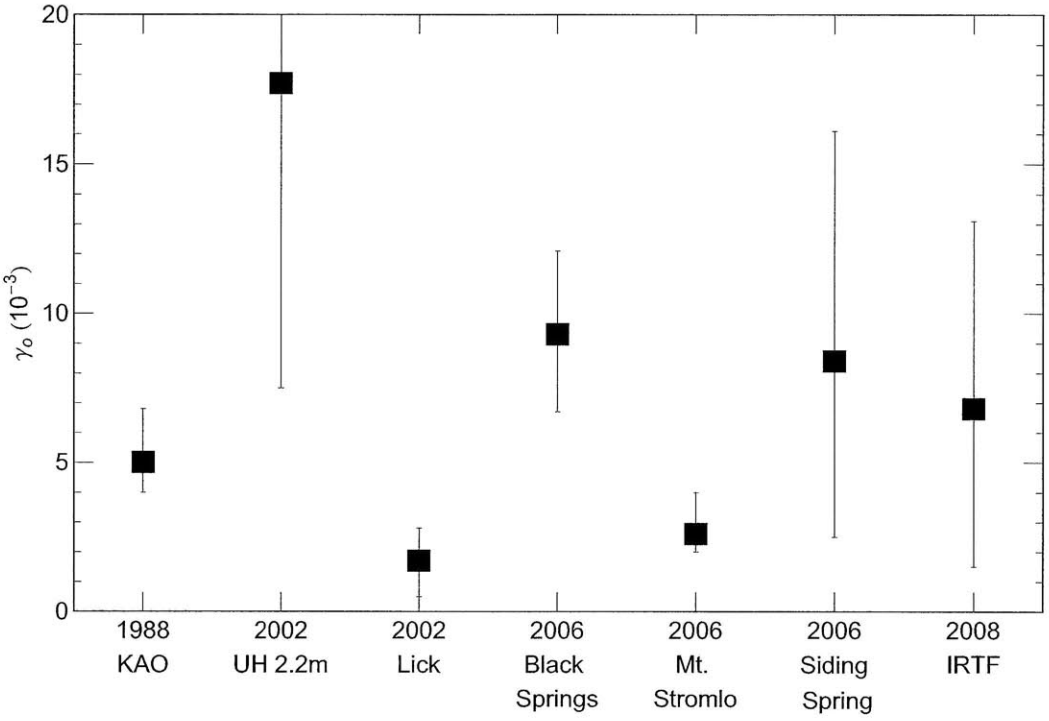

Figure 4-17: Fit results for γ_o vs. year. The full extent of the 2002 UH 2.2m error bar is intentionally not displayed so as to be able to see the differences in the remaining measurements. No obvious trend with time can be seen for this parameter.

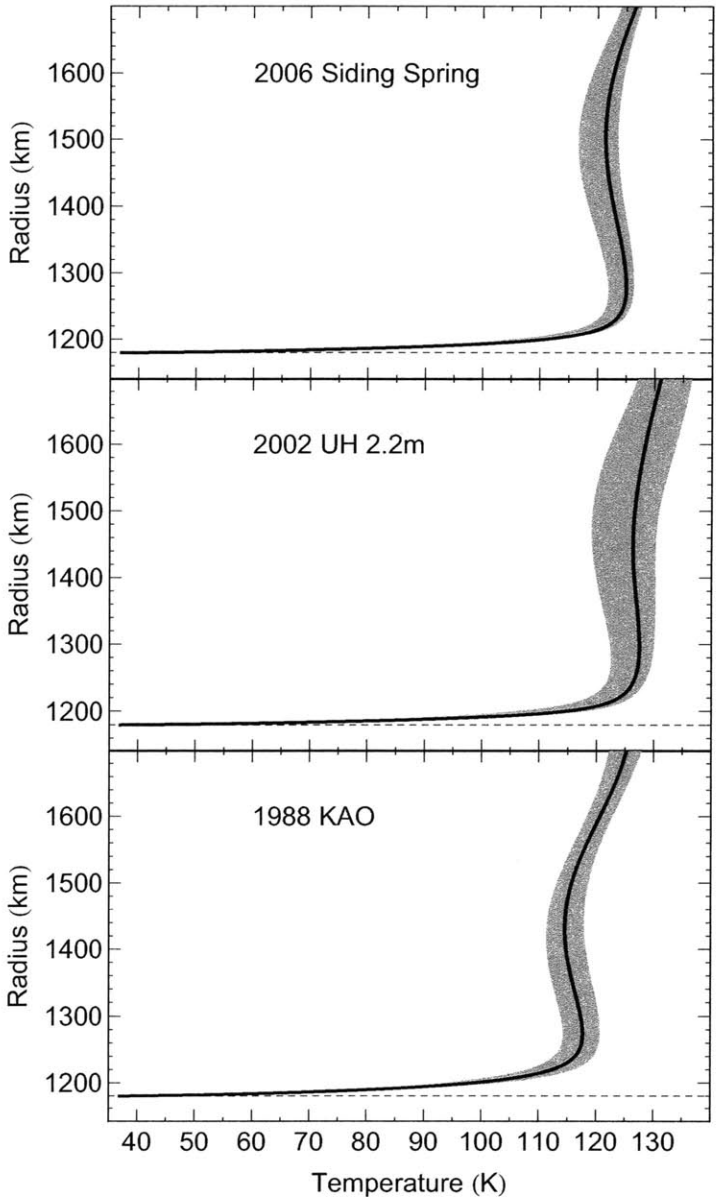

Figure 4-18: Model temperature results corresponding to the best-fit light curves for the 2006 Siding Spring occultation (top), 2002 UH 2.2m (middle), and 1988 KAO (bottom). The solid black line is the fitted value, while the gray shaded area is the range of the formal error bars from the least-squares fit. The dashed black line is the level of the surface.

Chapter 5

Experiments with a Preliminary Pluto General Circulation Model

The Strobel et al. [1996] model used to least-squares fit occultation light curves in Chapter 4 provides radiative equilibrium temperature. Comparisons between model calculated radiative equilibrium temperatures and *in situ* data do not show any planetary atmosphere to be in radiative equilibrium. Therefore it would be naive to assume that Pluto's atmosphere lies in perfect radiative equilibrium. In fact Person et al. [2008] have already shown that this is not the case with their observations of waves and subsequent estimate of limits on wind speed.

General circulation models, as discussed previously, are a widely used tool in exploring planetary circulations. Yet a Pluto GCM (PGCM) has not been presented in the literature. The natural choice for constructing a PGCM would be to combine the dynamical core of the MIT GCM with the radiative transfer code of Strobel et al. [1996], but at present the Strobel et al. [1996] model code is not available for public use. Instead, I tuned the gray radiative-convective radiation scheme of Section 2.1 to temperatures appropriate for Pluto. This step is perhaps a better starting point rather than beginning with the full complexity of the Strobel et al. [1996] model in a GCM. Following the procedure described in Section 2.3.1, I used the gray radiative-convective radiation scheme to thermally force a simple GCM, but now with Pluto physical constants. Admittedly, adjusting the surface optical depth in the gray radiation scheme until the radiative equilibrium temperature roughly approximates the range of the Strobel et al. [1996] model temperature produces fundamentally different equilibrium temperatures. The gray radiation scheme monotonically decreases upward, while the Strobel et al. [1996] model temperature increases near the surface and then become isothermal or decreases depending on the amount of CO. A more accurate radiation scheme is of high priority in future work.

MGCMs have provided the community with decades of experience in dealing with atmospheres where the primary component sublimates and condenses on a seasonal cycle. On Mars the so called condensation flow from the sublimating pole to the condensing pole is small compared to the Hadley circulation. On Pluto this effect could be so large as to dominate the Hadley component, if it exists, changing the character of the circulation from anything previously encountered. It is also possible

that the atmosphere freezes out entirely during certain periods of the year, making a GCM unusable over the course of an entire year.

Hansen and Paige [1996] modeled the seasonal ice cycle on Pluto using a simple thermal model of the surface. They considered the mass transfered to and from the atmosphere at each latitudinal box at progressive seasons, but did not include any atmospheric circulation (i.e. latitudinal transfer of mass between atmospheric boxes). The atmosphere was also transparent to radiation. Depending on the values of their model parameters, namely substrate albedo, frost albedo, thermal inertia, frost emissivity, and total amount of N_2, sufficiently low surface pressures could be achieved at certain seasons in which a redistribution of mass by the atmosphere would require supersonic flow.

At present, a multi-year simple PGCM run is prohibitively expensive from a computational standpoint, even in axisymmetric mode, due to the very long Pluto year (248 Earth years). Therefore I ran the simple PGCM at fixed season (and with diurnally averaged radiation), and investigated the components of the circulation not related to the condensation flow. Like Mars, Pluto's low density leads to a short radiative timescale, at least in the framework of the gray radiation scheme, so a run at fixed season should be similar to a time-varying run (that also does not include the frost cycle). In this configuration, the atmosphere remains at constant mass, and the temperature is instantaneously snapped back to the N_2 condensation temperature if it ever falls below it.

Table 5.1 shows the parameters used in the simple PGCM. Pluto is unusual (thus leading to disagreement in the scientific community) in that one may either define its north pole as being inclined at 112° to the ecliptic so that Pluto rotates counterclockwise when viewed from above the north pole, or define the north pole to be in the same hemisphere of the ecliptic as the Sun's north pole, which implies that Pluto rotates "backwards". I have chosen to follow the latter convention. Buie et al. [2010] presented observations of Pluto's surface that showed significant albedo variations; however I have chosen to use a constant albedo to keep the PGCM simple in its initial stages.

Three experiments were performed corresponding to the dates of three occultations– 9 June 1988 ($L_s = 182.8°$), 21 August 2002 ($L_s = 217.4°$), and 12 June 2006 ($L_s = 226.2°$). The global mean surface pressure was set to the value of 13.2μbar from the 2006 Siding Spring best fit. This value is somewhat arbitrary, as the purpose of the experiments is to see how the circulation alone affects the pressure field apart from the supposed seasonal pressure cycle. As in the simple MGCM of Section 2.3.1, the experiments were done on a cube-sphere grid with 32 × 32 points per cube face (or a horizontal resolution of 2.8°) and 30 vertical levels. The top model level was located at 0.000258 μbar or 206 km log pressure height, assuming a scale height of 19 km (consistent with the average equilibrium temperature). Flat topography was used, as we have no information about the variations in Pluto's surface elevation.

Figure 5-1 shows the radiative-convective (note the fundamental difference from the Strobel et al. [1996] radiative-conductive model) equilibrium temperature used to drive the simple PGCM, while Fig. 5-2 shows the resulting zonally and time averaged (over about 15 Earth days) PGCM temperatures, i.e. the temperatures with the ef-

fects of dynamics included. At all three seasons considered, it is apparent that the circulation affects the resulting temperature so that it is not in radiative equilibrium. Figure 5-3 shows the zonally and time averaged mass stream function. Pluto's circulation near equinox (panel (a)) is characterized by one Hadley cell in each hemisphere that extends almost to the poles; a Ferrel cell is notably absent due to Pluto's slow rotation. A quite different scenario occurs just 14 Earth years later (panel (b)) when Pluto has moved away from equinox toward northern hemisphere summer. Now a single pole-to-pole Hadley cell exists, while a Ferrel cell is still absent. In panel (c), four Earth years later, the circulation has not changed other than becoming slightly more intense. The lack of a Ferrel cell (and inspection of surface pressure plots, not shown), suggests that there is little zonal variation and that the use of an axisymmetric model in the future will prove to be quite adequate.

Figure 5-4 shows the zonally and time averaged surface pressure as a function of latitude from the simple PGCM results. The surface pressure field shows little zonal variation, which is consistent with the lack of eddy activity (i.e. no Ferrel cells) noted in the mass stream function plots. Near equinox (L_s=182.8°), the surface pressure is lower than the global mean pressure near the equator and higher poleward of about 40° latitude. Off equinox (L_s=217.4° and L_s=226.2°), the surface pressure decreases as latitude increases, except for a reversal of this trend in the tropics of the winter (i.e. northern) hemisphere. At any given latitude for each of these seasons, the circulation causes the surface pressure to deviate from the global mean; the maximum amount of deviation for these particular three cases is about 2.5μbar, which occurs during the off equinox seasons.

The maximum difference between the equinox and off equinox cases is also about 2.5 μbar, or a fractional change of 20% [c.f. the fractional change of 50% inferred by Elliot et al., 2003b]. Qualitatively, the simple PGCM surface pressure variation with time agrees better with the Elliot and Young [1992] model analysis [i.e. Elliot et al., 2003b, 2007] than the Strobel et al. [1996] analysis (Chapter 4) in that the former shows a relatively large difference between L_s=182.8° (1988) and L_s=217.4° (2002) but a relatively small difference between L_s=217.4° (2002) and L_s=226.2° (2006). The Strobel et al. [1996] model analysis yields a comparable increase in surface pressure between 1988 and 2002 vs. 2002 and 2006.

Figure 5-5 shows the resultant PGCM wind velocities for the three seasons under discussion. In the plots of u (left column), the zonal jets are located farther poleward than on Earth (due to Pluto's slower rotation) and are easterly (due to Pluto's opposite sense of rotation). The v and ω plots (middle and left columns, respectively) again show the dominance of the Hadley circulation. Near equinox, equatorward (poleward) flow occurs at low (high) altitudes; at the northern summer solstice-like season considered here, flow is southerly (northerly) at low (high) altitudes. The flow rises at the low latitudes near equinox and in the northern (i.e. summer) hemisphere near solstice; it sinks at high latitudes near equinox and in the southern (i.e. winter) hemisphere near solstice. Person et al. [2008] calculate an upper limit on the zonal wind speed of 3 m s^{-1} using the critical zonal wind speed that allows vertical propagation of Rossby waves. This value is much lower than the zonal wind speeds from the PGCM.

The simple PGCM experiments have shown, under the assumptions of a gray atmosphere that does not exchange mass with the surface, that the atmospheric circulation does affect the temperature field and the variation of surface pressure with latitude. The model Pluto atmosphere was in an equinox type configuration in 1988 and a solstice type configuration in 2002 and 2006. The difference (as seen in the temperature, mass stream function, and surface pressure results) between the 1988 and 2002 runs was greater than the difference between the 2002 and 2006.

The results of this initial study with a simple PGCM calls into question the previous occultation analyses such as Elliot et al. [2003b], Sicardy et al. [2003], and Chapter 4 that claimed the surface pressure was increasing with time. Because each occultation event and station samples a different latitude and longitude on Pluto, it is ambiguous if the surface pressure variations observed in e.g. Fig. 4-16 are variations with time, position, or both. Millis et al. [1993] plotted temperature (assumed to be isothermal with height) with latitude for several stations from the 9 June 1988 occultation, and found a scatter of less than 15 K and no systematic variation with latitude. Further development of the PGCM is needed to combine temporal and spatial variations in a self-consistent way.s

Table 5.1: Constants used in PGCM

Parameter	Value	Units
Surface radius	1180	km
Surface gravity	0.63	m s^{-2}
Molecular gas constant	298	J K^{-1} kg^{-1}
Specific heat at constant pressure	1043	J K^{-1} kg^{-1}
Solar day (sol)	551893	s
Rotation rate	-1.13856	$\times 10^{-5}$ s^{-1}
Orbital eccentricity	0.251	...
Orbital inclination	68	°
Semimajor axis	39.67	AU
Initial temperature	80	K
Mean scale height	19	km
Radiative damping time	22076	s
Wind damping rate (k_f)	1/86400	s^{-1}
Reference pressure (p_{oo})[1]	13.2	μbar
Ratio of gas constant to specific heat	2/7	...
Specific latent heat (of N_2)	253	kJ kg^{-1}
Surface albedo	0.3	...
L_s of perihelion	185.858	°
Mean solar constant	0.864465	W m^{-2}
Gray optical depth at reference pressure (τ_{oo})	2	...

[1]Set to global mean surface pressure

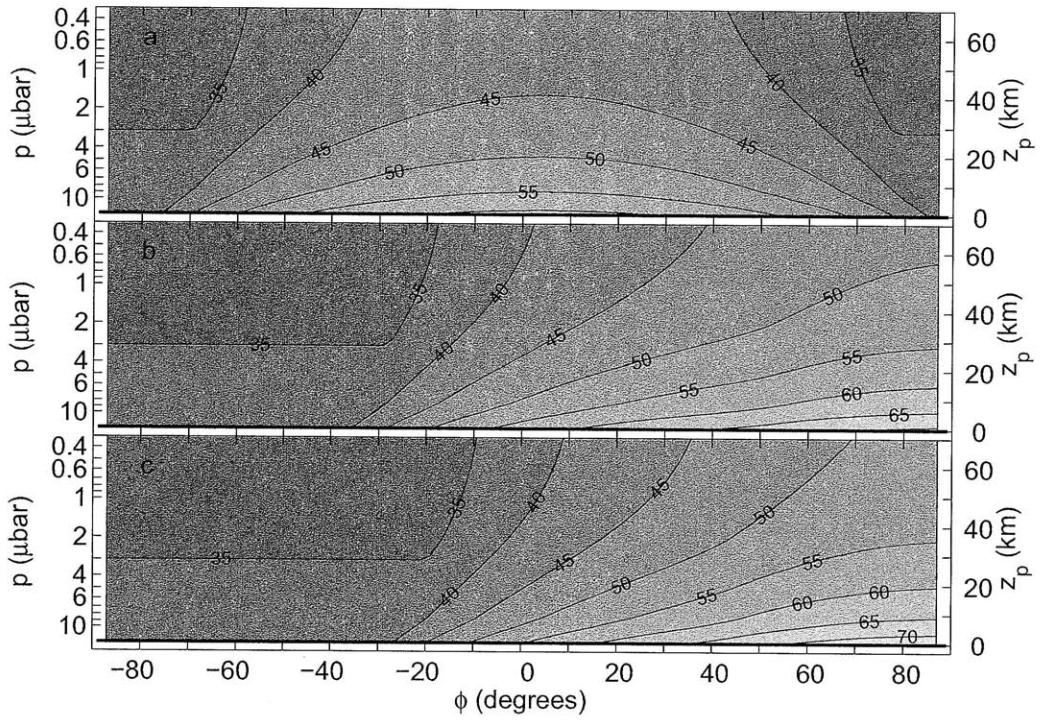

Figure 5-1: Radiative-convective equilibrium temperature (units in K) for the simple PGCM. Latitude is plotted on the x-axis, pressure is plotted on the left y-axis, and log pressure height is plotted on the right y-axis, assuming a scale height of 19 km and a reference pressure of 13.2 μbar. Only temperatures below $\sim$0.3 μbar (70 km log pressure height) are shown. From top to bottom, the rows are are L_s=182.8, 217.4, and 226.2°. Contour interval is 5 K.

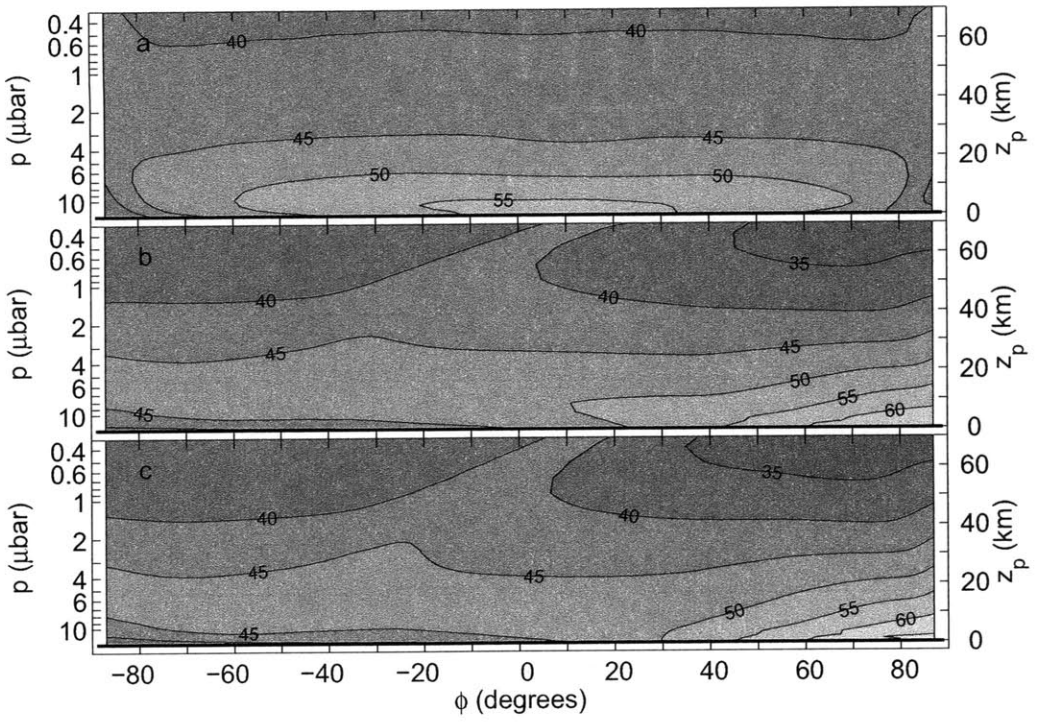

Figure 5-2: Zonally and time averaged temperature results (units in K) for the simple PGCM. Latitude is plotted on the x-axis, pressure is plotted on the left y-axis, and log pressure height is plotted on the right y-axis, assuming a scale height of 19 km and a reference pressure of 13.2 μbar. Only temperatures below $\sim$0.3 μbar (70 km log pressure height) are shown. From top to bottom, the rows are are L_s=182.8, 217.4, and 226.2°. Contour interval is 5 K.

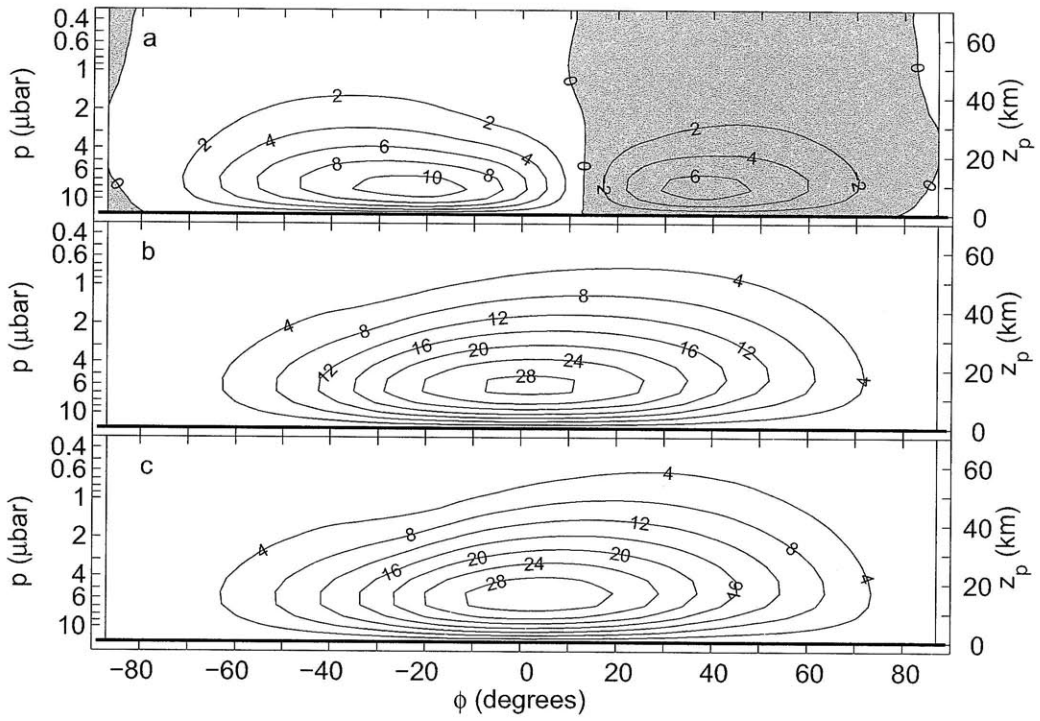

Figure 5-3: Simple PGCM results for zonally and time averaged mass stream function with radiative-convective forcing. Units are 10^7 kg s^{-1}. Positive flow is counterclockwise; negative contours are shaded. Latitude is plotted on the x-axis, pressure is plotted on the left y-axis, and log pressure height is plotted on the right y-axis, assuming a scale height of 19 km and a reference pressure of 13.2 μbar. Only results below $\sim$0.3 μbar (70 km log pressure height) are shown. From top to bottom, the rows are are L_s=182.8, 217.4, and 226.2°. Note the different contour intervals (2×10^7 kg s^{-1} for panel (a) and 4×10^7 kg s^{-1} for panels (b) and (c)).

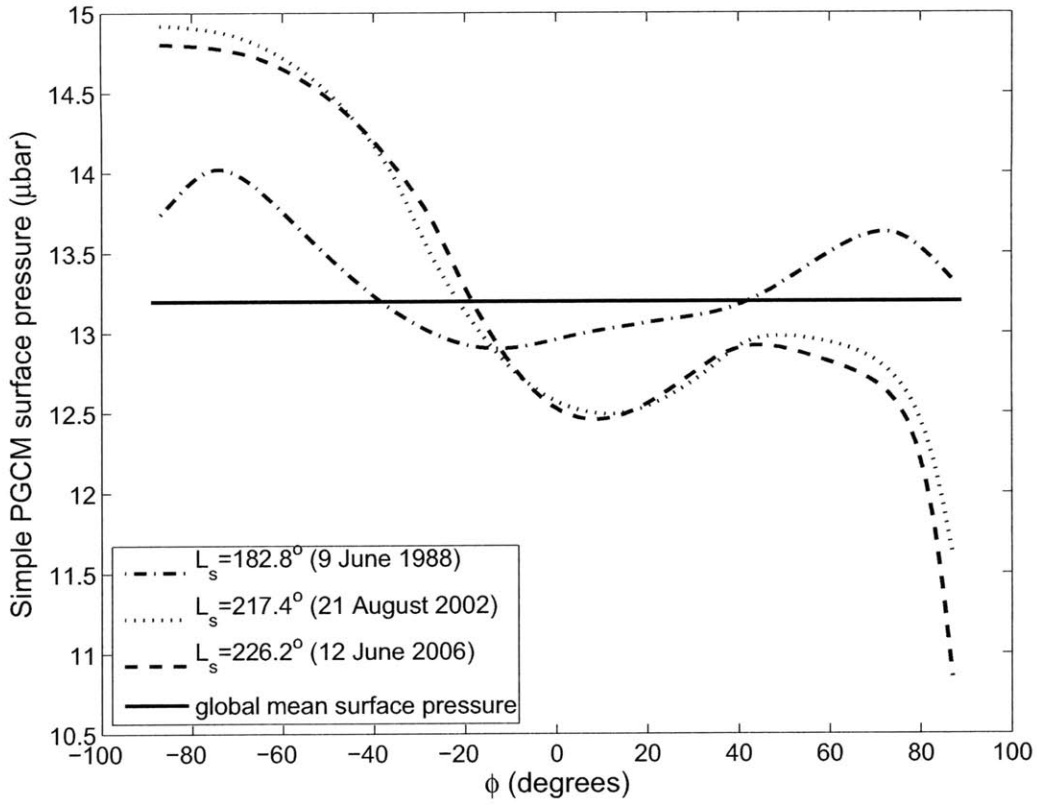

Figure 5-4: Zonally and time averaged surface pressure results (units in μbar) for the simple PGCM. The plot indicates that at any given latitude, the circulation in general will differ from the global mean surface pressure (solid black line). Also, the surface pressure as a function of latitude is different for different seasons.

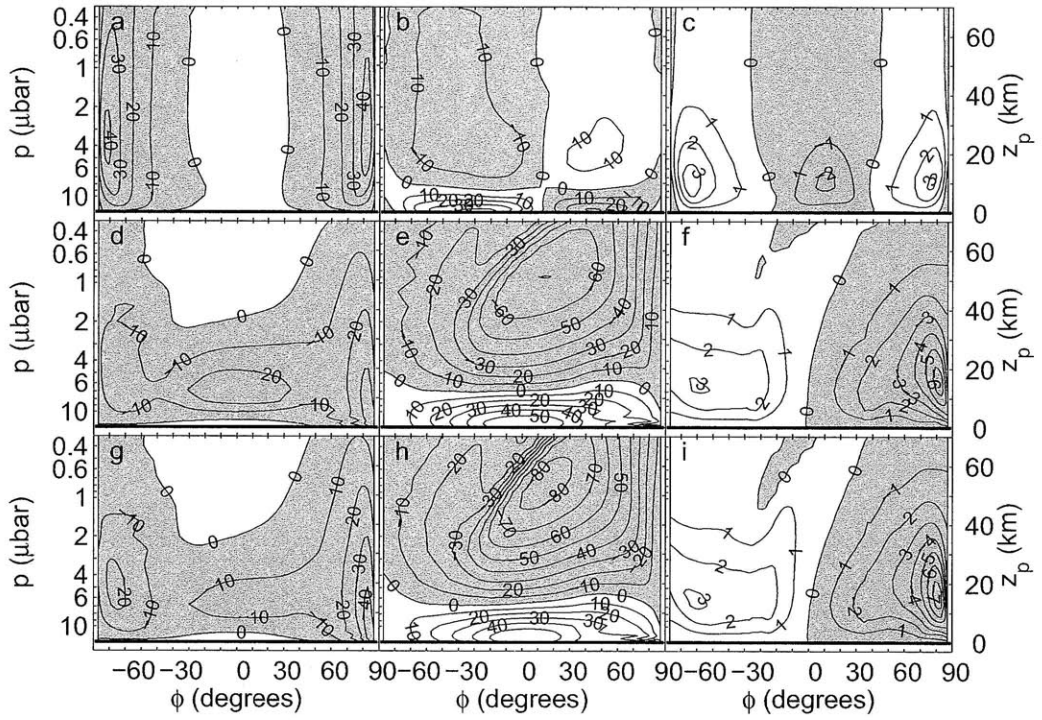

Figure 5-5: Zonally and time averaged wind velocity for the simple PGCM. The left column is u (m s^{-1}), the middle column is v (m s^{-1}), and the right column is ω (10^{-4} μbar s^{-1}). From top to bottom, the rows are are L_s=182.8, 217.4, and 226.2°. Only results below ~0.3 μbar (70 km log pressure height) are shown. Negative contours are shaded. Contour intervals are 10 m s^{-1} for u and v and 1×10^{-4} μbar s^{-1} for ω

Appendix A

Glossary of Symbols

Table A.1: Glossary of Symbols

Symbol	Definition
A	Albedo
a	Planetary radius
B	Convective flux (positive upwards)
b	Temperature power index on Elliot and Young [1992] model
C_d	Drag coefficient
C_h	Heat transfer coefficient
c_p	Specific heat at constant pressure
C_v	Specific heat at constant volume
D	Distance to observer
d	Sun-Mars distance
e	Orbital eccentricity
F	A shorthand function in Lindzen and Hou [1988] model
g	Acceleration of gravity at the surface
H	Equivalent depth
h	Height of the top of the Hadley cell
h_c	Altitude of the top of the convecting layer
i	Obliquity
K	Thermal conductivity
K_o	Reference thermal conductivity
k_T	Radiative relaxation rate
k_f	Wind damping rate of the lower atmosphere
k_v	Wind damping rate
k_w	Rate at which temperature anomaly develops in...
	...Webster [1977] model
L	Specific latent heat of sublimation
L_o	Loschmidt constant
L_s	Ecliptic longitude of Sun in planet centered coordinates...

Continued on next page

Table A.1 – continued from previous page

Symbol	Definition
	...(angular measure of season)
L_{sp}	L_s of perihelion
$L_\odot$	Solar luminosity
l	Monin-Obokhov length
l_o	Roughness length
M	Absolute angular momentum
M_a	Relative angular momentum
M_0	Absolute angular momentum for rising branch of Hadley cell
m	Inverse of steepness of slope of idealized topography
N	Brunt-Väisälä frequency
n	Number density
n_o	Number density at surface
p	Pressure
p_a	An arbitrary pressure aloft (in the convecting layer)
p_b	Pressure at the top of frictional boundary layer
p_o	Height of the surface in pressure coordinates
p_{oo}	Reference pressure (zero elevation)
p_s	Surface pressure
p_1	Reference pressure for CO_2 condensation
Q_o	Daily averaged net solar flux
Q^*	Heating rate due to topography in Webster [1977]
R	Specific gas constant
R_{net}	Heating rate
r	Radius from occulting body's center
r_H	Half-light radius
r_{top}	Top level of Strobel et al. [1996] radiative-conductive model
r_{max}	Maximum radius to which integration is carried out...
	...in refraction angle calculation
r_s	Surface radius
r'	Radial distance from the center of occulting body...
	...along the path of light ray
S	Solar constant
S_o	Mean solar constant
s_{bf}	Background fraction
s_{fs}	Full scale flux
s_s	Slope (in flux)
T	Temperature
T_{co2}	CO_2 condensation temperature
T_{eq}	Equilibrium temperature
$T_{eq,R}$	Pure radiative equilibrium temperature
$T_{eq,RC}$	Pure radiative-convective equilibrium temperature

Continued on next page

Table A.1 – continued from previous page

Symbol	Definition
T_g	Surface temperature in pure radiative equilibrium
T_H	Half-light temperature
T_1	Reference temperature for CO_2 condensation
T_s	Surface temperature
t	Time
t_{min}	Time of closest approach
u	Zonal velocity
$\|\|\mathbf{v}\|\|$	Magnitude of horizontal surface wind
V	Relative velocity between the observer and occulting body
v	Meridional velocity
w	Vertical velocity
X_e	Forcing function
x	Distance along path of light ray
y	Distance from center of shadow plane
y_{min}	Distance of closest approach
z	Height above the reference surface (altitude)
z_b	Height of the surface
z_{bi}	Height of idealized mean topography (in km)
z_p	Log pressure height
z_m	Height of idealized topography with off-equatorial... ...mountain (in km)
z_{mm}	MOLA mean topography (in km)
α	Thermal conductivity power index
β	CH_4 mixing ratio power index
Γ	Lapse rate
Γ_a	Adiabatic lapse rate
γ	CH_4 volume mixing ratio (with respect to N_2)
γ_o	CH_4 volume mixing ratio at surface
δ	Declination of the Sun
ϵ	Depth of the convecting layer
ζ	Dimensionless height
ζ_o	Dimensionless of surface roughness
η	CO mixing ratio (not to be confused with η vertical coordinate)
$\Delta\Theta_s$	Potential difference between atmosphere... ...(above the surface layer) and ground
Θ	Potential temperature
Θ_e	Equilibrium potential temperature
Θ_e^C	Equilibrium potential temperature in convecting layer
Θ_e^R	Equilibrium potential temperature above convecting layer
Θ_e^S	Surface radiative-convective equilibrium temperature
Θ_o	Constant reference temperature

Continued on next page

Table A.1 – continued from previous page

Symbol	Definition
θ	Refraction angle
κ	von Kármán's constant (0.4)
Λ	Unnormalized light curve flux
λ	Longitude
ν	Refractivity
ν_{STP}	Refractivity at standard temperature and pressure
ξ	Hour angle of sunrise and sunset
ρ	Density of air
σ	Stefan-Boltzmann constant
τ	Optical depth
τ_{los}	Line of sight optical depth
τ_o	Optical depth at the surface
τ_{oo}	Optical depth at p_{oo}
τ_t	Optical depth at the top of convective layer
τ_*	Optical depth variable of integration
Φ	Geopotential
$\hat{\Phi}$	Integration constant (units of geopotential)
ϕ	Latitude
ϕ_c	Arbitrary latitude (integration limit)
ϕ_1	Latitude of the dividing streamline between Hadley cells
ϕ_+	Latitude of poleward boundary of northern Hadley cell
ϕ_-	Latitude of poleward boundary of southern Hadley cell
ϕ'	Variable of integration
χ	Normalized light curve flux
Ψ_m	Argument of drag coefficient integral
Ψ_h	Argument of heat transfer coefficient integral
ψ	Light curve flux (single limb)
Ω	Planetary rotation rate
ω	Vertical velocity in pressure coordinates
$[Y]$	Zonal average of Y
$\overline{Y}$	Time average of Y
Y^*	Departure from zonal average of Y
Y'	Departure from time average of Y

Appendix B

Light Curve Data

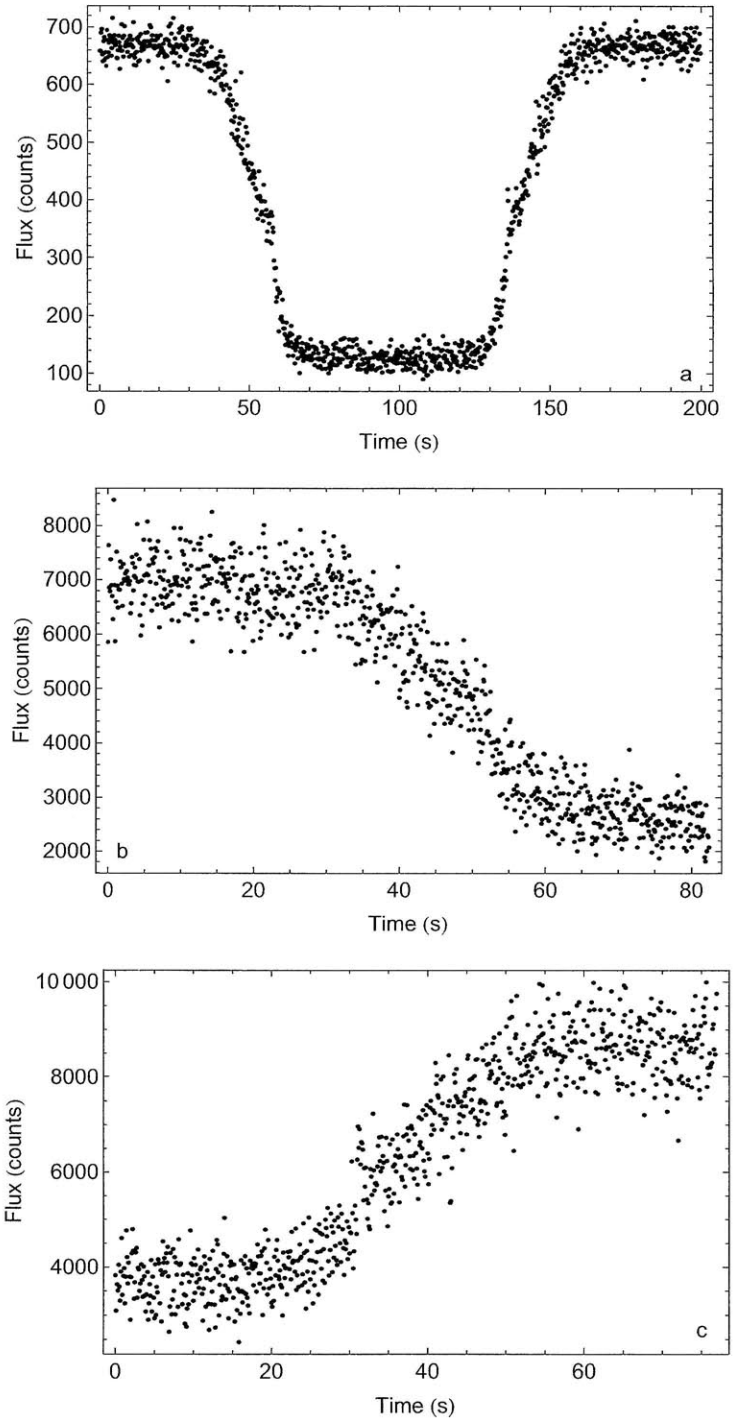

Figure B-1: (a) 1988 KAO light curve data, (b) 1988 Charters Towers immersion light curve data, and (c) 1988 Charters Towers emersion light curve data. The time scale has been set to zero at the start of the dataset.

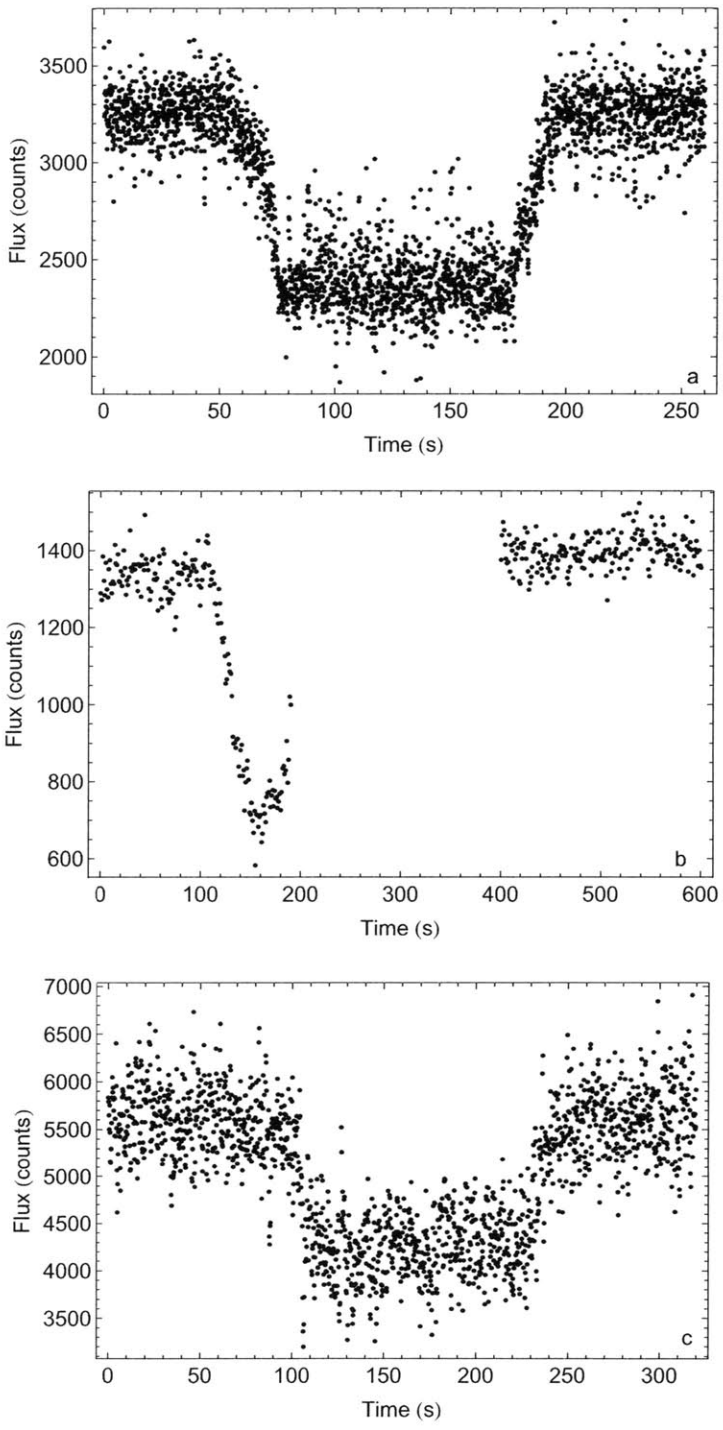

Figure B-2: (a) 1988 Aukland light curve data, (b) 1988 Black Birch light curve data, and (c) 1988 Toowoomba light curve data. The time scale has been set to zero at the start of the dataset.

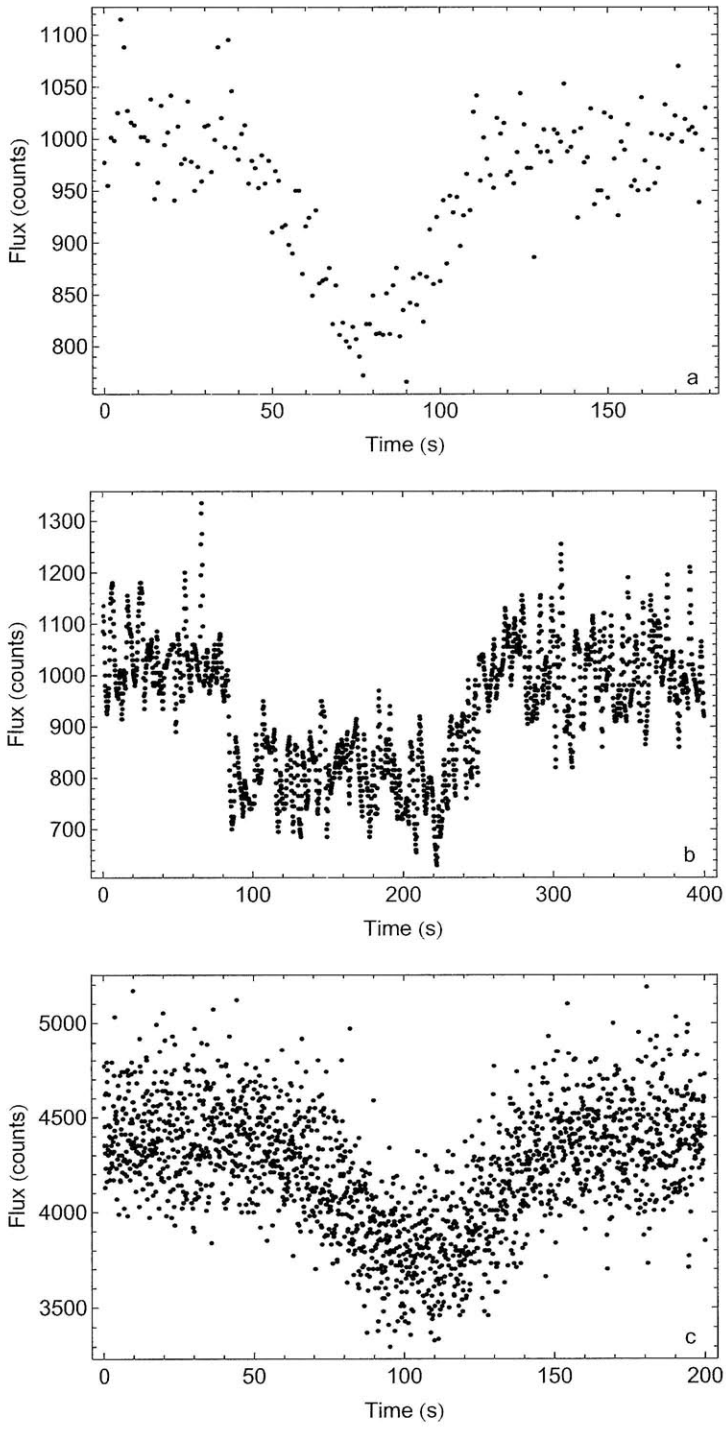

Figure B-3: (a) 1988 Mt. John light curve data, (b) 1988 Mt. Tambourine light curve data, and (c) 1988 Hobart light curve data. The time scale has been set to zero at the start of the dataset.

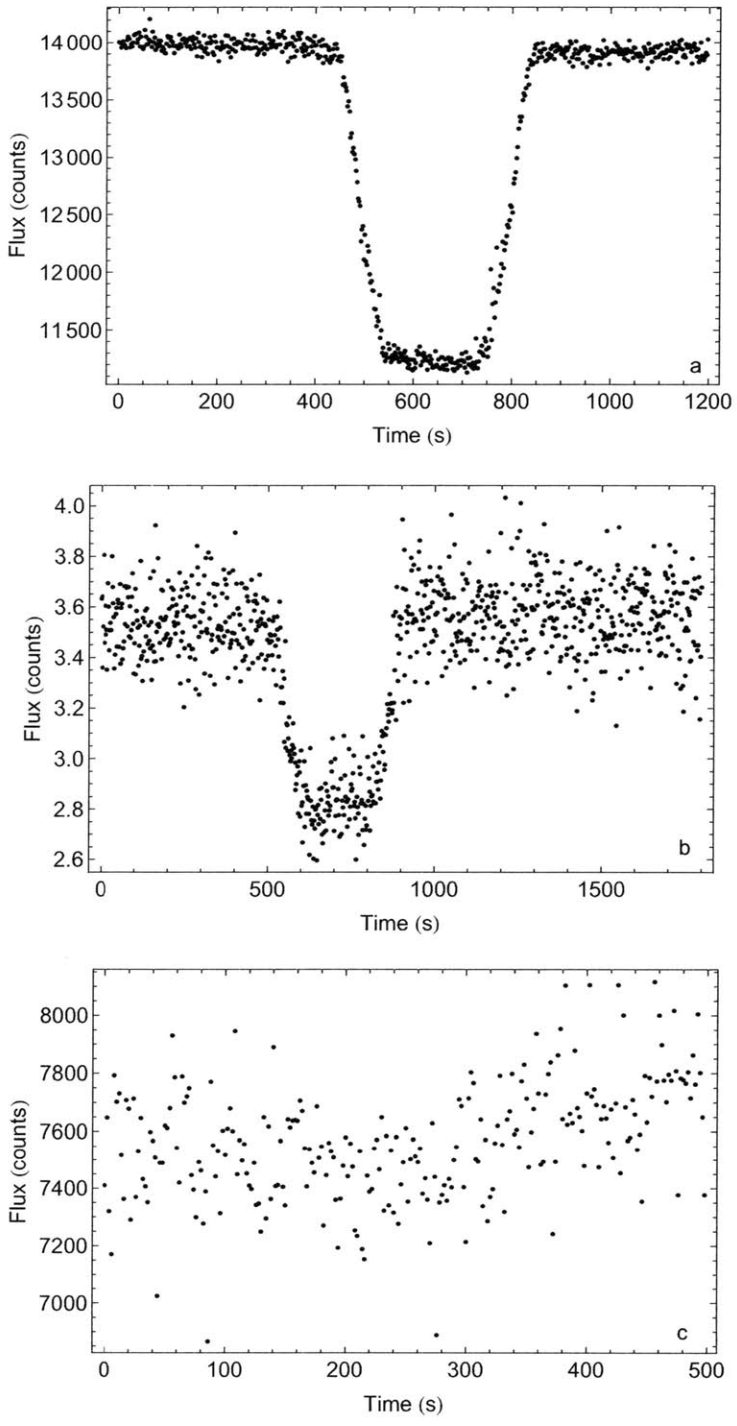

Figure B-4: (a) 2002 UH 2.2m light curve data, (b) 2002 Lick light curve data, and (c) 2002 Palomar light curve data. The time scale has been set to zero at the start of the dataset.

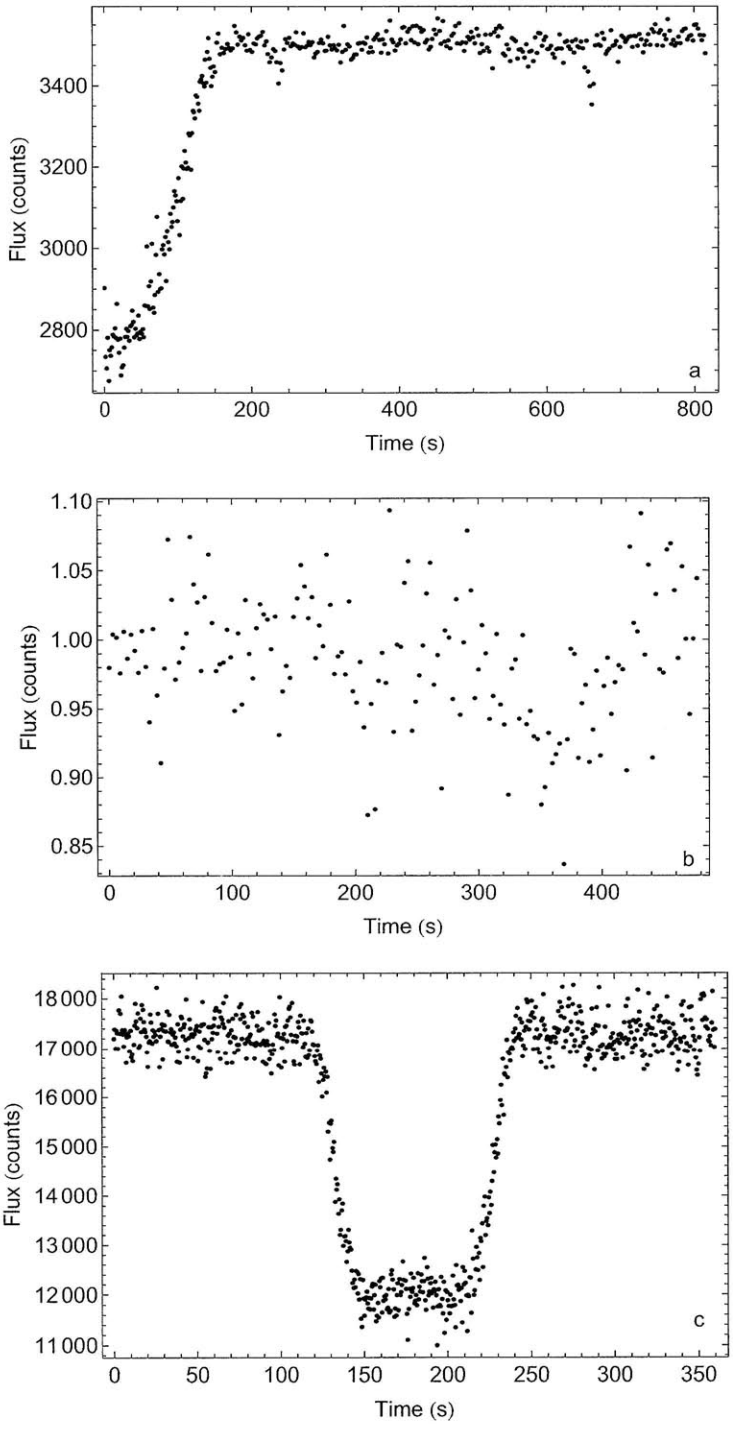

Figure B-5: (a) 2002 Maui light curve data, (b) 2002 Lowell light curve data, and (c) 2006 Black Springs light curve data. The time scale has been set to zero at the start of the dataset.

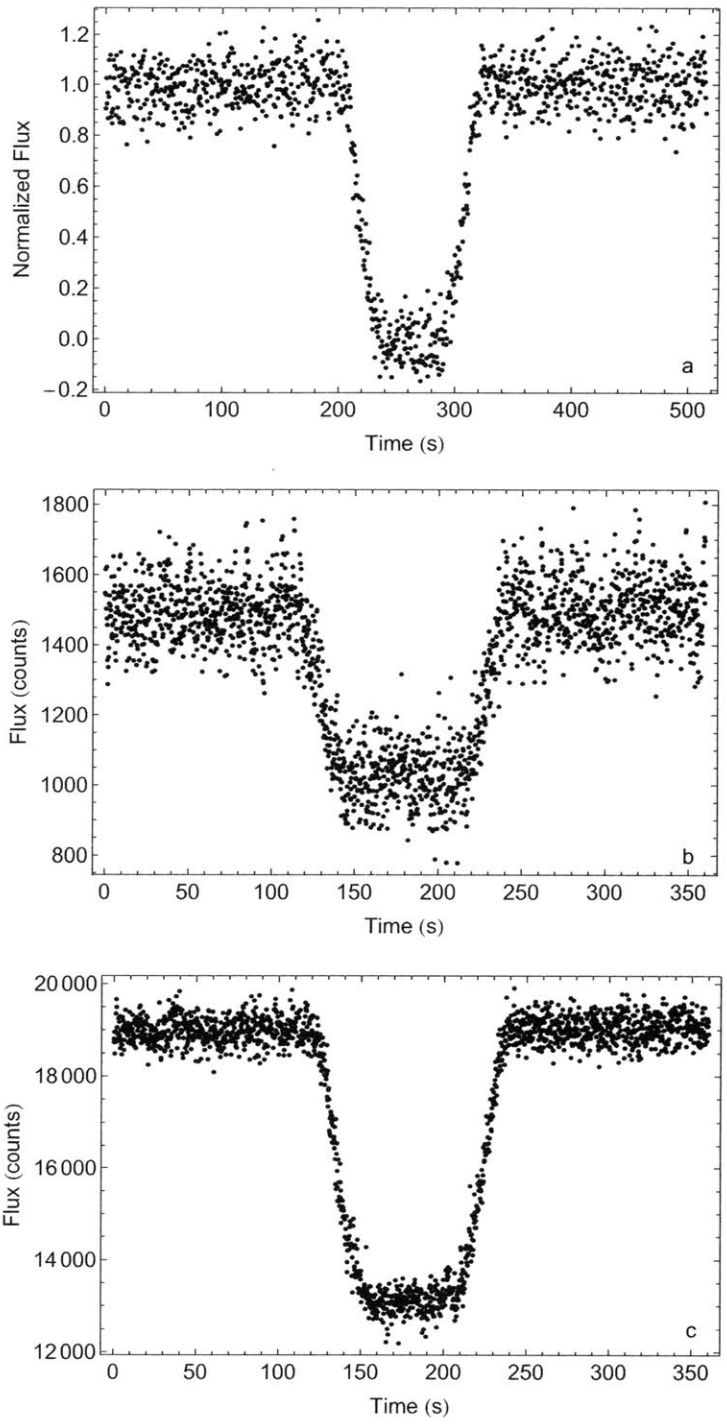

Figure B-6: (a) 2006 Hobart light curve data, (b) 2006 Mt. Stromlo light curve data, and (c) 2006 Siding Spring light curve data. The time scale has been set to zero at the start of the dataset. The data have already been normalized for 2006 Hobart.

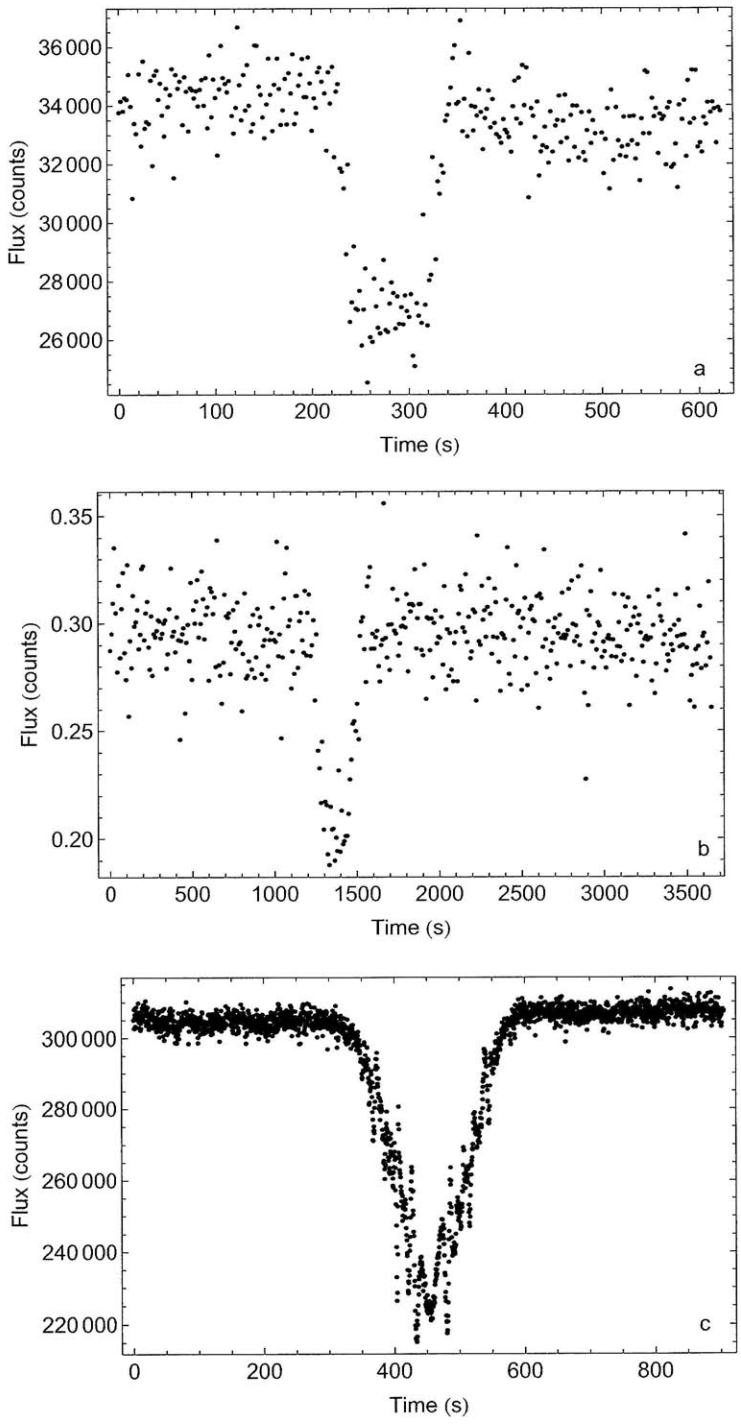

Figure B-7: (a) 2006 Stockport light curve data, (b) 2007 Fremont Peak light curve data, and (c) 2007 MMT (IR) light curve data. The time scale has been set to zero at the start of the dataset.

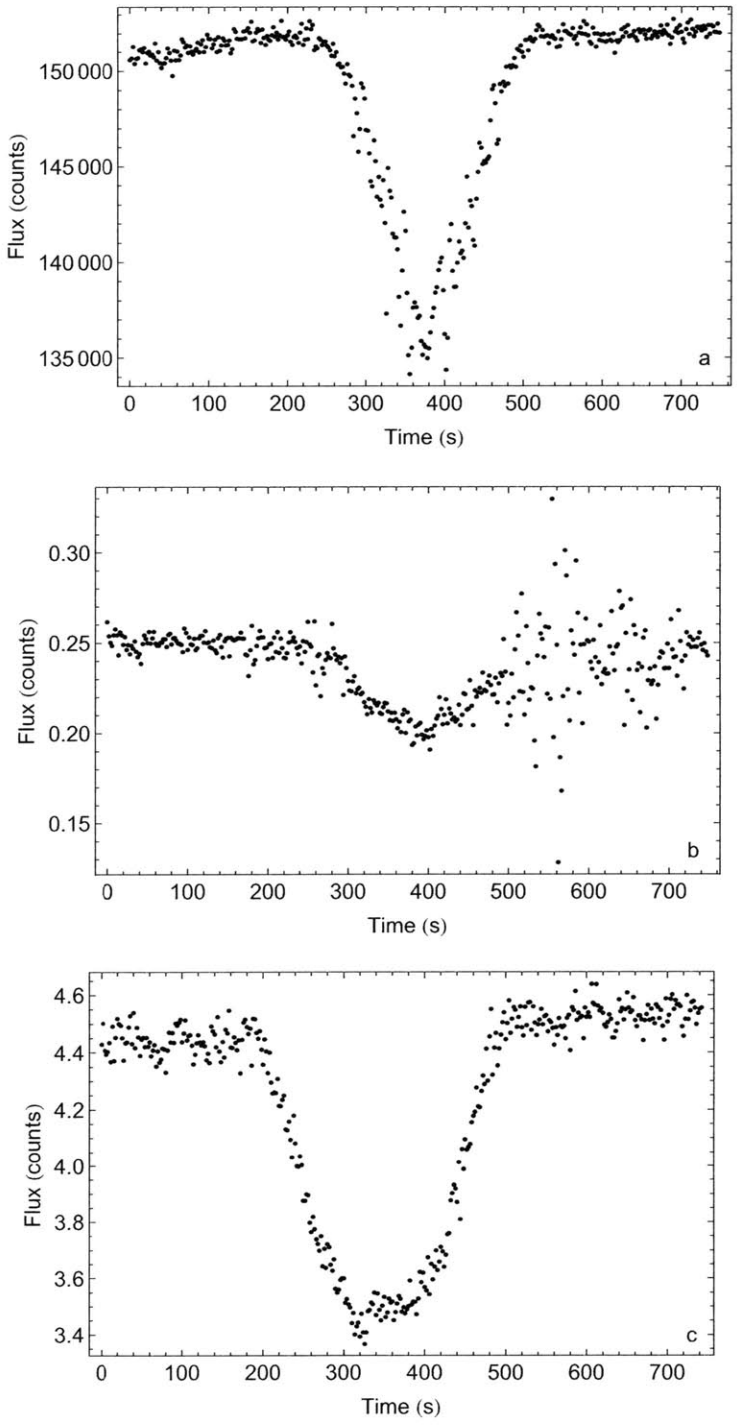

Figure B-8: (a) 2007 MMT (visible) light curve data, (b) 2007 MRO light curve data, and (c) 2007 USNO light curve data. The time scale has been set to zero at the start of the dataset.

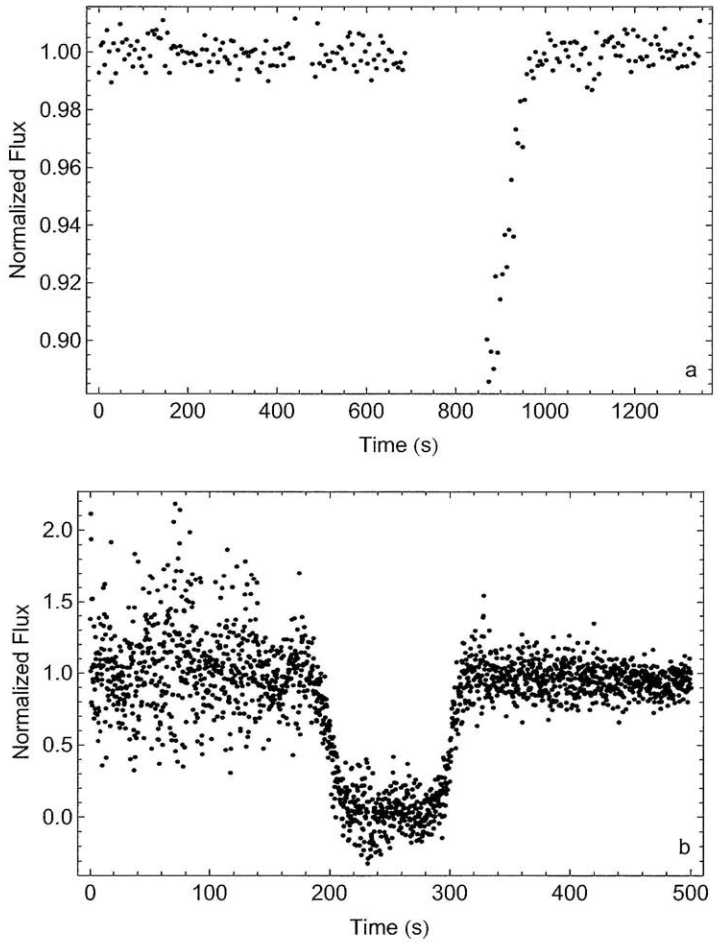

Figure B-9: (a) 2007 LBTO light curve data and (b) 2008 IRTF light curve data. The time scale has been set to zero at the start of the dataset. The data have already been normalized in both cases.

Bibliography

Adcroft, A. and J.-M. Campin, 2004: Rescaled height coordinates for accurate representation of free-surface flows in ocean circulation models. *Ocean Modelling*, **7**, 269–284.

Adcroft, A., J.-M. Campin, C. Hill, and J. Marshall, 2004: Implementation of an atmosphere-ocean general circulation model on the expanded spherical cube. *Mon. Wea. Rev.*, **132**, 2845–2863.

Adcroft, A., C. Hill, and J. Marshall, 1997: Representation of topography by shaved cells in a height coordinate ocean model. *Mon. Wea. Rev.*, **125**, 2293.

Andrews-Hanna, J. C., M. T. Zuber, and W. B. Banerdt, 2008: The Borealis basin and the origin of the Martian crustal dichotomy. *Nature*, **453**, 1212–1215, doi: 10.1038/nature07011.

Barth, C. A., A. I. F. Stewart, S. W. Bougher, D. M. Hunten, S. J. Bauer, and A. F. Nagy, 1992: Aeronomy of the current Martian atmosphere. *Mars*, H. H. Kieffer, Ed., University of Arizona Press, Tucson, 1054–1089.

Basu, S., M. I. Richardson, and R. J. Wilson, 2004: Simulation of the Martian dust cycle with the GFDL Mars GCM. *J. Geophys. Res.*, **109 (E18)**, doi: 10.1029/2004JE002243.

Basu, S., J. Wilson, M. Richardson, and A. Ingersoll, 2006: Simulation of spontaneous and variable global dust storms with the GFDL Mars GCM. *J. Geophys. Res.*, **111**, E09 004, doi:10.1029/2005JE002660.

Baum, W. A. and A. D. Code, 1953: A photometric observation of the occultation of σ ARIETIS by Jupiter. *Astron. J.*, **58**, 108–112, doi:10.1086/106829.

Brosch, N., 1995: The 1985 stellar occultation by Pluto. *Mon. Not. R. Astron. Soc.*, **276**, 571–578.

Buie, M. W. and U. Fink, 1987: Methane absorption variations in the spectrum of Pluto. *Icarus*, **70**, 483–498.

Buie, M. W., W. M. Grundy, E. F. Young, L. A. Young, and S. A. Stern, 2010: Pluto and Charon with the Hubble Space Telescope. II. Resolving changes on Pluto's

surface and a map for Charon. *Astron. J.*, **139**, 1128–1143, doi:10.1088/0004-6256/139/3/1128.

Caballero, R., R. T. Pierrehumbert, and J. L. Mitchell, 2008: Axisymmetric, nearly inviscid circulations in non-condensing radiative-convective atmospheres. *Quart. J. Roy. Meteor. Soc.*, **134**, 1269–1285, doi:10.1002/qj.271.

Chamberlain, D. M. and J. L. Elliot, 1997: A numerical method for calculating stellar occultation light curves from an arbitrary atmospheric model. *Publ. Astron. Soc. Pacific*, **109**, 1170–1180, doi:10.1086/133992.

Colburn, D. S., J. B. Pollack, and R. M. Haberle, 1989: Diurnal variations in optical depth at Mars. *Icarus*, **79**, 159–189, doi:10.1016/0019-1035(89)90114-0.

Cruikshank, D. P., C. B. Pilcher, and D. Morrison, 1976: Pluto: Evidence for methane frost. *Science*, **194**, 835–837.

Dima, I. M. and J. M. Wallace, 2003: On the seasonality of the Hadley cell. *J. Atmos. Sci.*, **60**, 1522–1527, doi:10.1175/1520-0469(2003)060¡1522:OTSOTH¿2.0.CO;2.

Elliot, J. L., E. W. Dunham, A. S. Bosh, S. M. Slivan, L. A. Young, L. H. Wasserman, and R. L. Millis, 1989: Pluto's atmosphere. *Icarus*, **77**, 148–170, doi:10.1016/0019-1035(89)90014-6.

Elliot, J. L., R. G. French, E. Dunham, P. J. Gierasch, J. Veverka, C. Church, and C. Sagan, ????: Occultation of Epsilon Geminorum by Mars. II - The structure and extinction of the Martian upper atmosphere. *Astrophys. J.*, **217**, 661–679, doi:10.1086/155612.

Elliot, J. L., R. G. French, E. Dunham, P. J. Gierasch, J. Veverka, C. Church, and C. Sagan, 1977: Occultation of Epsilon Geminorum by Mars - Evidence for atmospheric tides. *Science*, **195**, 485–486.

Elliot, J. L. and C. B. Olkin, 1996: Probing planetary atmospheres with stellar occultations. *Annu. Rev. of Earth and Planet. Sci.*, **24**, 89–124, doi:10.1146/annurev.earth.24.1.89.

Elliot, J. L., M. J. Person, and S. Qu, 2003a: Analysis of stellar occultation data. II. Inversion, with application to Pluto and Triton. *Astron. J.*, **126**, 1041–1079, doi:10.1086/375546.

Elliot, J. L. and L. A. Young, 1992: Analysis of stellar occultation data for planetary atmospheres. I - Model fitting, with application to Pluto. *Astron. J.*, **103**, 991–1015, doi:10.1086/116121.

Elliot, J. L., et al., 2003b: The recent expansion of Pluto's atmosphere. *Nature*, **424**, 165–168.

Elliot, J. L., et al., 2007: Changes in Pluto's atmosphere: 1988-2006. *Astron. J.*, **134**, 1–13, doi:10.1086/517998.

Fink, U. B., A. Smith, D. C. Benner, J. R. Johnson, H. J. Reitsema, and J. A. Westphai, 1980: Detection of a CH_4 atmosphere on Pluto. *Icarus*, **44**, 62–71.

Forget, F., et al., 1999: Improved general circulation models of the Martian atmosphere from the surface to above 80 km. *J. Geophys. Res.*, **104 (E10)**, 24 155–24 175.

Gill, A. E., 1980: Some simple solutions for heat-induced tropical circulation. *Quart. J. Roy. Meteor. Soc.*, **106**, 447–462, doi:10.1256/smsqj.44904.

Gulbis, A. A. S. et al., 2010: In preparation.

Haberle, R. M., H. Houben, J. R. Barnes, and R. E. Young, 1997: A simplified three-dimensional model for Martian climate studies. *J. Geophys. Res.*, **102**, 9051–9068, doi:10.1029/97JE00383.

Haberle, R. M., H. C. Houben, R. Hertenstein, and T. Herdtle, 1993: A boundary-layer model for Mars - Comparison with Viking lander and entry data. *J. Atmos. Sci.*, **50**, 1544–1559, doi:10.1175/1520-0469(1993)050.

Haberle, R. M., J. B. Pollack, J. R. Barnes, R. W. Zurek, C. B. Leovy, J. R. Murphy, H. Lee, and J. Schaeffer, 1993: Mars atmospheric dynamics as simulated by the NASA Ames general circulation model 1. The zonal-mean circulation. *J. Geophys. Res.*, **98 (E2)**, 3093–3123.

Hansen, C. J. and D. A. Paige, 1996: Seasonal nitrogen cycles on Pluto. *Icarus*, **120**, 247–265, doi:10.1006/icar.1996.0049.

Hartogh, P., A. S. Medvedev, T. Kuroda, and R. Saito, 2005: Description and climatology of a new general circulation model of the Martian atmosphere. *J. Geophys. Res.*, **110**, E11 008, doi:10.1029/2005JE002498.

Held, I. M. and A. Y. Hou, 1980: Nonlinear axially symmetric circulations in a nearly inviscid atmosphere. *J. Atmos. Sci.*, **37**, 515–533.

Held, I. M. and M. J. Suarez, 1994: A proposal for the intercomparison of the dynamical cores of atmospheric general circulation models. *Bull. Amer. Meteor. Soc.*, **75 (10)**, 1825–1830.

Hess, S. L., J. A. Ryan, J. E. Tillman, R. M. Henry, and C. B. Leovy, 1980: The annual cycle of pressure on Mars measured by Viking Landers 1 and 2. *Geophys. Res. Lett.*, **7**, 197–200.

Hinson, D. P., M. Pätzold, S. Tellmann, B. Häusler, and G. L. Tyler, 2008: The depth of the convective boundary layer on Mars. *Icarus*, **198**, 57–66, doi: 10.1016/j.icarus.2008.07.003.

Hinson, D. P., G. L. Tyler, J. L. Hollingsworth, and R. J. Wilson, 2001: Radio occultation measurements of forced atmospheric waves on Mars. *J. Geophys. Res.*, **106 (E1)**, 1463–1480.

Hinson, D. P. and R. J. Wilson, 2002: Transient eddies in the southern hemisphere of Mars. *Geophys. Res. Lett.*, **29 (7)**, doi:10.1029/2001GL014103.

Hinson, D. P. and R. J. Wilson, 2004: Temperature inversions, thermal tides, and water ice clouds in the Martian tropics. *J. Geophys. Res.*, **109 (E18)**, doi: 10.1029/2003JE002129.

Hinson, D. P., R. J. Wilson, M. D. Smith, and B. J. Conrath, 2003: Stationary planetary waves in the atmosphere of Mars during southern winter. *J. Geophys. Res.*, **108**, doi:10.1029/2002JE001949.

Hourdin, F., F. Forget, and O. Talagrand, 1995: The sensitivity of the Martian surface pressure and atmospheric mass budget to various parameters: A comparison between numerical simulations and Viking observations. *J. Geophys. Res.*, **100**, 5501–5523.

Hourdin, F., P. Le van, F. Forget, and O. Talagrand, 1993: Meteorological variability and the annual surface pressure cycle on Mars. *J. Atmos. Sci.*, **50**, 3625–3640, doi:10.1175/1520-0469(1993)050.

Hubbard, W. B., D. M. Hunten, S. W. Dieters, K. M. Hill, and R. D. Watson, 1988: Occultation evidence for an atmosphere on Pluto. *Nature*, **336**, 452–454, doi:10.1038/336452a0.

Hubbard, W. B., D. W. McCarthy, C. A. Kulesa, S. D. Benecchi, M. J. Person, J. L. Elliot, and A. A. S. Gulbis, 2009: Buoyancy waves in Pluto's high atmosphere: Implications for stellar occultations. *Icarus*, **204**, 284–289, doi: 10.1016/j.icarus.2009.06.022.

Hubbard, W. B., R. V. Yelle, and J. I. Lunine, 1990: Nonisothermal Pluto atmosphere models. *Icarus*, **84**, 1–11, doi:10.1016/0019-1035(90)90154-2.

Hunt, G. E., 1983: The atmospheres of the outer planets. *Annu. Rev. of Earth and Planet. Sci.*, **11**, 415–459, doi:10.1146/annurev.ea.11.050183.002215.

James, P., H. H. Kiefferand, and D. A. Paige, 1992: The seasonal cycle of carbon dioxide on Mars. *Mars*, H. H. Kieffer, Ed., University of Arizona Press, Tucson, 934–968.

Joshi, M. M., S. R. Lewis, P. L. Read, and D. C. Catling, 1995: Western boundary currents in the Martian atmosphere: Numerical simulations and observational evidence. *J. Geophys. Res.*, **100 (E3)**, 5485–5500.

Kahre, M. A., J. L. Hollingsworth, R. M. Haberle, and J. R. Murphy, 2008: Investigations of the variability of dust particle sizes in the Martian atmosphere using the NASA Ames General Circulation Model. *Icarus*, **195**, 576–597, doi:10.1016/j.icarus.2008.01.023.

Kahre, M. A., J. R. Murphy, and R. M. Haberle, 2006: Modeling the Martian dust cycle and surface dust reservoirs with the NASA Ames general circulation model. *J. Geophys. Res.*, **111**, E06 008, doi:10.1029/2005JE002588.

Kovalevsky, J. and F. Link, 1969: Diameter, flattening and optical properties of the upper atmosphere of Neptune as derived from the occultation of BD -17 4388. *Astron. Astrophys.*, **2**, 398–412.

Kuroda, T., N. Hashimoto, D. Sakai, and M. Takahashi, 2005: Simulation of the Martian atmosphere using a CCSR/NIES AGCM. *J. Meteor. Soc. Japan*, **83 (1)**, 1–19.

Kuroda, T., A. S. Medvedev, P. Hartogh, and M. Takahashi, 2009: On forcing the winter polar warmings in the Martian middle atmosphere during dust storms. *Journal of the Meteorological Society of Japan*, **87 (5)**, 913–921.

Larsen, S. E., H. E. Jørgensen, L. Landberg, and et al., 2002: Aspects of the atmospheric surface layers on Mars and Earth. *Boundary-Layer Meteorology*, **105**, 451–470, doi:10.1023/A:1020338016753.

Lellouch, E., 1994: The thermal structure of Pluto's atmosphere: Clear vs hazy models. *Icarus*, **108**, 255–264, doi:10.1006/icar.1994.1060.

Lellouch, E., C. de Bergh, B. Sicardy, S. Ferron, and H.-U. Käufl, 2010: Detection of CO in Triton's atmosphere and the nature of surface-atmosphere interactions. *Astron. Astrophys.*, In press.

Lellouch, E., B. Sicardy, C. de Bergh, H.-U. Käufl, S. Kassi, and A. Campargue, 2009: Pluto's lower atmosphere structure and methane abundance from high-resolution spectroscopy and stellar occultations. *Astron. Astrophys.*, **495**, L17–L21, doi:10.1051/0004-6361/200911633, 0901.4882.

Leovy, C. and Y. Mintz, 1969: Numerical simulation of the atmospheric circulation and climate of Mars. *J. Atmos. Sci.*, **26 (6)**, 1167–1189.

Lewis, S. R., P. L. Read, and M. Collins, 1996: Martian atmospheric data assimilation with a simplified general cirulcation model: orbiter and lander networks. *Planet. Space Sci.*, **44 (11)**, 1395–1409.

Lindzen, R. S. and A. Y. Hou, 1988: Hadley circulations for zonally averaged heating centered off the equator. *J. Atmos. Sci.*, **45 (17)**, 2416–2427.

López-Valverde, M. A., D. P. Edwards, M. López-Puertas, and C. Roldán, 1998: Non-local thermodynamic equilbrium in general circulation models of the Martian atmosphere 1. Effects of the local thermodynamic equilibrium approximation on thermal cooling and solar heating. *J. Geophys. Res.*, **103 (E7)**, 16 799–16 811.

Magalhães, J. A., 1987: The Martian Hadley circulation: Comparison of "viscous" model prediction to observations. *Icarus*, **70**, 442–468.

Magalhães, J. A., J. T. Schofiled, and A. Seiff, 1999: Results of the Mars Pathfinder atmospheric structure investigation. *J. Geophys. Res.*, **104**, 8943–8955.

Marshall, J., A. Adcroft, C. Hill, L. Perelman, and C. Heisey, 1997: A finite-volume, incompressible Navier Stokes model for studies of the ocean on parallel computers. *J. Geophys. Res.*, **102**, 5753–5766.

Martin, T. Z. and H. H. Kieffer, 1979: Thermal infrared properties of the Martian atmosphere. ii - the 15-micron band measurements. *J. Geophys. Res.*, **84**, 2843–2852.

Martínez, G., F. Valero, and L. Vázquez, 2009: Characterization of the Martian convective boundary layer. *J. Atmos. Sci.*, **66**, 2044–2058.

Michaux, C. M., 1967: *Handbook of the Physical Properties of the Planet Mars.* NASA, Washington, D. C.

Millis, R. L., et al., 1993: Pluto's radius and atmosphere: results from the entire 9 June 1988 occultation data set. *Icarus*, **105**, 282–297, doi:10.1006/icar.1993.1126.

Molnar, P. and K. A. Emanuel, 1999: Temperature profiles in radiative-convective equilibrium above surfaces at different heights. *J. Geophys. Res.*, **104**, 24 265–24 271.

Mouden, Y. and J. C. McConnell, 2005: A new model for multiscale modeling of the Martian atmosphere, GM3. *J. Geophys. Res.*, **110**, E04 001, doi: 10.1029/2004JE002354.

Nayvelt, L., P. J. Gierash, and K. H. Cook, 1997: Modeling and observations of Martian stationary waves. *J. Atmos. Sci.*, **54**, 986–1013.

Olkin, C. B., L. Young, E. Young, M. Buie, R. French, R. Howell, J. Regester, and C. Ruhland, 2009: Pluto's increasing atmospheric pressure. *Division of Planetary Sciences 41st Meeting Abstracts*, Bulletin of the American Astronomical Society, Vol. 41, #6.07.

Owen, T., 1992: The composition and early history of the atmosphere of Mars. *Mars*, H. H. Kieffer, Ed., University of Arizona Press, Tucson, 818–834.

Owen, T. C., et al., 1993: Surface ices and the atmospheric composition of Pluto. *Science*, **261**, 745–748, doi:10.1126/science.261.5122.745.

Pasachoff, J. M., et al., 2005: The structure of Pluto's atmosphere from the 2002 August 21 stellar occultation. *Astron. J.*, **129**, 1718–1723, doi:10.1086/427963.

Peck, E. R. and B. N. Khanna, 1966: Dispersion of nitrogen. *Journal of the Optical Society of America*, **56**, 1059–1063.

Peixoto, J. P. and A. H. Oort, 1992: *Physics of Climate*. Springer, New York, 99–100 pp.

Person, M. J., et al., 2008: Waves in Pluto's upper atmosphere. *Astron. J.*, **136**, 1510–1518, doi:10.1088/0004-6256/136/4/1510.

Pleskot, L. K. and E. D. Miner, 1981: Time variability of Martian bolometric albedo. *Icarus*, **45**, 179–201.

Pollack, J. B., R. M. Haberle, J. Schaeffer, and H. Lee, 1990: Simulations of the general circulation of the Martian atmosphere 1. Polar processes. *J. Geophys. Res.*, **95 (B2)**, 1447–1473.

Pollack, J. B., C. B. Leovy, P. W. Greiman, and Y. Mintz, 1981: A Martian general circulation experiment with large topography. *J. Atmos. Sci.*, **38 (1)**, 3–29.

Prinn, R. G. and B. Fegley, 1987: The atmospheres of Venus, Earth, and Mars - A critical comparison. *Annu. Rev. of Earth and Planet. Sci.*, **15**, 171–212, doi: 10.1146/annurev.ea.15.050187.001131.

Putzig, N. E., M. T. Mellon, K. A. Kretke, and R. E. Arvidson, 2005: Global thermal inertia and surface properties of Mars from the MGS mapping mission. *Icarus*, **173**, 325–341, doi:10.1016/j.icarus.2004.08.017.

Richardson, M. I. and R. J. Wilson, 2002: A topographically forced asymmetry in the Martian circulation and climate. *Nature*, **416**, 298–301.

Richardson, M. I., R. J. Wilson, and A. V. Rodin, 2002: Water ice clouds in the Martian atmosphere: General circulation model experiments with a simple cloud scheme. *J. Geophys. Res.*, **107**, doi:10.1029/2001JE001804.

Schneider, E. K., 1977: Axially symmetric steady-state models of the basic state for instability and climate studies. Part II. Nonlinear calculations. *Journal of Atmospheric Sciences*, **34**, 280–296.

Schneider, E. K. and R. S. Lindzen, 1977: Axially symmetric steady-state models of the basic state for instability and climate studies. Part I. Linearized calculations. *Journal of Atmospheric Sciences*, **34**, 263–279.

Seiff, A. and D. B. Kirk, 1977: Structure of the atmosphere of Mars in summer at mid-latitudes. *J. Geophys. Res.*, **82**, 4364–4378.

Showman, A., C. S. Cooper, J. J. Fortney, and M. S. Marley, 2008: Atmospheric circulation of hot Jupiters: Three-dimensional circulation models of HD 209458b and HD 189733b with simplified forcing. *ApJ*, **682**, 559–576, doi:10.1086/58932.

Sicardy, B., et al., 2003: Large changes in Pluto's atmosphere as revealed by recent stellar occultations. *Nature*, **424**, 168–170.

Smith, D. E., et al., 1999: The global topography of Mars and implications for surface evolution. *Science*, **284 (5419)**, 1495–1503.

Smith, D. E., et al., 2001: Mars Orbiter Laser Altimeter: Experiment summary after the first year of global mapping of Mars. *J. Geophys. Res.*, **106**, 23 689–23 722, doi:10.1029/2000JE001364.

Smith, M. D., 2004: Interannual variability in TES atmospheric observations of mars during 1999-2003. *Icarus*, **167**, 148–165.

Stansberry, J. A., J. I. Lunine, W. B. Hubbard, R. V. Yelle, and D. M. Hunten, 1994: Mirages and the nature of Pluto's atmosphere. *Icarus*, **111**, 503–513, doi: 10.1006/icar.1994.1160.

Stansberry, J. A., J. I. Lunine, and M. G. Tomasko, 1989: Upper limits on possible photochemical hazes on Pluto. *Geophys. Res. Lett.*, **16**, 1221–1224, doi: 10.1029/GL016i011p01221.

Strobel, D. F., X. Zhu, M. E. Summers, and M. H. Stevens, 1996: On the vertical thermal structure of Pluto's atmosphere. *Icarus*, **120**, 266–289, doi: 10.1006/icar.1996.0050.

Stull, R. B., 1988: *An introduction to boundary layer meteorology.* Atmospheric Sciences Library, Kluwer Academic Publishers, Dordrecht, The Netherlands.

Summers, M. E., D. F. Strobel, and G. R. Gladstone, 1997: Chemical models of Pluto's atmosphere. *Pluto and Charon*, S. A. Stern and D. J. Tholen, Eds., University of Arizona Press, Tucson, 391.

Sutton, J. L., C. B. Levoy, and J. E. Tillman, 1978: Diurnal variations of the Martian surface layer meteorological parameters during the first 45 sols at two Viking Lander sites. *J. Atmos. Sci.*, **35**, 2346–2355, doi:10.1175/1520-0469(1978)035.

Takahashi, Y. O., H. Fujiwara, H. Fukunishi, M. Odaka, Y.-Y. Hayashi, and S. Watanabe, 2003: Topographically induced north-south asymmetry of the meridional circulation in the Martian atmosphere. *J. Geophys. Res.*, **108 (E3)**, doi: 10.1029/2001JE001638.

Tillman, J. E., 1989: VL1/VL2 Mars meteorology resampled daily avg. pressure v1.0. Dataset name: VL1/VL2-M-MET-4-DAILY-AVG-PRESSURE-V1.0. NASA Planetary Data System.

Tillman, J. E., L. Landberg, and S. E. Larsen, 1994: The boundary layer of Mars: Fluxes, stability, turbulent spectra, and growth of the mixed layer. *J. Atmos. Sci.*, **51**, 1709–1727.

Toon, O. B., C. P. McKay, T. P. Ackerman, and K. Santhanam, 1989: Rapid calculation of radiative heating rates and photodissociation rates in inhomogeneous multiple scattering atmospheres. *J. Geophys. Res.*, **94**, 16 287–16 301, doi: 10.1029/JD094iD13p16287.

Tryka, K. A., R. H. Brown, D. P. Chruikshank, T. C. Owen, T. R. Geballe, and C. Debergh, 1994: Temperature of nitrogen ice on Pluto and its implications for flux measurements. *Icarus*, **112**, 513–527, doi:10.1006/icar.1994.1202.

Walker, C. C. and T. Schneider, 2006: Eddy influences on Hadley circulations: Simulations with an idealized GCM. *J. Atmos. Sci.*, **63**, 3333–3350.

Webster, P. J., 1977: The low-latitude circulation of Mars. *Icarus*, **30**, 626–649.

Wilson, R. J., 1997: A general circulation model simulation of the Martian polar warming. *Geophys. Res. Lett.*, **24 (2)**, 123–126.

Wilson, R. J., D. Banfield, B. J. Conrath, and M. D. Smith, 2002: Traveling waves in the northern hemisphere of Mars. *Geophys. Res. Lett.*, **29 (14)**, doi: 10.1029/2002GL014866.

Wilson, R. J. and K. Hamilton, 1996: Comprehensive model simulations of thermal tides in the Martian atmosphere. *J. Atmos. Sci.*, **53 (9)**, 1290–1326.

Wilson, R. J., S. R. Lewis, L. Montabone, and M. D. Smith, 2008: Influence of water ice clouds on Martian tropical atmospheric temperatures. *Geophys. Res. Lett.*, **35**, doi:10.1029/2007GL032405.

Wilson, R. J., G. A. Neumann, and M. D. Smith, 2007: Diurnal variation and radiative influence of Martian water ice clouds. *Geophys. Res. Lett.*, **34**, doi: 10.1029/2006GL027976.

Withers, P. and M. D. Smith, 2006: Atmospheric entry profiles from the Mars Exploration Rovers Spirit and Opportunity. *Icarus*, **185**, 133–142.

Yelle, R. V. and J. I. Lunine, 1989: Evidence for a molecule heavier than methane in the atmosphere of Pluto. *Nature*, **339**, 288–290, doi:10.1038/339288a0.

Young, E. F. and R. P. Binzel, 1994: A new determination of radii and limb parameters for Pluto and Charon from mutual event lightcurves. *Icarus*, **108**, 219–224, doi:10.1006/icar.1994.1056.

Young, E. F., et al., 2008a: Vertical structure in Pluto's atmosphere from the 2006 June 12 stellar occultation. *Astron. J.*, **136**, 1757–1769, doi:10.1088/0004-6256/136/5/1757.

Young, L., M. W. Buie, C. B. Olkin, E. F. Young, R. G. French, and R. R. Howell, 2008b: Pluto's lower atmosphere from stellar occultations. *Division of Planetary Sciences 40th Meeting Abstracts*, Bulletin of the American Astronomical Society, Vol. 40, #36.03.

Young, L. A., J. L. Elliot, A. Tokunaga, C. de Bergh, and T. Owen, 1997: Detection of gaseous methane on Pluto. *Icarus*, **127**, 258–262, doi:10.1006/icar.1997.5709.

Zalucha, A., et al., 2007: The 2003 November 14 occultation by Titan of TYC 1343-1865-1. II. Analysis of light curves. *Icarus*, **192**, 503–518, doi: 10.1016/j.icarus.2007.08.008.

Zhong, S. and M. T. Zuber, 2001: Degree-1 mantle convection and the crustal dichotomy on Mars. *Earth and Planetary Science Letters*, **189**, 75–84, doi: 10.1016/S0012-821X(01)00345-4.

Zurek, R. W., J. R. Barnes, R. M. Haberle, J. B. Pollack, J. E. Tillman, and C. B. Leovy, 1992: Dynamics of the atmosphere of Mars. *Mars*, H. H. Kieffer, Ed., University of Arizona Press, Tucson, 835–933.